RCA REVIEW

a technical journal

Published quarterly by

RCA LABORATORIES

in cooperation with all subsidiaries and divisions of

RADIO CORPORATION OF AMERICA

VOLUME XXVIII SEPTEMBER 1967 NUMBER 3

CONTENTS

RCA REVIEW is regularly abstracted and indexed by *Abstracts of Photographic Science and Engineering Literature, Applied Science and Technology Index, Bulletin Signalétique des Télecommunications, Chemical Abstracts, Electronic and Radio Engineer, Mathematical Reviews, and Science Abstracts* (I.E.E.-Brit.).

RCA REVIEW

BOARD OF EDITORS

HIGH-FREQUENCY CHARACTERISTICS OF THE INSULATED-GATE FIELD-EFFECT TRANSISTOR

By

Joseph R. Burns

RCA Laboratories
Princeton, N. J.

Summary—A detailed analysis of the active channel of an insulated-gate field-effect transistor is used to characterize the performance of the device as a high-frequency amplifier. Closed-form expressions are obtained that determine the input admittance and transconductance as functions of frequency and the d-c operating point of the transistor. An approximate equivalent circuit is obtained that predicts the unilateral power gain to within 1 db over the useful frequency range. A comparison between the tetrode (double-gate transistor) and triode (single-gate transistor) shows that, while the tetrode is capable of higher power gain, the triode has a flatter frequency response. The results are summarized by a relative comparison of the gain–bandwidth products of the silicon insulated-gate (MOS) transistor and the bipolar transistor.

Introduction

THE INSULATED-gate field-effect transistor (IGFET), developed in 1962, has exhibited many desirable features as an r-f amplifier. Among these are the excellent cross-modulation-distortion characteristics derived from its square-law behavior and the simplicity of biasing circuitry that is a result of the insulated input terminal. An early disadvantage was the instability of the d-c operating point under stress (high gate fields and/or high ambient temperatures), but this has been largely eliminated by "clean" oxide processing techniques. Despite this, acceptance of the device in r-f amplifier applications has been minimal, particularly in the UHF range where use of the bipolar transistor has provided higher power gain. Evaluation of the high-frequency power gain of the IGFET has been mostly qualitative (or experimental), due mainly to the lack of an accurate equivalent circuit model. The main object of this paper is, therefore, to quantitatively determine the high-frequency limits of this device and to develop an equivalent circuit to simplify analysis and design of high-frequency IGFET amplifiers.

STATIC CHARACTERISTICS

The insulated-gate field-effect transistor has a number of physical forms, all of which have been extensively described in the literature[1,2] and all of which have essentially the same physical behavior. For purposes of discussion, the properties of the device will be illustrated using the bulk-silicon version commonly called the MOS transistor (Metal-

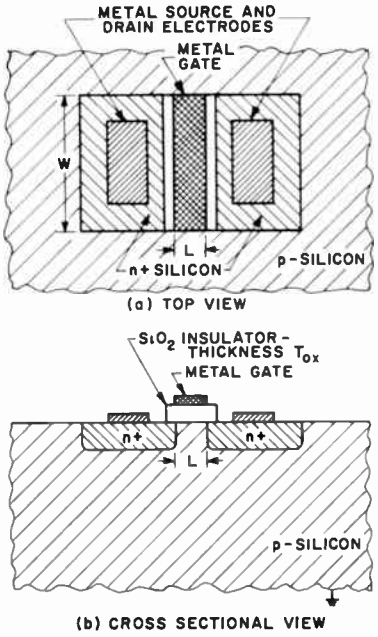

Fig. 1—Physical construction of MOS transistor.

Oxide-Semiconductor). The top and cross-sectional views shown in Figure 1 illustrate the typical construction of the device. It consists of two heavily doped silicon regions (called the source and drain) separated by a distance L. The region between the source and drain is commonly called the *channel* and is composed of silicon whose conductivity is controlled by the *gate* terminal, which is a metal electrode electrically insulated from the channel (as well as the source and drain) by a thermally grown oxide layer of thickness T_{ox} and dielectric per-

[1] S. R. Hofstein and F. P. Heiman, "The Silicon Insulated-Gate Field-Effect Transistor," *Proc. IEEE*, Vol. 51, p. 1190, Sept. 1963.
[2] P. K. Weimer, "The TFT—A new Thin-Film Transistor," *Proc. IRE*, Vol. 50, p. 1462, June 1962.

mittivity ϵ_{ox}. The width of the channel is denoted by W. Physically, the device is a parallel-plate capacitor with the metal gate electrode as one plate and the silicon channel as the other. The induced charge on the bottom plate is mobile in that it is free to move between the source and drain electrodes and thereby conducts a current when an electric field is applied between source and drain. In the case of the device shown in Figure 1, the electrodes are heavily doped n-type silicon and, therefore, good suppliers of electrons. Application of a positive voltage on the gate will tend to induce negative charge in the channel and enable electron current to flow from source to drain when a positive voltage is applied to the drain electrode and the source is at ground potential. Such a device is called an n-channel transistor. Below a certain value of gate-to-source voltage, no current flows in the drain circuit for any value of drain voltage V_D. This is because of the finite resistivity of the p-type substrate and residual charge in both the oxide layer and at the semiconductor–insulator interface (surface states). These residual charges cause a residual (positive or negative) charge in the surface layer of the silicon when the voltage on the gate electrode is zero. Assuming this charge is σ_0 coulombs per square meter, the total charge per square meter near the source electrode is

$$\sigma_T = -C_m V_{gs} + \sigma_0 \qquad \text{coulombs/meters}^2, \qquad (1)$$

where $C_m = \epsilon_{ox}/T_{ox}$ is the capacitance/m^2 of the gate insulator. The threshold voltage is then given by the gate voltage where σ_T goes to zero, or

$$V_T = \frac{\sigma_0}{C_m} = \frac{\sigma_0 T_{ox}}{\epsilon_{ox}}. \qquad (2)$$

Note that if $\sigma_0 > 0$, $V_T > 0$, so that a finite positive voltage must be applied to the gate electrode before drain current flows. A positive V_T for an n-channel device typifies an enhancement-type transistor. Similarly, if $\sigma_0 < 0$, a negative voltage is required to stop drain-current flow; in other words, a finite drain current flows when the gate-to-source voltage $V_{gs} = 0$. A negative V_T characterizes a depletion-type transistor for an n-channel device. Analogous arguments hold for a p-channel device with appropriate changes in sign.

Assuming an n-channel transistor with the source grounded and voltages V_G and V_D (with respect to ground) applied to the gate and drain electrodes, respectively, the low-frequency drain-current characteristics may be derived as follows.

Defining $X = 0$ as the source and $X = L$ as the drain and assuming

a channel potential $V(X)$, the charge per unit area in the channel at any point X is given by

$$\sigma(X) = -C_m\,(V_G - V(X)) + \sigma_o = -C_m\,(V_G - V_T - V(X)), \quad (3)$$

where $(V_G - V_T)$ is assumed greater than $V(X)$ for all X (i.e., $V_D < V_G - V_T$). Since the device is symmetrical in the Z direction, this distribution may be immediately integrated over this dimension to give a charge per unit length in the X direction as

$$\begin{aligned} Q(X) &= -C_m W\,(V_G - V_T - V(X)) \\ &= -\overline{C}\,(V_G - V_T - V(X)) \text{ coulomb/meter} \end{aligned} \quad (4)$$

where $\overline{C} = \epsilon_{ox} W/T_{ox}$ is the capacitance per unit length in the X direction. The current flowing in the channel can now be obtained by Ohm's law, i.e.,

$$I(X) = Q(X)\,v\,(X) = \bar{\mu}_n \overline{C}\,(V_G - V_T - V(X))\,\frac{dV(X)}{dX} \quad (5)$$

where $v\,(X)$ is the velocity of the electron, $\bar{\mu}_n$ is the effective mobility of the electrons in the channel and is constant, $dV(X)/dX$ is the electric field in the channel, and $I(X) = I_D$ is independent of X for low frequencies.

Integrating both sides with respect to X from 0 to L, we obtain

$$I_D L = \bar{\mu}_n \overline{C} \int_{V_G - V_T}^{V_G - V_T - V_D} (V_G - V_T - V(X))\,d(V_G - V_T - V(X)) \,. \quad (6)$$

Integrating and substituting $\overline{C} = \epsilon_{ox} W/T_{ox}$

$$I_{DS} = \frac{\bar{\mu}_n\,\epsilon_{ox}\,W}{2\,L\,T_{ox}}\,[2\,V_D\,(V_G - V_T) - V_D{}^2] \,. \quad (7)$$

The preceding analysis assumed that the channel was not pinched off at any point, i.e., that $V_G - V_T > V_D$. As V_D approaches a value $V_G - V_T$, the drain region approaches cutoff (i.e., no charge is induced in this region) and the current approaches

$$I_{DS} = \frac{\bar{\mu}_n \epsilon_{ox} W}{2 L T_{ox}} (V_G - V_T)^2 \; ; \; V_D = V_G - V_T \, . \tag{8}$$

For further increases in V_D above $(V_G - V_T)$, the current remains constant at the above value. This is not immediately obvious, but can be made plausible by the following physical argument. At some point in the channel, say $X = L'$, the potential must have a value $V(L') = V_G - V_T$, as $V(0) = 0$ and $V(L) = V_D > (V_G - V_T)$. The behavior of the device may then be analyzed, as was done previously, from $X = 0$ to $X = L'$ giving the same current as in Equation (8), except that L must be replaced by L'. Because of continuity of current, this must be the same current that flows in the drain circuit regardless of V_D. In most devices of interest, it happens that $L' \approx L$, so that in the so-called current-saturation region Equation (8) holds for $V_D \geq V_G - V_T$.

In practice, although the drain current remains approximately constant above $V_D = V_G - V_T$, a finite slope of the I_D versus V_D characteristic appears (in some cases this slope is even caused by a reduction in L) giving rise to a finite amplification factor.*

Above $V_D = V_G - V_T$, the current increases as the square of the gate-to-source voltage, so that the small-signal transconductance can be defined as:

$$g_{m_0} = \left. \frac{\partial I_D}{\partial V_G} \right|_{V_D} = \frac{\bar{\mu}_n \epsilon_{ox} W}{L T_{ox}} (V_G - V_T) \quad \text{amperes/volt.} \tag{9}$$

If we define $C_{ox} = \epsilon_{ox} W L / T_{ox}$ as the total parallel-plate capacitance appearing in the gate circuit, the classical figure of merit (or gain–bandwidth product) of such a device is

$$\omega_0 = \frac{g_{m_0}}{C_{ox}} = \frac{\bar{\mu}_n (V_G - V_T)}{L^2} \quad \text{radians/seconds.} \tag{10}$$

This quantity will be discussed in much more detail in connection with the high-frequency properties of the device.

Before proceeding, it will be instructive at this point to derive the voltage distribution $V(X)$, as this is essential to the solution of the partial differential equations that arise at high frequencies. Referring

* For a complete treatment, see Reference (11).

to Equation (5) again and noting that I is independent of X, it is evident that

$$(V_G - V_T - V(X))\frac{dV}{dX} = \text{constant}. \qquad (11(a))$$

Integrating both sides from 0 to X gives

$$(V_G - V_T - V(X))^2 = C_1 X + C_2, \qquad (11(b))$$

which, coupled with the boundary conditions $V(0) = 0$ and $V(L) = V_D$, yields

$$V(X) = (V_G - V_T)\left[1 - \sqrt{1 - \frac{X}{L} + \left(1 - \frac{V_D}{V_G - V_T}\right)^2 \frac{X}{L}}\right] \qquad (12(a))$$

for $V_D < V_G - V_T$,

$$V(X) = (V_G - V_T)\left[1 - \sqrt{1 - \frac{X}{L}}\right] \qquad (12(b))$$

for $V_D \geq V_G - V_T$.

Having obtained these distributions, particularly (12(b)), which is most important for small-signal-amplifier applications, it is now possible to derive another important relationship for high frequencies, namely the transit time of electrons from source to drain. This characteristic time is given by

$$\tau_0 = \int_0^L \frac{dX}{v(X)} = \int_0^L \frac{dX}{\bar{\mu}_n \dfrac{dV}{dX}}. \qquad (13)$$

After differentiating (12(b))

$$\tau_0 = \frac{2L}{\bar{\mu}_n(V_G - V_T)} \int_0^L \sqrt{1 - \frac{X}{L}}\, dx = \frac{4}{3} \frac{L^2}{\bar{\mu}_n(V_G - V_T)}. \qquad (14(a))$$

Using Equation (10), the above becomes

$$\tau_o = \frac{4}{3}\frac{C_{ox}}{g_{m_o}} = \frac{4}{3}\frac{1}{\omega_o}. \qquad (14(b))$$

High-Frequency Model for the MOS Transistor

The high-frequency performance of the MOS transistor is best analyzed, for both small- and large-signal applications, as a nonlinear *RC* transmission line. This is shown schematically in Figure 2, where the capacitance per unit length is constant and the resistance per unit

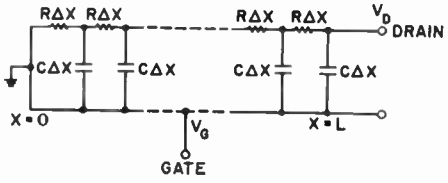

Fig. 2—Transmission-line model of MOS channel.

length is a function of the voltage at a particular point. The voltage, in turn, is a function of both distance and time. This model is similar to that used previously for the junction-gate field-effect transistor[3] and for the MOS transistor.[4-6] The analysis here differs from all of the above in that the solution obtained is an exact analytic expression in terms of the Laplace transform variable. This greatly simplifies characterization of the device in terms of a high-frequency equivalent circuit.

We set down the well-known transmission line equations,

$$\frac{\partial I(X,t)}{\partial X} = -\overline{C}\frac{\partial}{\partial t}(V(X,t) - V_G(t)) \qquad (15(a))$$

---

[3] A. van der Ziel and J. W. Ero, "Small-Signal High-Frequency Theory of Field-Effect Transistors," *Trans. IEEE PTGED*, Vol. ED-11, p. 128, April 1964.

[4] J. R. Hauser, "Small-Signal Properties of Field-Effects Devices," *Trans. IEEE PTGED*, Vol. ED-12, p. 605, Dec. 1965.

[5] D. Candler and A. Jordan, "A Small-Signal High-Frequency Analysis of the Insulated-Gate Field-Effect Transistor," *Int. Jour. Electronics*, Vol. IX, p. 181, Aug. 1965.

[6] J. A. Guerst, "Calculation of High-Frequency Characteristics of Thin-Film Transistors," *Solid State Electronics*, Vol. 8, p. 88, Jan. 1965.

$$\frac{\partial V\,(X,t)}{\partial X} = -\,I\,(X,t)\,\bar{R}\,, \qquad (15(b))$$

where $\bar{R}$ and $\overline{C}$ are the resistance and capacitance per unit length. From Equation (4)

$$\overline{C} = \frac{\epsilon_{ox}\,W}{T_{ox}} = \text{constant}\,,$$

while Equation (5) gives for $\overline{G} = R^{-1}$

$$\overline{G} = \bar{\mu}_n\,\overline{C}\,(V_G - V_T - V(X,t))\,.$$

Substitution of these relations in Equations (15) gives

$$\frac{\partial I(X,t)}{\partial X} = -\,\overline{C}\,\frac{\partial}{\partial t}\,(V(X,t) - V_G(t)) \qquad (16(a))$$

$$I(X,t) = -\,\bar{\mu}_n\,\overline{C}\,(V_G - V_T - V(X,t))\,\frac{\partial\,X(X,t)}{\partial X}\,. \qquad (16(b))$$

This set of equations can be simplified by a change in variable given by

$$\overline{V}\,(X,t) = V_G(t) - V_T - V(X,t)\,. \qquad (17)$$

On substitution, Equations (16) become

$$\frac{\partial I(X,t)}{\partial X} = \overline{C}\,\frac{\partial\,\overline{V}\,(X,t)}{\partial\,t} \qquad (18(a))$$

$$I(X,t) = \bar{\mu}_n\,\overline{C}\,\overline{V}\,(X,t)\,\frac{\partial\,\overline{V}\,(X,t)}{\partial X}\,, \qquad (18(b))$$

which represents a pair of nonlinear partial differential equations in the dependent variables $I\,(X,t)$ and $\overline{V}\,AX,t)$. The equations cannot be solved explicitly for I because of this nonlinearity in $\overline{V}(X,t)$, but an

equation for $\overline{V}$ can be readily obtained by differentiation of Equation (18(b)) with respect to X and substitution in Equation (18(a)):

$$\overline{V}\frac{\partial^2\overline{V}}{\partial X^2}+\left(\frac{\partial\overline{V}}{\partial X}\right)^2=\frac{1}{\bar{\mu}_n}\frac{\partial\overline{V}}{\partial t},$$

or

$$\frac{\partial^2}{\partial X^2}(\overline{V}^2(X,t))=\frac{2}{\bar{\mu}_n}\frac{\partial\overline{V}(X,t)}{\partial t}.$$

These equations must be solved for $\overline{V}$ subject to various boundary conditions, and the current (which is usually the variable of interest) is then derived from the defining relationship Equation (18(b)).

The object of this paper, then, is the solution of Equation (17) subject to appropriate boundary conditions and the high-frequency limits of the device obtained for small-signal-amplifier applications. Suitable approximations can be made under the assumption of small signals that give the high-frequency behavior in closed form. These are discussed in the next section.

III. The MOS Transistor as a Small-Signal, High-Frequency Amplifier

A. Analytical Solution of High-Frequency Behavior

The object here is to ascertain the high-frequency behavior of the MOS device, in particular the behavior of the small-signal transconductance and the input admittance, which is capacitive at low frequencies. This analysis does not include second-order effects such as the output admittance of the drain and stray capacitance due to overlap of the gate electrode over the source and drain electrodes. In regard to these effects, then, the device is assumed to be "ideal". The circuit diagram used to analyze the transistor is shown in Figure 3.

When used as an amplifier, the transistor is biased with a gate voltage V_G and a drain voltage $V_D > V_G - V_T$. The d-c drain (and source) current is then, from Equation (8),

$$I_o=\frac{\bar{\mu}_n\epsilon_{ox}W}{2LT_{ox}}(V_G-V_T)^2=K_n(V_G-V_T)^2 \text{ amperes.}$$

The low-frequency transconductance, by Equation (9), is

$$g_{m_0} = \frac{\bar{\mu}_n \epsilon_{ox} W}{L T_{ox}} (V_G - V_T) = 2 K_n (V_G - V_T) \text{ amperes per volt.}$$

Also shown in the figure is a small-signal generator, $\delta \sin \omega t$, which is superimposed on the bias voltage V_G. The small-signal responses to this generator, i.e., i_{in}, i_s, and i_d, will determine the input admittance

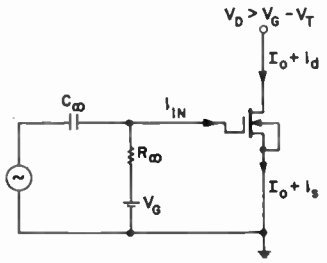

Fig. 3—Schematic of MOS amplifier.

and transconductance as functions of frequency. For purposes of analysis, however, this generator will be replaced by a generator of complex frequencies S, where $S = \sigma + j\omega$ is the complex angular frequency. This will greatly simplify subsequent manipulation of the input admittance expression, particularly in the synthesis of an equivalent input network. Furthermore, the Laplace transform will enable the transient response to a small step voltage on the gate to be readily determined and related to the sinusoidal response. The steady-state sinusoidal solution is easily obtained by setting $S = j\omega$.

For small-signal inputs, the variable $\overline{V}(X,t)$ can be represented by

$$\overline{V}(X,t) = \overline{V}_0(X) + \frac{\epsilon(X,t)}{2} = (V_G - V_T)\sqrt{1 - \frac{X}{L} + \frac{1}{2}\epsilon(X,t)}\,,$$

and (19)

$$\overline{V^2}(X,t) \approx (V_G - V_T)^2 \left(1 - \frac{X}{L}\right) + (V_G - V_T)\sqrt{1 - \frac{X}{L}}\,\epsilon(X,t)\,.$$

Here, $\frac{1}{2}\epsilon(X,t)$ represents the deviation of the voltage distribution from $\overline{V}_0(X)$, the d-c distribution, under an applied input signal of magnitude much less than $\overline{V}_0(X)$. Substituting this into Equation

(18(b)) and carrying out the indicated differentiation gives

$$\frac{\partial \epsilon}{\partial t} = \omega_o \left[\sqrt{Z} \frac{\partial^2 \epsilon}{\partial Z^2} + \frac{1}{\sqrt{Z}} \frac{\partial \epsilon}{\partial Z} - \frac{\epsilon}{4(Z)^{3/2}} \right], \tag{20}$$

where $Z \equiv 1 - (X/L)$ is the new independent position variable and $\omega_o = \tilde{\mu}_n (V_G - V_T)/L^2 = g_{m_o}/C_{ox}$.

The solution of the above equation is given in terms of the modified Bessel function of order $\frac{2}{3}$ (see Appendix I). From this solution, the variables of most interest can be obtained, namely, the drain, source, and input currents, as functions of frequency and the device parameters. These are, from Equations (51) and (52) in Appendix I given in series expansion form by

$$i_d(S') = \frac{g_{m_o}\, \delta(S')}{1 + \frac{4}{15} S' + \frac{1}{45} S'^2 + \frac{8}{8910} S'^3 + \ldots} = g_m(S')\, \delta(S') \tag{21}$$

and

$$i_{in}(S') = i_s(S') - i_d(S') = g_{m_o}\, \delta(S') \left[\frac{\frac{2}{3} S' + \frac{4}{45} S'^2 + \frac{2}{405} S'^3 + \ldots}{1 + \frac{4}{15} S' + \frac{1}{45} S'^2 + \ldots} \right]$$

$$= Y_{in}(S')\, \delta(S') \tag{22}$$

where $S' = S/\omega_o$ represents a normalized Laplace transform variable.

The variations of $g_m(\omega)$ and $Y_{in}(\omega)$ are shown plotted in Figures 4 and 5 for steady state where $S' = j\omega/\omega_o$. Significant features to note are that the magnitude of g_m is down 3 db at a frequency $\omega = 6\omega_o$ and that the real and imaginary parts of the input admittance are both monotonically increasing functions of frequency. Good agreement between these results and previously published experimental results is obtained.[7, 8, 9]

[7] P. Kolk and H. Johnson, *Field-Effect Transistors—Physics, Technology, and Applications*, Chap. 11, Prentice Hall. 1966.

[8] M. Mitchell, "The N-Channel MOS as an RF Amplifier," *Digest of Technical Papers, Int. Solid State Circuits Conf.*, 1966.

[9] Data Sheet for the RCA 3N128 Silicon MOS transistor.

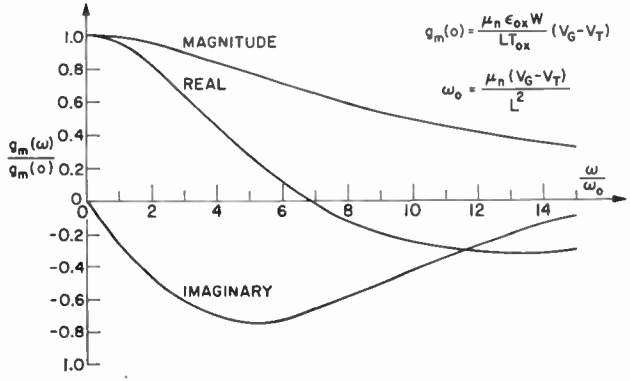

Fig. 4—Transconductance versus frequency.

B. Frequency Response of the MOS Tetrode

A circuit that has been used extensively for high-frequency amplification is the MOS tetrode shown in Figure 6. The tetrode connection is seen to consist of two MOS transistors serially connected from the upper terminal to ground in a cascode or driven grounded-gate arrangement. The gate or control terminals are independent and isolated from one another with gate No. 1 acting as the input terminal and gate No. 2 as the a-g-c terminal, which is normally at a-c ground potential. As is well known, in vacuum-tube circuits such an arrangement yields extremely high output resistance and almost completely eliminates the increase in feed-back capacitance due to the Miller effect, since the input and output are effectively isolated by the second transistor. The low-frequency equivalent circuit of the tetrode under these con-

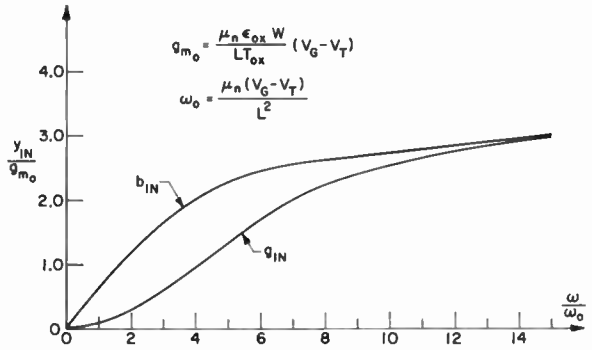

Fig. 5—Input admittance versus frequency.

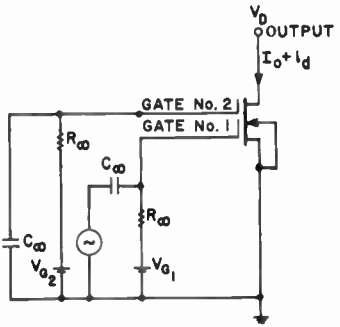

Fig. 6—Schematic of MOS tetrode.

ditions is shown in Figure 7, where it is assumed that both transistors are in the high-gain or current-saturation regions and have identical transconductances and drain resistances.

Note that the circuit is identical to that of the equivalent vacuum-tube circuit in that the output resistance is effectively multiplied by a factor of $A_{Vo} + 2$ where $A_{Vo} = g_{m_o} r_d$, which is the low-frequency amplification factor.*

Before proceeding to a high-frequency analysis of the tetrode, it will first be necessary to derive the d-c operating conditions when both transistors are in their active regions. This implies the two conditions;

$$V_D \geqq V_{G_2} - V_T \qquad (23(a))$$

$$V_1 \geqq V_{G_1} - V_T \,. \qquad (23(b))$$

where V_1 is the voltage at the common terminal of the two devices.

A further condition is that the current in the two transistors must be the same. This, in turn, implies

$$K_{n_2} (V_{G_2} - V_1 - V_T)^2 = K_{n_1} (V_{G_1} - V_T)^2 \,, \qquad (24)$$

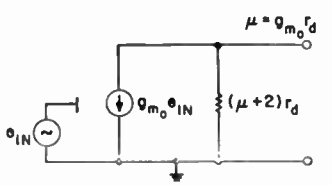

Fig. 7—Low-frequency equivalent circuit of MOS tetrode.

* This somewhat unconventional notation for the amplification factor is used to avoid confusion with the symbol adopted for the carrier mobility.

since both devices are assumed in current saturation. Solving for V_1,

$$V_1 = V_{G_2} - V_{G_1} - V_T (1 - \gamma). \tag{25}$$

Here

$$\gamma = \sqrt{\frac{K_{n_1}}{K_{n_2}}} = \sqrt{\frac{W_2 L_1}{W_1 L_2}}$$

is a dimensionless factor depending only on the relative dimensions of the two devices.† For identical devices, i.e., $\gamma = 1$, Equation (25) becomes, simply,

$$V_1 = V_{G_2} - V_{G_1},$$

For a given V_{G_1}, the inequalities (23) become

$$V_D > V_{G_2} - V_T \tag{26(a)}$$

$$V_{G_2} > 2\, V_{G_1} - V_T. \tag{26(b)}$$

Assuming that these conditions are satisfied for a given set of V_{G_1}, V_{G_2}, and V_D (which implies fixed values of the transistor low-frequency transconductances g_{m_1} and g_{m_2} and characteristic frequencies ω_1 and ω_2), the output drain current can be calculated as follows. An input signal $\delta(s)$ produces a drain current in the first transistor given by

$$i_{d_1} = g_{m_1} \left(\frac{S}{\omega_1} \right) \delta(S). \tag{27}$$

This in turn creates a voltage $v_1(S)$ at the source of the second transistor,

$$v_1(S) = \frac{i_{d_1}(S)}{Y_s\left(\frac{S}{\omega_2}\right)} = \frac{g_{m_1}\left(\frac{S}{\omega_1}\right)\delta(S)}{Y_s\left(\frac{S}{\omega_2}\right)}, \tag{28}$$

where Y_s is the input admittance looking in at the source of transistor

† This, of course, assumes equal mobilities and identical oxide structures for the two devises.

No. 2. The output current is then, simply,

$$i_{d_2}(S) = g_{m_2}\left(\frac{S}{\omega_2}\right) v_1(S) = \frac{g_{m_1}\left(\frac{S}{\omega_1}\right) g_{m_2}\left(\frac{S}{\omega_2}\right)}{Y_s\left(\frac{S}{\omega_2}\right)} \delta(S) . \qquad (29)$$

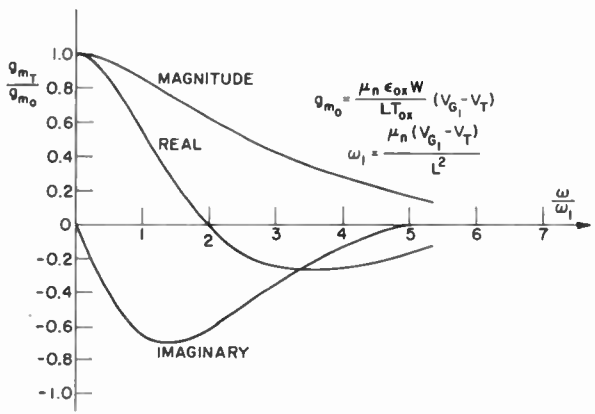

Fig. 8—Transconductance of MOS tetrode versus frequency.

Combining Equations (51) and (54) in Appendix I, the total transconductance of the MOS tetrode is

$$g_{m_T} = \frac{(g_{m_1})_o}{\left(1 + \frac{2}{3}\frac{S}{\omega_2} + \frac{4}{45}\frac{S^2}{\omega_2^2} + \ldots\right)\left(1 + \frac{4}{15}\frac{S}{\omega_1} + \frac{S^2}{45\,\omega_1^2} + \ldots\right)} \qquad (30)$$

which is obviously poorer in frequency response than an individual device. Assuming, again, identical devices and the same d-c gate-to-source voltages,

$$g_{m_T}(S) = \frac{(g_{m_1})_o}{\left(1 + \frac{14}{15}\frac{S}{\omega_1} + \frac{13}{45}\frac{S^2}{\omega_1^2} + \frac{1}{34}\frac{S^3}{\omega_1^3} + \ldots\right)} . \qquad (31)$$

Equation (31) is plotted in Figure 8 for the steady state where $S = j\omega$.

A comparison of Figures 8 and 4 shows that the transconductance of the tetrode is degraded in frequency response by a factor of 3.5 to 4.0 for the same transistor parameters. The input admittance, of course, remains the same, but the output admittance is lowered by the amplification factor of the upper transistor. Physically, the degradation in g_m results from an effective increase in transit time of the electrons, which now, rather than traveling a distance L, must travel a total distance of $2L$.* According to Equation (14), this increases the transit time by a factor of 4, which is approximately the factor of degradation of the tetrode obtained from the exact expression Equation (31). The tetrode is analyzed further in Section D, where power gain is considered.

C. Small-Signal Equivalent Circuits

On the basis of the results derived previously (input admittance and transconductance as functions of S), it is possible to determine an equivalent electrical network that characterizes the MOS transistor. There are, of course, many ways of arranging such a network and, for a given configuration, just as many ways of realizing the configuration. Two of the most straightforward are shown in Figure 9.

In Figure 9(a), the input and output circuits are effectively separated. The input is represented as a two-terminal driving-point impedance that realizes Z_{in} from Equation (22); the output is represented by a frequency-dependent current generator with $g_m(\omega)$ given by Equation (21). In Figure 9(b), the input and output circuit frequency dependence is combined into a single four-terminal network N_2 realized in such a manner that its driving-point impedance is the appropriate Z_{in} and also yields an output voltage which, when multiplied by g_{m_o}, the low-frequency transconductance, gives the proper frequency response of the drain current. The latter approach is more satisfying, as it is closely related to the actual operation of the device (i.e., a strong coupling between the input and output through the active channel). In addition, it is conceptually simpler and easier to use. Synthesis of 4-terminal networks is generally a more difficult problem than that of driving-point-impedance synthesis, but when a given network is only partially specified (only 1 or 2 of the three z or y parameters are given) as is the case here, the overall complexity is reduced considerably.† It can be shown that if such is the case, the input impedance can always

* From a circuit point of view, this is equivalent to saying that the current is decreased because of the additional current lost in the distributed capacitance of the upper transistor.

† See, for example, E. Guillemin, Chapter 7 in *Synthesis of Passive Networks*, Wiley, 1957.

be developed so as to simultaneously realize the desired transfer function to within a constant multiplier. More precisely, the properties of the 4-terminal network are

$$Z_{in}(S) = \frac{1}{g_{m_o}} \frac{1 + \frac{4}{15}\frac{S}{\omega_o} + \frac{1}{45}\frac{S^2}{\omega_o^2} + \ldots}{\frac{2}{3}\frac{S}{\omega_o} + \frac{4}{45}\frac{S^2}{\omega_o^2} + \ldots}, \qquad (32(a))$$

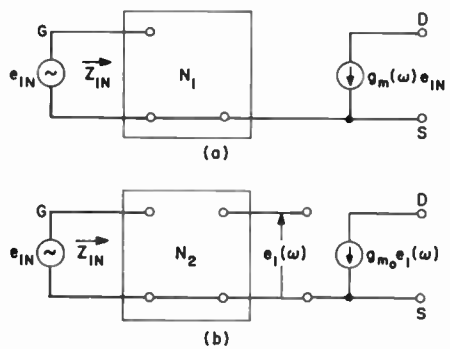

Fig. 9—Equivalent circuit configurations.

$$\frac{e_1(S)}{e_{in}(S)} = \frac{1}{1 + \frac{4}{15}\frac{S}{\omega_o} + \frac{1}{45}\frac{S^2}{\omega_o^2} + \ldots}. \qquad (32(b))$$

Clearly, a circuit of any desired complexity can be obtained depending on the number of terms taken in the series expansions (needless to say, this is not the object). If, as a first approximation, terms up to S^2 are retained in Equation (32(b)) and also in the numerator of Equation (32(a)) and up to S in the denominator of Equation (32(a)), i.e.,

$$Z_{in} \approx \frac{1}{g_{m_o}} \frac{1 + \frac{4}{15}\frac{S}{\omega_o} + \frac{1}{45}\frac{S^2}{\omega_o^2}}{\frac{2}{3}\frac{S}{\omega_o}},$$

$$\frac{e_1}{e_{in}} \approx \frac{1}{1 + \frac{4}{15}\frac{S}{\omega_o} + \frac{1}{45}\frac{S^2}{\omega_o^2}},$$

then the pair of equations represents a relatively simple network, namely a series *RLC* circuit where the voltage e_1 is taken across the capacitor. The complete network, with element values given in terms of the known device parameters, is shown in Figure 10.

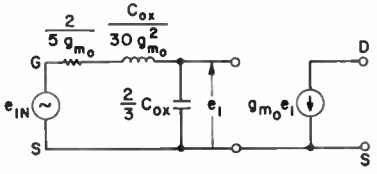

Fig. 10—Series resonant equivalent circuit.

The network appears intuitively plausible, as the transconductance in this model depends on the voltage across the capacitance (and therefore on the charge induced in the channel), and this voltage decreases with frequency because of losses in the equivalent input resistance. Furthermore, at low frequencies the input is capacitive, all of the input voltage is developed across the capacitance, and the drain current is given by its low-frequency value $g_{m_o} e_{in}$. Note that the equivalent input capacitance at low frequencies is (2/3) C_{ox} rather than C_{ox} as might be expected. That this value is correct can be verified by the following argument.

The channel voltage for $V_D > V_G - V_T$ was given by Equation (12(b)),

$$V(X) = (V_G - V_T)\left(1 - \sqrt{1 - \frac{X}{L}}\right). \qquad (12(b))$$

The oxide voltage, therefore, is

$$V_{ox}(X) = (V_G - V_T)\sqrt{1 - \frac{X}{L}}.$$

Thus, the charge per unit length on the gate electrode is

$$Q(X) = \overline{C}(V_G - V_T)\sqrt{1 - \frac{X}{L}} = \frac{\epsilon_{ox} W}{T_{ox}}(V_G - V_T)\sqrt{1 - \frac{X}{L}}. \quad (33)$$

Integrating Equation (33), we find

$$Q_{TOT} = \frac{2}{3}\int_0^L Q(X)\, dX = \frac{\epsilon_{ox} W}{T_{ox}}(V_G - V_T)\int_0^L \sqrt{1 - \frac{X}{L}}\, dX,$$

$$Q_{TOT} = \frac{2}{3}\frac{\epsilon_{ox} WL}{T_{ox}}(V_G - V_T) = \frac{2}{3} C_{ox}(V_G - V_T), \quad (34)$$

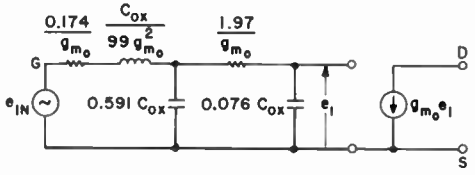

Fig. 11—Higher-order equivalent circuit.

which gives

$$C_{in} = \frac{d\, Q_{TOT}}{d\, V_G} = \frac{2}{3} C_{ox}.$$

Despite these intuitive confirmations, the equivalent circuit only roughly describes the transistor behavior at high frequencies, particularly for the input admittance. A more accurate version is obtained by adding one more term in S to both the numerator and denominator of Equation (32(a)) and yields a network valid up to $\omega = 12\omega_o$. This essentially is the useful region of operation, since g_m $(12\omega_o)$ is less than $0.35 g_{m_o}$. The network is shown in Figure 11 and was obtained by a Cauer expansion, removing zeros of transmission at $S = \infty$.

It is evident from the form and complexity of the circuit of Figure 11 that, although quite accurate, the practical use of the circuit for design and analysis purposes would be rather difficult. A solution to the apparent dilemma can be found by recalling the parameters that are of most interest for a device operating as a tuned high-frequency amplifier. The most important consideration at the input is the real part of

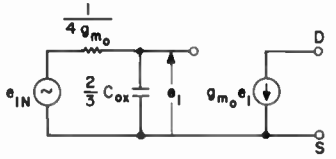

Fig. 12—Approximate equivalent circuit.

the input admittance, as this determines to a large extent the power gain of the amplifier as well as the Q of the input tuned circuit. For the output, however, a phase shift between the input voltage and the resultant drain current is usually not as important as the magnitude of the drain current. With these considerations in mind, an extremely simple equivalent circuit consisting of only a single resistance and capacitance can be derived, as shown in Figure 12. The element values of the circuit were chosen to fit the input admittance curves of Figure 5 as nearly as possible.

A plot of the input admittance versus frequency for this circuit is shown in Figure 14, and is seen to agree reasonably well with the exact expression. The magnitudes of g_m for each curve also compare favorably (see Figure 13) and, in fact, the above network predicts the 3-db for g_m exactly at

$$\omega = \frac{1}{RC} = \frac{6\, g_{m_o}}{C_{ox}} = 6\, \omega_o\,.$$

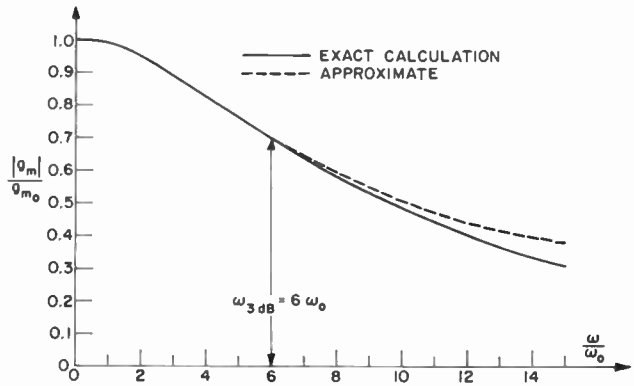

Fig. 13—Transconductance of approximate circuit.

Similar agreement is noted in the discussion of the transient response, which is derived in Appendix II. Thus, within a large portion of the useful frequency range, this approximate circuit* is a reliable representation of the transistor, and its use should considerably simplify circuit design and analysis of MOS transistor amplifiers at ultra-high frequencies.

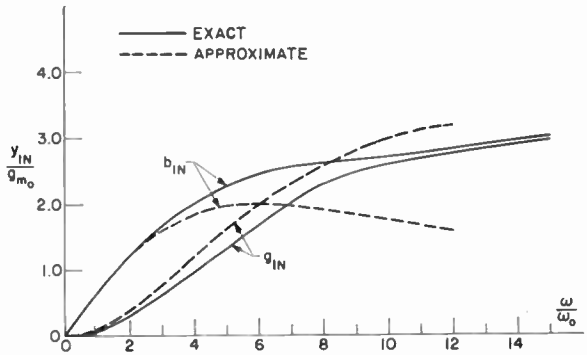

Fig. 14—Input admittance of approximate circuit.

D. Unilateral Power Gain

A useful figure of merit for an amplifying device is the unilateral gain.[10] This is an invariant quality and is defined as the maximum available power gain from a completely neutralized amplifier. In terms of the short-circuit admittance parameters, the gain U is given by (neglecting y_{12})

$$U = \frac{|y_{21}|^2}{4\, g_{11}\, g_{22}}.$$

In more familiar terms,

$$U = \frac{|g_m(\omega)|^2}{4\, g_{in}(\omega)\, g_{out}(\omega)}. \tag{35}$$

The gain can be expressed in normalized form with respect to the

* It should be noted that in Figures 9 through 12, the parallel drain conductance has been purposely omitted. This is accounted for in the evaluation of power gain that follows.

[10] S. J. Mason, "Power Gain in Feedback Amplifiers," *Trans. IEEE PTGCT*, Vol. CT-1, p. 20, June 1954.

low-frequency transconductance g_{m_o} as

$$U = \frac{g_{m_o}}{g_{out}(\omega)} \frac{\left|\frac{g_m(\omega)}{g_{m_o}}\right|^2}{4\frac{g_{in}(\omega)}{g_{m_o}}}.$$

If the assumption is made that $g_{out}(\omega)$ is constant with frequency (as is usually, though not always, the case), this relation can be given in a very convenient form:

$$U = A_{V_o} \frac{\left|\frac{g_m(\omega)}{g_{m_o}}\right|^2}{4\frac{g_{in}(\omega)}{g_{m_o}}}. \tag{36}$$

Here, $A_{V_o} = g_{m_o}/g_d = g_{m_o} r_d$ is the low-frequency amplification factor of the transistor.[11] The quantity U/A_{V_o} expressed in decibels is plotted in Figure 15 against the normalized frequency using the results obtained in Section III-A. [It should be pointed out that $U \to \infty$ as $\omega \to 0$ and is thus not a very useful figure of merit at low frequencies; of more interest at these frequencies is the voltage gain.] The curve shows that the loss in power gain with increasing frequency approximates a 6-db per octave fall off in the pass band of the device. In terms of the simplified single-time-constant model of the preceding section, U is given by

$$U = \frac{9}{4} A_{V_o} \left(\frac{\omega_o}{\omega}\right)^2. \tag{37}$$

This simplified relation is shown in Figure 15 to agree within ± 1 db over the frequency range $\omega_o \leq \omega \leq 15\,\omega_o$; although at higher frequencies ($\omega > 6\,\omega_o$), the power gain actually falls off at a rate exceeding 8 db per octave.

[11] S. R. Hofstein and G. Warfield, "Carrier Mobility and Current Saturation in the MOS Transistor," *Trans. IEEE PTGED*, Vol. ED-12, p. 129, March 1965.

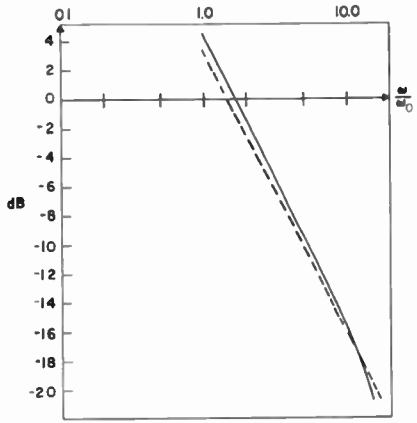

Fig. 15—Unilateral power gain versus frequency.

For a given A_{V_0}, the power gain drops to unity at a frequency ω_T given by

$$\omega_T = \frac{3}{2} \sqrt{A_{V_0}}\, \omega_0 \text{ Hz} \tag{38}$$

as determined by Equation (37). For frequencies higher than ω_T, the device is no longer useful as a power amplifier, and thus ω_T is analogous to the "maximum frequency of oscillation" commonly used as a high-frequency figure of merit for bipolar transistors.

The tetrode has been shown in III-B to have a poorer frequency response than the triode, but it was also shown that the output impedance was considerably higher at low frequencies. Thus, the tetrode is capable of higher maximum power gain than the triode. As shown in Figure 16, the tetrode connection can be represented as a 4-terminal network using the simplified equivalent circuit. The unilateral gain of the structure can then be determined from the y parameters of the net-

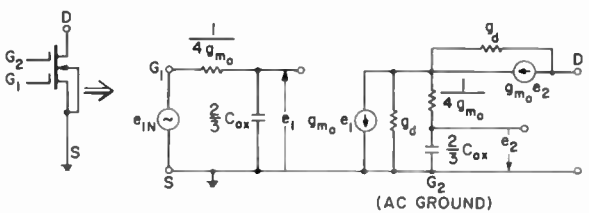

Fig. 16—Approximate equivalent circuit of tetrode.

work. Making suitable approximations ($g_d \ll g_{m_0}$), the unilateral gain for identical transistors is, from Equation (35),

$$U_{\text{TETRODE}} = \frac{\frac{9}{4} A_{V_0} \left(\frac{\omega_0}{\omega}\right)^2}{1 + \frac{4}{9}\left(\frac{\omega}{\omega_0}\right)^2} = \frac{U_{\text{TRIODE}}\, A_{V_0}}{1 + \frac{4}{9}\left(\frac{\omega}{\omega_0}\right)^2}. \tag{39}$$

The crossover frequency, where the power gains of the two connections become equal, is, therefore,

$$\omega_c = \frac{3}{2}\sqrt{A_{V_0} - 1}\,\omega_0 \approx \frac{3}{2}\sqrt{A_{V_0}}\,\omega_0 .$$

This is exactly the frequency ω_T defined in Equation (38) where the triode is no longer capable of power gain. Thus, for given transistors, the tetrode connection always has higher gain at any frequency, as long as the gain is greater than unity at that frequency.

It should be pointed out, however, that the frequency response of the tetrode is far from flat, falling off at a rate exceeding 12 db per octave. In applications requiring a wide range of tuning and large bandwidths, this could be particularly troublesome and lead to the use of complex and, therefore, expensive compensating networks to flatten the response.

IV. Relative Performance of the MOS and Bipolar Transistors

The high-frequency performance of the MOS transistor may be conveniently summarized by comparing it to the bipolar transistor, using the unilateral power gain as a basis for the comparison. It has been shown[12] for a bipolar transistor that

$$U \cong \frac{1}{8\pi^2 f^2} \frac{f_a}{r_{bb'} C_c} = \frac{\omega_a}{4 r_{bb'} C_c \omega^2}, \tag{40}$$

where ω_a is the α-cutoff frequency, $r_{bb'}$ is the base spreading resistance, and C_c is the collector junction capacitance. The similarity of the above

[12] R. L. Pritchard, "High-Frequency Power Gain of Junction Transistors," *Proc. IRE*, Vol. 43, p. 1075, Sept. 1955.

with the corresponding expression for the MOS transistor, Equation (38), is apparent. The gain of both devices decreases as $1/\omega^2$ and the quantities A_{V_o} and $1/(r_{bb}' C_c)$ are analogous measures of the output impedance. A more obvious similarity appears in the expressions for the factors ω_o and ω_a, which are both measures of the reciprocal transit time of carriers across the active regions. Equation (10) gives ω_o as

$$\omega_o = \frac{\bar{\mu}_n (V_G - V_T)}{L^2},$$

while ω_a is given by[13]

$$\omega_a \cong \frac{2.434\, D_B}{W_B^2}$$

where D_B is the diffusion coefficient for minority carriers in the base region and W_B is the base width. Using the Einstein relation $D = \mu(kT/q)$,

$$\omega_a = 2.434 \frac{\mu_B \left(\frac{k\,T}{q}\right)}{W_B^2}, \tag{41}$$

where kT/q is the so-called "thermal voltage" and is equal to 26 millivolts at room temperature. The two relations, Equations (10) and (41), clearly emphasize the physical and technological differences between the two types of device. In a bipolar transistor, charge carriers "drift" by diffusion at the thermal voltage within the silicon bulk, while in the MOS transistor, the carriers move at a drift velocity determined by the operating voltage $(V_G - V_T)$ and the effective mobility of the silicon surface. Similarly, the base width W_B is determined by the difference of two well-controlled vertical dimensions in the bulk, while the channel length L is a surface dimension limited by the resolution of the present photolithographic techniques. For present devices, ω_a and ω_o are about equal as the improvement due to the large ratio of $(V_G - V_T)$ to kT/q is nullified by the extremely narrow base width employed in the bipolar transistor.

Returning to the power gain Equation (40), the frequency where the power gain goes to unity for the bipolar transistor is

[13]R. L. Pritchard, "Frequency Variations of Current Amplification Factor for Junction Transistors," *Proc. IRE*, Vol. 40, p. 1476, Nov. 1952.

$$(\omega_T)_{\text{Bipolar}} = \frac{1}{2}\left(\frac{\omega_a}{r_{bb}' C_c}\right)^{1/2}. \tag{42}$$

A detailed calculation of this quantity has been made[14] for planar structure transistors. It was shown that

$$(f_T)_{\text{Bipolar}} = \frac{\omega_T}{2\pi} = \frac{(5 \text{ to } 12) \times 10^6}{D} \quad \text{Hz}$$

for a p-n-p germanium device of optimum design, where D is a surface dimension equal to the width of the emitter stripe in centimeters. It was estimated that for silicon transistors, f_T would be lower by a factor of two or more.

A corresponding figure for the MOS transistor can be obtained by assuming a maximum power-density limitation in the channel of P_o watts/cm². Assuming $V_D \approx (V_G - V_T)$ and I_o from Equation (8), P_o is

$$|P_o|_{\max} = \frac{\bar{\mu}_n \epsilon_{ox}}{2L^2 T_{ox}} (V_G - V_T)^3_{\max} \text{ watts/cm}^2 \tag{43}$$

where the area used is equal to WL. If it is further assumed that the substrate is lightly doped, then A_{V_o} is a constant factor given by[11]

$$A_{V_o} = \frac{\epsilon_{ox} L}{\epsilon_s T_{ox}},$$

where ϵ_s is the dielectric permittivity of the substrate. Substituting this expression into Equation (38)

$$(f_T)_{\text{MOS}} = \frac{\omega_T}{2\pi} = \frac{3}{4\pi}\left(\frac{\epsilon_{ox} L}{\epsilon_s T_{ox}}\right)^{1/2} \frac{\bar{\mu}_n}{L^2}\left(\frac{2 L^2 T_{ox} P_o}{\bar{\mu}_n \epsilon_{ox}}\right)^{1/3}$$

$$(f_T)_{\text{MOS}} = 0.3 \frac{(A_{V_o})^{1/6} (\bar{\mu}_n)^{2/3} (P_o)^{1/3}}{(\epsilon_s)^{1/3} L}. \tag{44}$$

[14] J. M. Early, "Structure Determined Gain-Band Product of Junction Triode Transistors," *Proc. IRE*, Vol. 46, p. 1924, Dec. 1958.

For $A_{V_o} = 20$, $\tilde{\mu}_n = 250$ cm^2/volt-sec, and $P_o = 10^4$ watts/cm^2,* which are typical values for a silicon device,

$$(f_T)_{\text{MOS}} = \frac{4.1 \times 10^6}{L} \quad \text{Hz}$$

for L in centimeters.

Thus, for the same surface dimensions, the present silicon MOS transistor is potentially within a factor of 3 of an optimized germanium bipolar transistor in gain–bandwidth product and would be at least comparable to a silicon bipolar transistor. Further, the MOS transistor has far superior cross-modulation distortion characteristics, particularly in the tetrode configuration,[7,8] and comparable noise figure which, in addition to the high-frequency performance, make it quite attractive in low-level r-f amplifier application.

ACKNOWLEDGMENT

This work represents part of the author's thesis for the Ph.D. degree in electrical engineering at Rutgers University, New Brunswick, N. J., and was carried out while on a David Sarnoff Fellowship at that institution. The author is indebted to Professor S. Fich of the Electrical Engineering Department at Rutgers for his many valuable suggestions, particularly on the use of the Laplace transform in distributed parameter systems, and to Professor J. L. Potter for his discussions and suggestions on equivalent circuit synthesis.

APPENDIX I—SOLUTION OF HIGH-FREQUENCY VOLTAGE AND CURRENT DISTRIBUTIONS IN THE MOS CHANNEL

If we take the Laplace transform of both sides of Equation (20) and normalize the complex frequency S to ω_o, an ordinary differential equation results for $\bar{\epsilon}\ (Z, S)$, which is, after some manipulation,

$$Z^2 \frac{d^2\bar{\epsilon}}{dZ^2} + Z\frac{d\bar{\epsilon}}{dZ} - \left(\frac{1}{4} + (Z)^{3/2} S'\right)\bar{\epsilon} = 0\,, \tag{45}$$

* The value of P_o is based on the power-handling capability of present enhancement-type transistors without a heat sink. It corresponds approximately to a device 10 mils wide by 0.2 mils long dissipating 125 milliwatts. Calculations based on power transistors of much larger area[15] yield an upper limit of about 400 watts/cm^2.

[15] G. C. Dacey and I. M. Ross, "The Field Effect Transistor," *Bell Syst. Tech. Jour*, Vol. 34, p. 1149, Nov. 1955.

where $\bar{\epsilon} = \bar{\epsilon}\ (X,S')$ is no longer time dependent, and $S' = S/\omega_o$. It can be shown that the solution of the above is

$$\bar{\epsilon}\ (Z,S') = C_1\, I_{2/3}\left(\frac{4}{3}\sqrt{S'}\,(Z)^{3/4}\right) + C_2\, I_{-2/3}\left(\frac{4}{3}\sqrt{S'}\,(Z)^{3/4}\right), \quad (46)$$

where $I_{2/3}$ is the modified Bessel function of the first kind and of order 2/3. From the boundary condition $\bar{\epsilon}\ (L,S') = 0$, we must have $C_2 = 0$ as $I_{-2/3}\ (0)$ approaches infinity. Invoking the other boundary condition, namely $\bar{\epsilon}/2 = \delta\ (S)$ at $X = 0$, where $\delta\ (S)$ is the input forcing function at the gate, the complete solution is

$$\frac{\bar{\epsilon}}{2} = \delta\ (S')\ \frac{I_{2/3}\left(\frac{4}{3}\sqrt{S'}\,(Z)^{3/4}\right)}{I_{2/3}\left(\frac{4}{3}\sqrt{S'}\right)}. \quad (47)$$

From Equation (16(b)), the incremental change in current can be obtained as

$$i\ (X,S') = \frac{\bar{\mu}_n\,\overline{C}}{2}\,\frac{d}{dX}\,(\bar{\epsilon}\,\overline{V}_o\ (X)) = -\frac{g_{m_o}}{2}\,\frac{\partial}{\partial Z}\,(\sqrt{Z}\,\bar{\epsilon}) \quad (48)$$

since

$$V_o = (V_G - V_T)\sqrt{1 - \frac{X}{L}} = (V_G - V_T)\,\sqrt{Z}.$$

Making use of the Bessel-function identities,

$$\frac{d}{dX}\,I_\nu\ (X) = \frac{1}{2}\,(I_{\nu+1}\ (X) + I_{\nu-1}\ (X))$$

and

$$\frac{2\nu}{X}\,I_\nu\ (X) = I_{\nu-1}\ (X) - I_{\nu+1}\ (X),$$

the complete solution for $i\ (Z,S')$ becomes

$$i\,(Z,S') = g_{m_o}\,\delta\,(S')\,(Z)^{1/4}\,\sqrt{S'}\,I_{-1/3}\left(\frac{4}{3}\sqrt{S'}\,(Z)^{3/4}\right) \Big/ I_{2/3}\left(\frac{4}{3}\sqrt{S'}\right). \quad (49)$$

The drain current, i_d, is the limit as $Z \to 0$ of $i\,(Z,S')$. For small values of the argument,

$$I_\nu\,(X) \approx \frac{\left(\frac{X}{2}\right)^\nu}{\Gamma\,(\nu+1)},$$

or

$$i_d\,(S') = \frac{g_{m_o}\,\delta\,(S')\,(S')^{1/3}}{\left(\frac{2}{3}\right)^{1/3}\Gamma\left(\frac{2}{3}\right)I_{2/3}\left(\frac{4}{3}\sqrt{S'}\right)} = g_m\,(S')\,\delta\,(S'). \quad (50)$$

As a check, taking the low-frequency limit, i.e., $S' \to 0$, and again using the Bessel-function approximation for small values of the argument gives

$$i_d\,(o) = \frac{g_{m_o}\,\delta\,(S')^{1/3}\,\Gamma\left(\frac{5}{3}\right)}{\left(\frac{2}{3}\right)^{1/3}\Gamma\left(\frac{2}{3}\right)\left(\frac{2}{3}\right)^{2/3}(S')^{1/3}} = g_{m_o}\,\delta,$$

since $\nu\,\Gamma\,(\nu) = \Gamma\,(\nu+1)$.

Expanding Equation (50) according to $i_\nu\,(X) = \sum_{n=0}^{\infty} \frac{\left(\frac{X}{2}\right)^{2n+\nu}}{n!\,\Gamma\,(n+\nu+1)}$,

$$g_m\,(S') = \frac{g_{m_o}}{1 + \frac{4}{15}S' + \frac{S'^2}{45} + \frac{8\,S'^3}{8910} + \ldots}. \quad (51)$$

The input admittance can now be readily obtained from Figure 3;

$$\frac{i_{in}(S')}{\delta(S')} = Y_{in}(S') = \frac{i_s(S') - i_d(S')}{\delta(S')} \tag{52}$$

$$Y_{in}(S') = g_{m_o}\left[\frac{-\frac{2}{3}S' + \frac{4}{45}S'^2 + \frac{2}{405}S'^3 + \dots}{1 + \frac{4}{15}S' + \frac{S'^2}{45} + \frac{8\,S'^3}{8910} + \dots}\right]. \tag{53}$$

Expanding Equation (50) with $Z = 1$

$$Y_s = \frac{i_s}{\delta} = \frac{1 + \frac{2}{3}S' + \frac{4}{45}S'^2 + \frac{2}{405}S'^3 + \dots}{1 + \frac{4}{15}S' + \frac{S'^2}{45} + \frac{8\,S'^3}{8910} + \dots}, \tag{54}$$

where i_s can be interpreted either as the source current due to a gate-to-source voltage $\delta(S')$ with the source grounded or as the current due to a source voltage $\delta(S')$ with the gate grounded. The latter interpretation is useful in considering the cascode arrangement for high-frequency MOS amplifiers.

Appendix II—Small-Signal Transient Response of MOS Triode

Considerable insight into the mechanisms that limit the high-frequency response of the MOS triode can be obtained by calculating the response of the drain current to a small step voltage applied to the gate input terminal. By calculation of the time for the drain current to reach its final value (or, more reasonably, 90% of its final value), an effective "transit time" can be defined. This in turn can be related to the previously computed steady-state response. In this problem, the input signal $\delta(S')$ becomes

$$\delta(S') = \frac{v_0}{S'} \tag{55}$$

where v_G is the height of the voltage step and $v_G \ll V_G$. The final value of i_d is then $g_{m_0} v_G$.

According to Equation (50) the transformed drain current for the above input is

$$i_d(S') = \frac{g_{m_0} v_G}{(S')^{2/3} \left(\frac{2}{3}\right)^{1/3} \Gamma\left(\frac{2}{3}\right) I_{2/3}\left(\frac{4}{3}\sqrt{S'}\right)} \tag{56}$$

Since $I_{2/3}(4\sqrt{S'}/3)$ is a polynomial of infinite degree in S having all positive coefficients, we obtain from the above equation and the initial value theorem of Laplace transform theory the conditions that

$$i_d(0) = 0, \tag{57}$$

and

$$\left.\frac{d^n i_d}{dt^n}\right|_{t=0} = 0, \; 1 \leq n \leq \infty.$$

These conditions state that not only is the initial value of drain current zero, but all of its initial time derivatives are identically zero as well. In effect, there will be a considerable time delay in the output current in addition to a finite nonzero rise time.

To find $i_d(t)$, it is necessary to take the inverse transform of Equation (2). This implies a knowledge of the zeros in the S plane of the denominator of this equation. The root at $S = 0$ is simple with a residue of $g_{m_0} v_G$, as can readily be seen by multiplying Equation (21) by v_G/S. The other poles are also simple and are determined by the zeros of $I_{2/3}(4\sqrt{S}/3)$. For any general function $F(S) = P(S)/Q(S)$ where the zeros of P and Q are simple and are not equal, the inverse transform $f(t)$ is[16]

$$f(t) = L^{-1}[F(S)] = \sum_{k=1}^{\infty} \frac{P(S_k)}{Q'(S_k)} \exp\{S_k T\}$$

[16] S. Fich, *Transient Analysis in Electrical Engineering*, p. 135, Prentice-Hall, Inc., Englewood Cliffs, N. J., 1951.

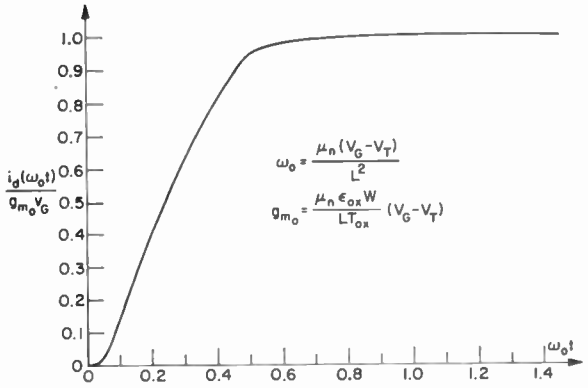

Fig. 17—Drain-current transient response.

which is in excellent agreement with the 3-db cutoff point obtained from the steady-state response of the transconductance.

STANDARD TEST-LAMP TEMPERATURE FOR PHOTOSENSITIVE DEVICES—RELATIONSHIP OF ABSOLUTE AND LUMINOUS SENSITIVITIES

By

R. W. Engstrom and A. L. Morehead

RCA Electronic Components and Devices
Lancaster, Pa.

Summary—Data were calculated to indicate the effect of changing standard lamp color temperature from 2870°K to 2854°K in order to promote a more universal standard for luminous photosensitivity measurements. It is shown that the proposed change would have little effect on already published values for most photosensitive devices.

Introduction

SINCE THE early 1940's, a tungsten lamp operating at a color temperature of 2870°K has served as the U.S. industrial standard for measuring the sensitivity of photosensitive devices. Although this standard color temperature is well established in this country, it has not received universal acceptance. For example, the NATO Committee on Image Conversion Tubes adopted a color temperature of 2854°K because of its use in Europe. Also, the C.I.E. has designated a tungsten lamp operated at 2854°K as Illuminant A. At present, the Committee on Photosensitive Electron Tubes of the Joint Electron Device Engineering Council of the EIA (Electronic Industries Association) is considering a change of the standard color temperature from 2870°K to 2854°K.

This paper shows that the adoption of either standard has little effect on already published sensitivity values for most photosensitive devices. The difference between values based on the two standards is in most cases insignificant.

Computer Study

A computer program was written, and the ratio (k) of the absolute sensitivity (at the wavelength of maximum response) to the luminous sensitivity was calculated for a number of industry standard

spectral response characteristics[1] at the two temperatures under discussion.* These values were computed from the relative spectral response of the photodevice, the emissivity of the tungsten filament, the optical transmission of the test-lamp envelope, and the standardized response of the human eye.[2]

Table I† gives the results of these calculations and compares the ratio of the conversion factors at the two temperatures. Previous data, published in 1960, are also shown in the table for comparison. For the calculations, the two color temperatures 2870°K and 2854°K correspond to actual temperatures[3] of 2817°K and 2802°K. Black-body calculations were made using a value of C_2 (from Planck's radiation formula) of 14,380 micron-degrees K; a value of 14388.4 was used for the 1960 data.[2] Emissivity values for tungsten were taken from DeVos[4]; envelope transmission data for the lamp were taken from Engstrom.[2]

Table I indicates that the more ultraviolet the spectral response characteristic, the larger the positive difference in the k values for the two temperatures; the more red–infrared the characteristic, the larger the negative difference in the k values. This trend is expected. The lower-temperature test lamp has less blue and ultraviolet output; therefore, the blue and ultraviolet spectral responses (relative to the human eye) have a lower luminous sensitivity value at the lower lamp temperature. On the other hand, spectral responses that are more red–infrared than the eye characteristic show a higher luminous sensitivity value at the lower temperature. Because k is the ratio of absolute sensitivity in amperes per watt to luminous sensitivity in amperes per lumen, a lower luminous sensitivity corresponds to a higher k value.

---

* For those users of photoelectric devices who require specific values of absolute spectral sensitivity (amperes per watt of input radiation), these k values may be used as conversion factors to relate absolute radiant sensitivity at the wavelength of peak radiant sensitivity to the luminous sensitivity (amperes per lumen).

† Two tables showing the specific data used in the calculations that resulted in Table I are available on request from the authors. One of these tables gives data on those spectral responses in Table I (see footnote (d) to Table I) that have not been standardized by the Electronic Industries Association. The second table shows data related to the computation of radiation from a tungsten lamp at the two color temperatures: the transmission of the envelope (taken from previous data[2]); the emissivities at the two color temperatures, 2870°K and 2854°K; and, finally, the radiation spectra.

[1] *Relative Spectral Response Data for Photosensitive Devices ("S" Curves)*, JEDEC Publication No. 50, Oct. 1964.

[2] R. W. Engstrom, "Absolute Spectral Response Characteristics of Photosensitive Devices," *RCA Review*, Vol. 21, p. 184, June 1960.

[3] G. A. W. Rutgers and J. C. DeVos, "Relation Between Brightness Temperature, True Temperature, and Color Temperature of Tungsten. Luminance of Tungsten," *Physica*, Vol. XX, p. 715, 1954.

[4] J. C. DeVos, "A New Determination of the Emissivity of Tungsten Ribbon," *Physica*, Vol. XX, p. 690, 1954.

Table I—Conversion Factors[a] for a Number of Spectral Response Characteristics at 2870°K and 2854°K Color Temperature and Related Data

Response Designation	Photo-Element	Type of Sensor	Window	Wavelength of Maximum Response, (nanometers)	Ratio of Absolute to Luminous Sensitivity-*k* (lumens per watt)			Difference Between 2854°K and 2870°K Conversion Factors (Present Calculations) Expressed in Percent
					1960 Data[2] 2870°K	Present Calculations 2870°K	2854°K	
S-1	Ag-O-Cs	Photoemitter[b]	Lime Glass	800	93.9	94.0	92.7	−1.3
S-3	Ag-O-Rb	Photoemitter[b]	Lime Glass	420	286	286	285	−0.4
S-4	Cs-Sb	Photoemitter[b]	Lime Glass	400	977	1036	1044	+0.8
S-5	Cs-Sb	Photoemitter[b]	9741 Glass	340	1252	1253	1262	+0.8
S-8	Cs-Bi	Photoemitter[b]	Lime Glass	365	755	754	757	+0.4
S-9	Cs-Sb	Photoemitter	Lime Glass	480	683	680	683	+0.5
S-10	Ag-Bi-O-Cs	Photoemitter	Lime Glass	450	508	508	509	+0.2
S-11	Cs-Sb	Photoemitter	Lime Glass	440	804	803	808	+0.6
S-12[c]	CdS	Crystal Photo-conductor	Epoxy and Lime Glass	502	4070	—	—	—
S-13	Cs-Sb	Photoemitter	Fused Silica	440	795	794	799	+0.6
S-14	Ge	p-n alloy junction	Lime Glass	1500	42.1	42.7	41.8	−2.2
S-15[c]	CdS	Polycrystalline Photoconductor	Lime Glass	580	352	—	—	—
S-16	CdSe	Polycrystalline Photoconductor	Lime Glass	730	160	160.5	158.7	−1.1
S-17	Cs-Sb	Photoemitter[b] Reflecting Substrate	Lime Glass	490	664	664	667	+0.5

Table I—(Continued)

Response Designation	Photo-Element	Type of Sensor	Window	Wavelength of Maximum Response, (nanometers)	Ratio of Absolute to Luminous Sensitivity-*k* (lumens per watt) 1960 Data[2] 2870°K	Present Calculations 2870°K	Present Calculations 2854°K	Difference Between 2854°K and 2870°K Conversion Factors (Present Calculations) Expressed in Percent
S-19	Cs-Sb	Photoemitter[b]	Fused Silica	330	—	1593	1603	+0.7
S-20	K-Na-Cs-Sb	Photoemitter	Lime Glass	420	428	429	428	0.0
S-21	Cs-Sb	Photoemitter	9741 Glass	440	779	778	783	+0.6
S-24[d]	K-Na-Sb	Photoemitter	7056 Glass	380	—	1490	1505	+1.0
—[d]	K-Cs-Sb	Photoemitter	7740 Pyrex	400	—	1108	1117	+0.8
—[d]	CdS	Polycrystalline Photoconductor	Lime Glass	510	—	642	643	+0.2
—[d]	Cd(S-Se)	Polycrystalline Photoconductor	Lime Glass	615	—	278	276	−0.6
—[d]	Si	n-on-p diffused junction	No Window	860	—	76.9	75.9	−1.4

[a] These conversion factors are the ratio of the radiant sensitivity at the peak of the spectral response characteristic in amperes per watt to the luminous sensitivity in ampers per lumen at the indicated color temperature.

[b] Opaque substrate; photoemission is from the side of incident radiation.

[c] The spectral responses indicated by S-12 and S-15 are essentially obsolete. S-12 represents the response of a crystal photoconductive cell which is no longer being manufactured. S-15 represents a polycrystalline photoconductor whose peak response at 580 nm is believed to have been the result of impurities; the CdS curve, which has a maximum at 510 nm, is more typical of today's state-of-the-art.

[d] Spectral response data for these photoelements have not been standardized to date by the Electronic Industries Association. The data used to make the calculations represent typical results of a number of spectral response measurements, but they have not been coordinated by the JEDEC Committee. Therefore, they must be considered as tentative RCA data only.

The minor discrepancies that exist between the k values calculated at 2870°K and those published in 1960 generally can be attributed to the slight change in C_2, rounding errors, and the greater accuracy of the computer calculations. However, the 1960 value for the S-4 response (977 lumens per watt) is apparently in error.

According to the nomograph of Rutgers and DeVos,[3] the color temperatures 2870°K and 2854°K correspond to true temperatures 2817°K and 2802°K of a tungsten ribbon. However, the nomograph is based on proportional radiation at two wavelengths, while "physiological" color temperature is the standard by which lamps are adjusted. Rutgers and DeVos estimate that the two definitions of color temperature differ by 30° at 3000°K. However, this estimate appears to be in error because of an error in transcribing the isotemperature lines given by D. B. Judd.[5] The actual difference between the two temperature definitions is negligible for the purpose of the present calculations.

Another possible error is that the data of DeVos are for a tungsten ribbon, and the actual test lamps used by RCA and by the industry in general are tungsten-coil filament types. No estimate of the difference is made, but the conclusions relative to the differences between the two standard temperature choices should not be affected.

Conclusions

Because photoelectric sensitivity is difficult to measure with an accuracy better than 5%, it is apparent that the adoption of either lamp-temperature standard is of small consequence relative to published sensitivity figures. It is recommended, therefore, that the 2854°K color-temperature standard be adopted for use in photosensitive measurements in the interest of international conformity. During the interim period, the data presented in Table I can provide conversion factors between the two specifications.

Acknowledgment

The authors thank C. I. Swanson and C. E. Young for their assistance in the calculation program.

[5] D. B. Judd, "Estimation of Chromaticity Differences and Nearest Color Temperature on the Standard 1931 I.C.I. Solorimetric Coordinate System," *J.O.S.A.*, Vol. 26, p. 421, 1936.

GIGAHERTZ TUNNEL-DIODE LOGIC

By

Michael Cooperman

RCA Defense Electronics Products
Camden, N. J.

Summary—This paper describes a logically complete set of tunnel-diode gates that is capable of operating at a gigahertz repetition rate. The logic family consists of OR, AND, and EXCLUSIVE OR elements. Operation is synchronous and the relatively high speed is obtained with a new technique of paralleling gates so that the gate recovery period is not wasted as in previously described tunnel-diode circuits. This results in an effective repetition rate that is twice that of the individual circuits. The circuits have been subjected to d-c worst-case tolerance analysis, computer analysis for dynamic operation, timing analysis, and experimental verification. The results were in basic agreement and indicated reliable operation with the specified device and power-supply tolerances.

A three-stage experimental model, using these gates to shift and perform logic, operated reliably at a gigahertz repetition rate with a power-supply tolerance of ± 5%. However, the d-c tolerance and computer analysis indicated that ± 1% for tunnel-diode peak currents and power-supply variation is required. Based on the latter tolerance specification, an allowable fan-in and fan-out of two each can be obtained. Based on the timing analysis, the maximum allowable clock timing tolerance is ± 12.5%. The circuits are simple in construction and employ relatively few devices. However, care must be used to keep stray reactance to a minimum.

Introduction

SOON AFTER the discovery of the tunnel diode, its potential as a high-speed digital device became evident. Widespread interest and work resulted in a number of tunnel-diode digital schemes that far exceeded the speed capabilities of transistor logic circuits. However, tunnel-diode circuits are subject to stringent component and power-supply tolerance requirements. These requirements are costly to achieve with present device processing and fabrication technology. This has severely limited the use of tunnel diodes in the highly competitive commercial computers.

In spite of the present handicaps, the tunnel diode remains in the forefront as a high-speed digital element in applications where speed

is of utmost importance. Tunnel diodes also retain their advantages of low power dissipation and high resistance to nuclear radiation.[1,2]

The extent to which the speed potential of the tunnel diode is used depends on its circuit configuration and on the mode in which it is operated. This paper describes a scheme by which the tunnel diode can be used more efficiently as a high-speed digital element and thereby provide increased speed. A new set of tunnel-diode logic circuits capable of 1000 MHz data rates are presented. The behavior of the individual circuits under static and dynamic conditions is analyzed. In addition, a timing analysis is performed to establish the capability for a large number of these circuits to operate together. Circuit operation is also evaluated with the use of a digital computer and finally verified experimentally.

Basic Operation of Tunnel-Diode Circuits

A. Operating Modes

The tunnel diode has properties that enable it to be used as a fast switching device. A typical tunnel diode exhibits a voltage-controlled negative resistance, as shown in Figure 1(a). With appropriate biasing, either a monostable or a bistable mode may be established.[3]

A circuit for obtaining these modes of operation is shown in Figure 1(b). Two possible biasing characteristics that might result from this circuit are shown superimposed on the tunnel-diode characteristic of Figure 1(a). Biasing characteristic I provides one stable operating point (monostable mode), point A, while biasing characteristic II provides two stable operating points (bistable mode), points A and C. (The intersection at point B is unstable.) Generally, these are the two basic modes that tunnel-diode logic circuits employ; both provide a practical way of obtaining amplification. The tunnel-diode switching mechanism is discussed in detail in Reference (4).

B. Effect of Operating Mode on Speed

The tunnel diode is inherently a regenerative rather than an output-follow-input element. In an output-follow-input element, such as the vacuum tube or transistor, the input always controls the output,

[1] G. R. Briggs and R. C. Ricci, "Five-Megacycle Magnetic Tunnel-Semiconductor Logic for Nuclear Radiation Environments," *Proc. Intermag Conference*, Washington, D. C. April 21-23, 1965.

[2] P. Gardner, R. Glicksman and R. H. Bergman, "Application of Tunnel Diodes to Micropower Logic Circuits," *Solid-State Electronics*, Pergamon Press 1964, Vol. 7, pp. 547-551.

[3] H. S. Sommers, "Tunnel Diodes as High Frequency Devices," *Proc. I.R.E.*, Vol. 47, p. 1201, July 1959.

i.e., when the input switches high, the output switches high (assuming no inversion) and when the input is removed, the output returns to the original state. This is not the case with the tunnel diode. The output follows the input when the input switches high, but once in the high state the output ceases to depend on the input and remains in the

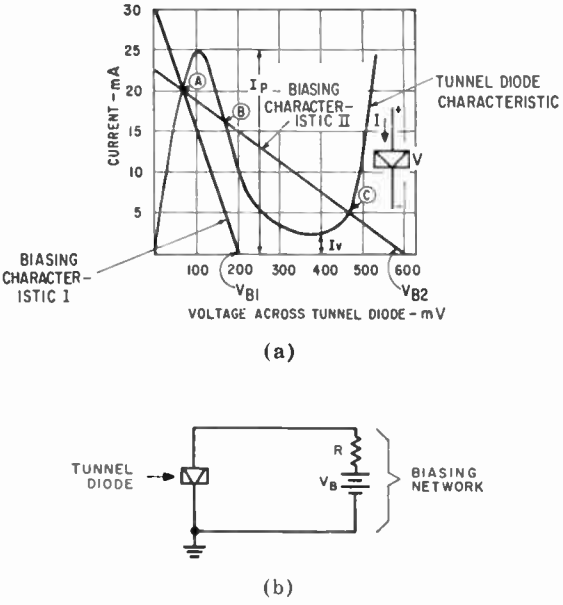

Fig. 1—(a) Two modes of tunnel-diode operation and (b) tunnel-diode circuit.

high state indefinitely. These are ideal features for a bistable element, a function the tunnel diode performs well. However, because its output is not always input dependent, difficulties arise in using the tunnel diode as a logic element when it must respond repeatedly to inputs. To solve this problem, some provisions must be included to unconditionally reset the tunnel diode after each input so that it will be ready to perform the same logic function again when the next input arrives.

One technique that solves this problem is to make the tunnel diode monostable, or self-resetting. This is illustrated in Figure 1 where, after the tunnel diode switches high, the current in biasing characteristic I decreases, thereby resetting the tunnel diode to its original state. Another technique is to operate the tunnel diode in a bistable mode, but to provide a properly synchronized reset after each input.

Both schemes have been used in the past,[4-8] and each has its advantages and disadvantages. In either case, however, the circuit must be reset, even when the next input will cause it to switch high again. This requirement for unconditional reset forces tunnel-diode circuits to operate in the return-to-zero (RZ) mode, which has a speed disadvantage compared to the non-return-to-zero (NRZ) mode.

In an NRZ system, setting accomplishes the transfer of a ONE and resetting the transfer of a ZERO, thus processing two bits in a set/reset operation. On the other hand, in an RZ system, the set/reset operation accomplishes the transfer of only one bit. Consequently, the time required to process one bit of information is the sum of the set and reset delays.

Logic Circuits

A. Parallel Tunnel-Diode Operation

The preceding discussion suggests that to use the inherent speed of tunnel diodes to fuller advantage, a dual tunnel-diode circuit should be used, where the second circuit processes data while the first is being reset. The set of circuits to be described operates on this principle, using tunnel diodes in the bistable mode with a reset after each logic level. However, while one tunnel diode is being reset and is getting ready for its next input, another circuit with the same logic function takes over. This effectively doubles the repetition rate over that obtainable with a single circuit.

The basic operation of this scheme is illustrated in Figure 2, which shows two identical circuits that are alternately enabled and disabled with a square-wave clock of 50% duty cycle. Each circuit is operational when the clock voltage is positive by several hundred millivolts; the circuit is inactive when the clock voltage is negative by several hundred millivolts and current is drawn from D_X or D_Y. In the case shown in Figure 2, TD_X is enabled during the time interval $0.2 \text{ ns} < t < 1 \text{ ns}$ and assumes the state of input B. TD_X operates in a bistable mode and consequently remains in the assumed state after

[4] R. H. Bergman, M. Cooperman and H. Ur, "High-Speed Logic Circuits using Tunnel Diodes," *RCA Review*, Vol. 23, p. 152, June 1962.
[5] M. Cooperman, "300-Mc Tunnel Diode Logic Circuits," *IEEE Trans. on Electronic Computers*, Vol. EC-13, p. 18, Feb. 1964.
[6] A. G. Samusenko, *Bistable with Reset Tunnel Diode Logic and Register Elements*, Master of Science Thesis, University of Pennsylvania, 1962.
[7] W. Peil, Y. C. Hwang and H. Raillard, "UHF Computer Circuits," *Proc. IEEE Pacific Computer Conference*, Pasadena, California, p. 163, March 15-16, 1963.
[8] J. S. Cubert and W. F. Chow, "Enhancement Tunnel Diode Nanosecond Logic Circuits," *Proc. IEEE Pacific Computer Conference*, Pasadena, Calif., p. 187, March 15-16, 1963.

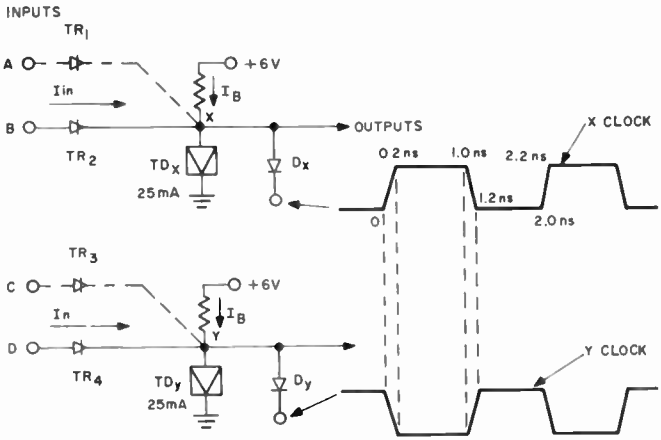

Fig. 2—Basic logic gate.

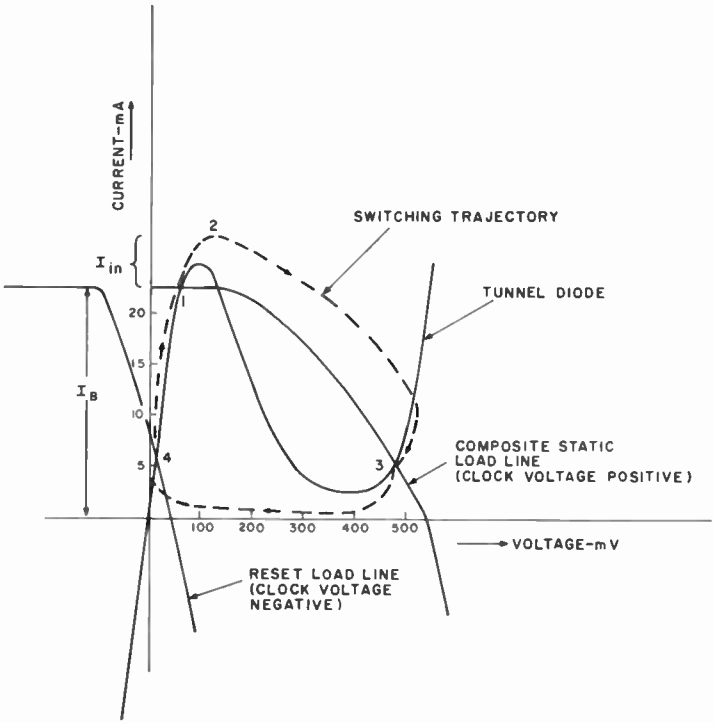

Fig. 3—Switching analysis of set and reset.

the removal of the input. During this same time interval, TD_Y is disabled. TD_Y is enabled during the succeeding time interval ($1.2\text{ ns} < t < 2.2\text{ ns}$), during which TD_X is disabled. The cycle is repeated with the roles of TD_X and TD_Y reversed.

The basic mode of operation is illustrated graphically in Figure 3. The static load line is a composite of the input load to the next stage and the reset diode D_X. When the clock voltage is positive, D_X is reverse-biased so that the load line is due entirely to the input of the next stage. Under these conditions, the circuit is in the active state and the two bistable points are 1 and 3, as indicated in Figure 3. When the clock voltage is negative, diode D_X conducts and the composite load line moves to the left, where it can have only one operating point, as indicated by point 4. Under these conditions, the circuit is inactive since the tunnel diode is biased so far from the peak that it cannot switch.

The sequence of operation is as follows. An input arrives at the circuit when the circuit is inactive (operating point 4). When the circuit is activated by the positive-going clock pulse, the composite load line assumes operating point 1. If the input is low ("low" indicates a logical ZERO and "high" indicates a logical ONE), the tunnel diode remains at operating point 1 since its peak is not exceeded. The output voltage and current to the next stage are essentially zero. If the input is high, $I_B + I_{in}$ exceeds the tunnel-diode peak and switching takes place along the indicated trajectory from operating point 1 to 3. The tunnel diode remains at operating point 3 as long as the clock voltage is positive. This state lasts from 0.2 ns to 1.0 ns. During this time, the tunnel-diode voltage is about 500 mV and it supplies an input current to the next stage. When the clock voltage becomes negative, the tunnel diode switches unconditionally from 3 back to 1 and remains in that state from 1.2 ns to 2.0 ns. Tunnel diode, TD_X, switches from the active, to the inactive state in the time interval of 1.0 ns to 1.2 ns. During this same time interval, TD_Y becomes activated and responds to an input in the same manner as TD_X did at 0.2 ns. Thus TD_X processes information while TD_Y is inactivated and TD_Y processes information while TD_X is inactivated.

When the output of TD_X is added to that of TD_Y, it can be seen that the combined circuit processes information at twice the rate of each individual circuit. The output need not be combined until the final logic function has been performed and it is driving a circuit of different type or a console indicator. When circuits of the same type are used, the rules are that an X circuit is always driven by a Y circuit and a Y circuit by an X circuit. The interconnection between

stages is illustrated in Figure 4(a). Figure 4(b) shows wave forms for one such stage.

The input is applied while the circuit is still inactive; when the circuit is activated, it assumes the state of the input before the input

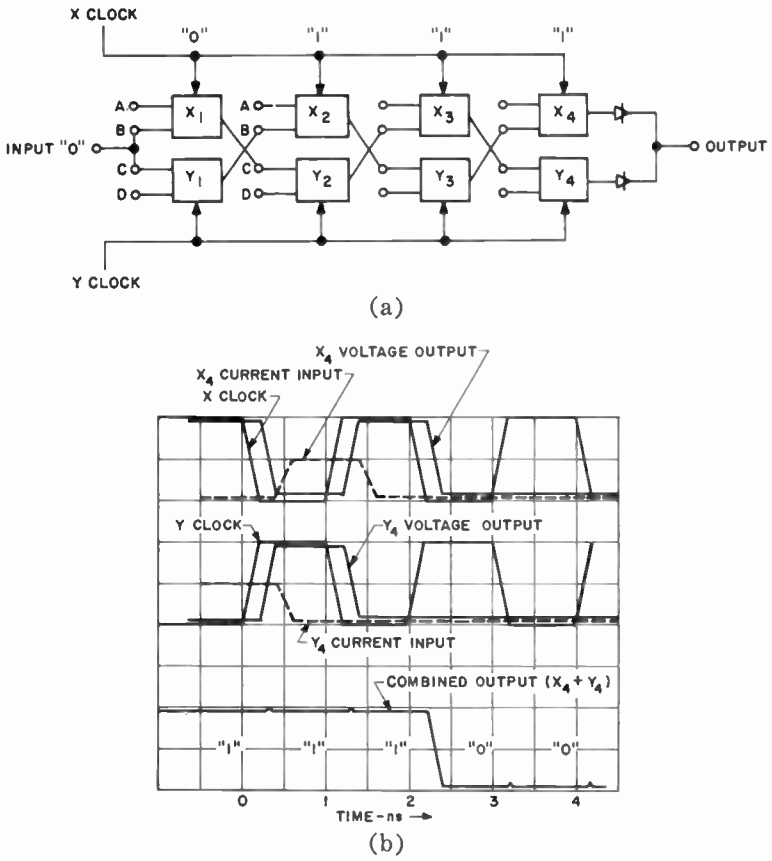

Fig. 4—(a) Interconnections between logic gates and (b) wave forms for one stage.

is removed. This overlap in information transfer is obtained from the accumulation of interstage delays—delays in the output tunnel diode, input tunnel rectifiers, and interconnecting transmission lines. The overlap requirements are discussed in more detail in a later section. The gate of Figure 2 can thus function as a delay unit or as a shift-register stage. When more inputs are added, as indicated by the dashed line in Figure 2, the circuit can function as an OR gate. By lowering the bias current or increasing the tunnel-diode peak so that

two inputs are required to switch over the peak, an AND function is obtained.

B. Exclusive OR Gate

To make the set of gates logically complete, an Exclusive OR gate is provided. This circuit is completely compatible with the basic OR gate. In addition to performing an Exclusive OR function, it also can be used for inversion. It is formed by adding a tunnel diode to the circuit of Figure 2, resulting in the circuit shown in Figure 5. The

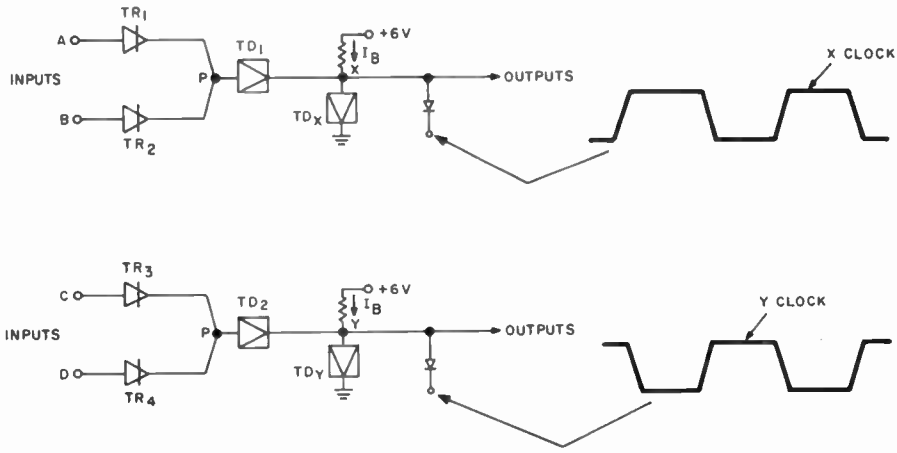

Fig. 5—Exclusive OR gate.

timing of the circuit is the same as before except the input is acted on by TD_1. When no input or only one input is high, the gate functions exactly as in Figure 2, since under these conditions TD_1 exhibits a very low resistance and for practical purposes, is a short circuit. However, when both inputs are high, the peak of TD_1 is exceeded, causing TD_1 to switch to the high state. In this state, TD_1 presents a high resistance that effectively disconnects both inputs from TD_X. This is illustrated graphically in Figure 6.

It is important to note that while TD_1 performs its logic function, TD_X is inactive and, for practical purposes, point X is grounded. This justifies the placement of the TD_1 characteristic as shown in Figure 6. The only supply of current to TD_1 is the currents from TR_1 and TR_2, which are shown superimposed as load lines on the characteristic of TD_1. These load lines with their operating points are shown for the following three conditions of operation:

(1) Both inputs are low (operating point 5) and TD_1 presents a relatively low resistance by being in the low state.

(2) One input is high (operating point 6) and TD_1 presents a relatively low resistance, since it is still below the peak. This permits an input to be supplied to TD_X.

(3) Both inputs are high and have caused TD_1 to exceed the peak and switch to point 7 along the indicated trajectory. In this state, the input to TD_X is limited by the relatively low valley current of TD_1, which effectively disconnects the inputs from TD_X.

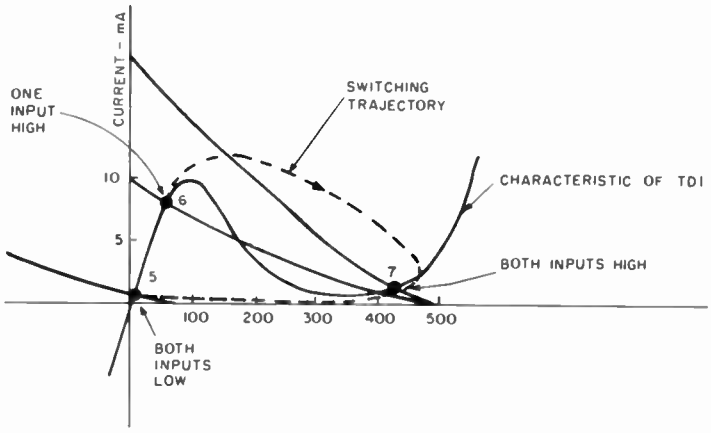

Fig. 6—Switching analysis of Exclusive OR gate.

Thus, when TD_X is activated, it switches to the high state only when either input A or input B, but not both, is in the high state.

While TD_X is activated, TD_1 is being reset (if it had been switched high) as the gates of its associated inputs are inactivated, thereby returning it from point 7 to 5 along the indicated trajectory. The function performed by this gate is identified as the Exclusive OR function, which may be represented by the Boolean expression $\bar{A}B + \bar{B}A$.

As shown in Figure 7, it would require five logic gates and three logic levels to perform an equivalent function with conventional logic gates. The Exclusive OR gate can also be used to provide inversion when one of its inputs always receives a logical ONE.

C. Interconnection of Logic Gates as a Shift-Register Generator

The Exclusive OR function is widely used in adders, comparators, and other important logic functions in general-purpose computers. It

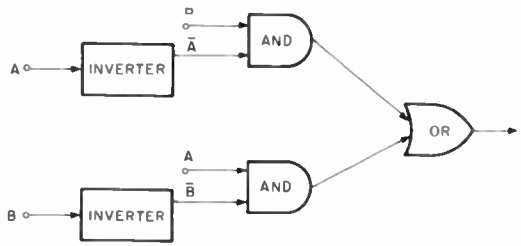

Fig. 7—Conventional logic implementation of Exclusive OR function.

is also used frequently to generate pseudo-random sequences for digital communications. An example of such a generator will be shown since it is very useful and it illustrates the interconnection and operation of the OR gate and Exclusive OR gate in a closed-loop circulating shift register with logic performed between shift-register stages. This type of interconnection illustrates the timing and tolerance requirements of the logic gates. Such a register is shown in Figure 8.

To trace the generation of the sequence, any starting state of the registers can be assumed. It is convenient, however, to start with the X portion active and storing all ONES and the Y portion inactive. This initial state is indicated for $t < 0$ in Table I, which also indicates the subsequent states for a complete sequence length. It is important to note the difference between a circuit being inactivated (indicated by a dash) and a circuit storing a ZERO (indicated by "0"). The

Table I—Circuit States of 3-Stage Shift-Register Generator

Time Interval (ns)	Stage							
	B	C	X_1 Y_1	X_2 Y_2	X_3 Y_3	X_1 and Y_1	X_2 and Y_2	X_3 and Y_3
$t < 0$	0	0	1 –	1 –	1 –	1	1	1
$0.2 < t < 1.0$	0	0	– 1	– 0	– 1	1	0	1
$1.2 < t < 2.0$	0	0	1 –	0 –	0 –	1	0	0
$2.2 < t < 3.0$	0	0	– 0	– 1	– 0	0	1	0
$3.2 < t < 4.0$	0	0	0 –	0 –	1 –	0	0	1
$4.2 < t < 5.0$	0	0	– 1	– 1	– 0	1	1	0
$5.2 < t < 6.0$	0	0	0 –	1 –	1 –	0	1	1
$6.2 < t < 7.0$	0	0	– 1	– 1	– 1	1	1	1

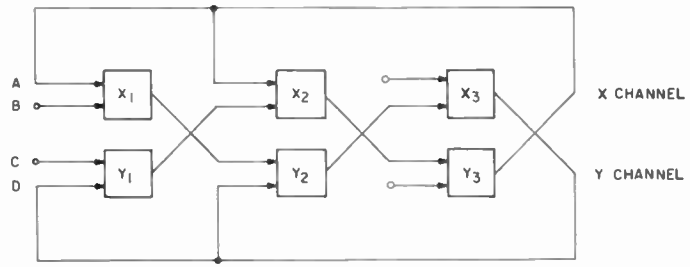

Fig. 8—Interconnection of logic gates as a shift-register generator (SRG).

storage of a ONE is indicated by "1". The corresponding timing wave forms are shown in Figure 9. It can be seen that when the two return-to-zero outputs (X and Y) are combined, an NRZ output results with the data being processed at a rate of 1 ns per bit, whereas in the individual X, Y circuits it is processed at 2 ns per bit.

D. Logic Requirements for High Speed

It can be shown that OR, AND, and INVERT functions are sufficient for a logically complete set of gates.[9] As shown in Figure 10, all of these functions can be obtained by combining the OR gate with the inversion provided by the Exclusive OR gate. Although such a

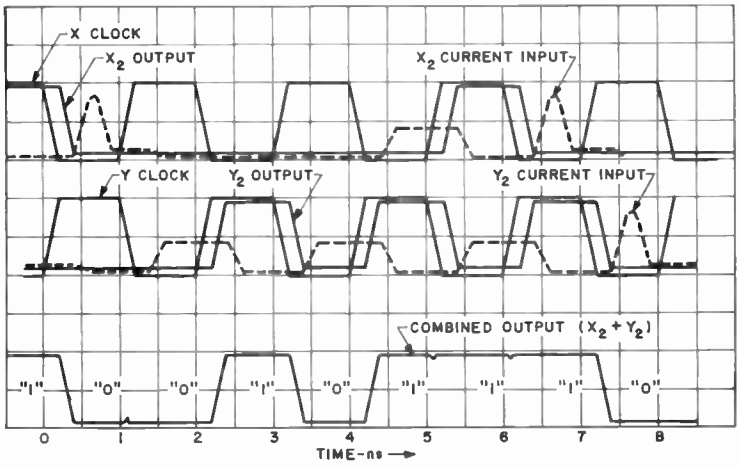

Fig. 9—Wave forms for second shift-register-generator stage.

[9] H. J. Gray, *Digital Computer Engineering*, Prentice-Hall, Inc., Englewood Cliffs, N. J., p. 68, 1963.

set of gates is satisfactory from the point of logical completeness, it has the disadvantage of requiring three logic levels to perform the AND function. Since the primary objective of this scheme is to increase high-speed capability, it is desirable to perform the AND function in one logic level. This is easily accomplished by increasing the peak currents of TD_X and TD_Y in the OR gate of Figure 2 so that two inputs are required for switching and producing an output.

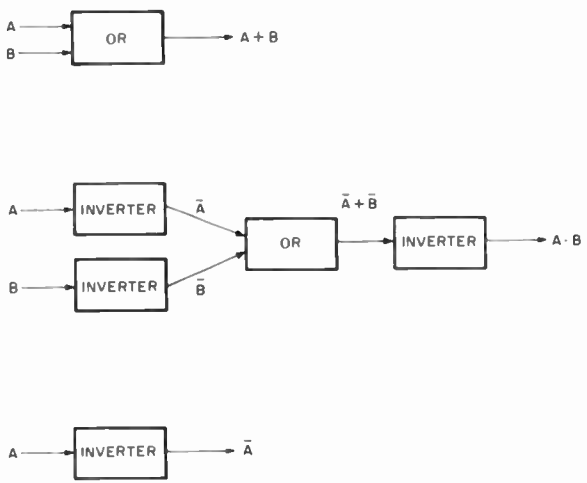

Fig. 10—Complete logic set.

Worst-Case Design

One of the first decisions in the design of tunnel-diode logic circuits is the choice of the peak currents that determine the magnitudes of the logic signal currents. Voltage swings are approximately 500 mV for germanium tunnel diodes and are independent of the tunnel-diode peak current. The available tunnel-diode peak currents were 2, 5, 10, 25, 35 and 100 mA. The lower peak currents have the advantage of lower operating currents, which take less time to build up; consequently, the inductive reactances are less bothersome. However, the ratio of I_P/C goes down, resulting in increased switching time. On the other hand, the high-current units have shorter switching times, but require a relatively longer time for current change. Consequently, stray capacitance presents less of a problem, but the effect of stray inductance is more pronounced. The 25- and 35-mA units were therefore chosen as a compromise between switching time and build-up or decay of current.

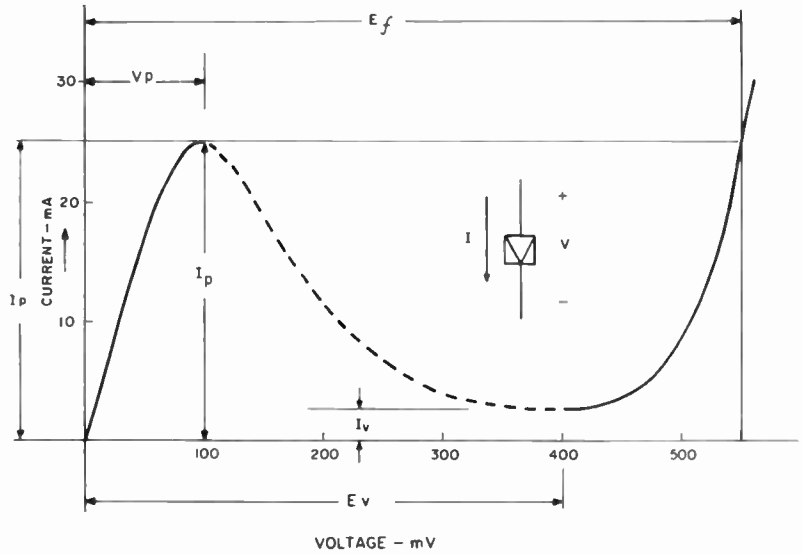

Fig. 11—Specification of tunnel-diode characteristic.

The parameters that specify the requirements of the tunnel-diode characteristic are defined in Figure 11. Tunnel rectifiers are used in the signal paths to provide isolation. A typical characteristic of a tunnel rectifier is shown in Figure 12. This rectifier is a tunnel diode with a very low peak current (in this case $I_p = 0.1$ mA). Consequently, for positive voltages that do not exceed 450 mV, it exhibits a rela-

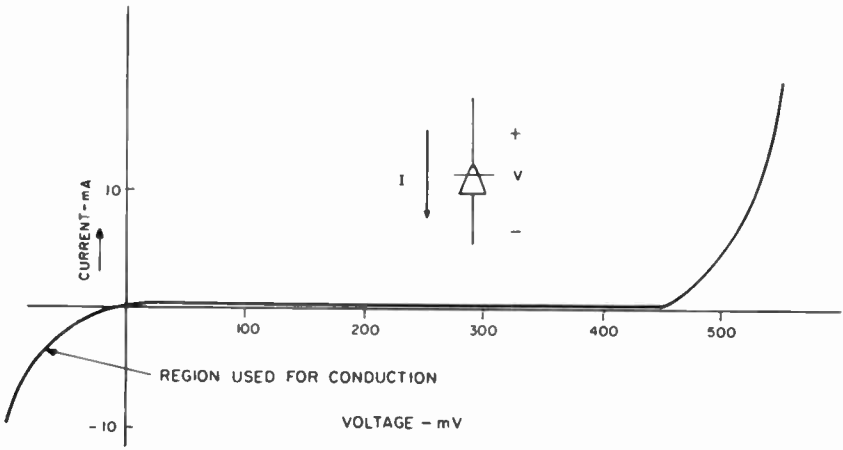

Fig. 12—Tunnel-rectifier characteristic.

tively high impedance (several thousand ohms). For negative voltages, it conducts immediately, thus providing diode action for voltages as low as 50 mV, depending on the individual device. The conduction region is considered the forward region, and in this operating region, the average resistance is about 20 ohms.

Circuit design is based on worst-case conditions. Several trial designs were performed with the tunnel diode chosen to determine the obtainable fan-outs and the required power-supply and component

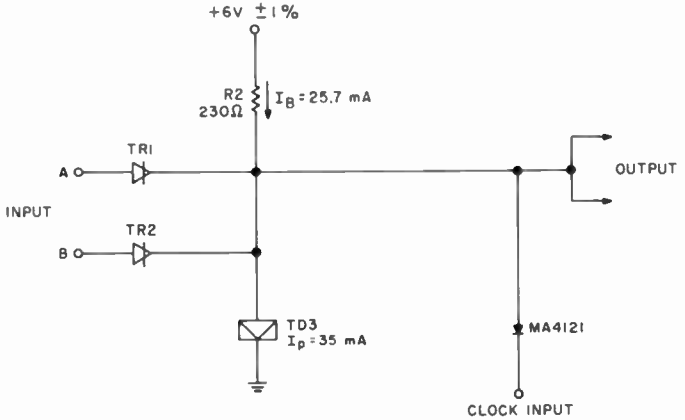

TR1; TR2; SAME AS IN "OR" GATE
TD3; I_p = 35mA ±1% V = 100 mV MAX, E_v = 400 mV MIN
E_f = 550 mV ±4% @ I = I_p

Fig. 13—AND gate circuit diagram.

tolerances. The following worst-case analysis is therefore a verification that the circuits will operate with the specified tolerances going to their extremes.

A. AND Gate

The function of this gate (Figure 13) is to provide an output when both inputs are high. Hence the following conditions must be satisfied.

(1) When both inputs are high and the gate is activated, the output must switch high. Consequently,

$$2I_H^- + I_B^- - I_{LO} \geqq I_p^+ + I_{OV} . \qquad (1)$$

(2) When only one input is high and the gate is activated, the out-

put must remain low. Consequently,

$$I_H{}^+ + I_B{}^+ + I_{Li} \leqq I_p{}^- - I_S \tag{2}$$

where

I_B = nominal bias current
I_H = input current when the input is high
$I_{Li} = 0$ = leakage into the tunnel diode
$I_{LO} = 1$ mA = leakage out of the tunnel diode
$I_{OV} = 1.4$ mA = overdrive (switching current above tunnel-diode peak)
$I_p = 25$ mA = nominal peak current of tunnel diode
$I_S = 1.5$ mA = safety current (amount of bias below peak for noise immunity)

The plus and minus signs indicate quantities going to their maximum and minimum extremes, respectively.

Assuming a $\pm 1\%$ variation in I_p, $\pm 2\%$ variation in I_B, and $\pm 5\%$ variation in I_H, Equations (1) and (2) can be solved for I_H and I_B as follows:

From Equation (1),

$$2I_H\,(0.95) + (0.98)I_B - 1 = (1.01)I_p + 1.4\,.$$

From Equation (2),

$$(1.05)I_H + (1.02)I_B + 0 = (0.99)\,I_p - 1.5\,.$$

From Equations (1) and (2),

$$I_H = 6.62 \text{ mA}$$
$$I_B = 25.7 \text{ mA}$$
$$I_H{}^- = 6.28 \text{ mA}$$
$$I_H{}^+ = 6.95 \text{ mA}$$

The AND gate was allowed to determine the allowable extremes on the inputs since it imposes the most severe restriction on the input tolerance.

B. Exclusive OR Gate

The function of this gate (Figure 14) is to provide an output only when an odd number of inputs is present. Here, the following condi-

tions must be satisfied:

(1) *Both Inputs High*—(a) TD_1 must conduct to shut off the inputs; consequently,

$$2I_H^- \geq I_{P1}^+ + I_{OV} \tag{3}$$

$$I_H^- = \frac{1.01I_{P1} + I_{OV}}{2} = \frac{10.1 + 0.4}{2} = 5.25 \text{ mA (actual } I_H^- = 6.2 \text{ mA)} ;$$

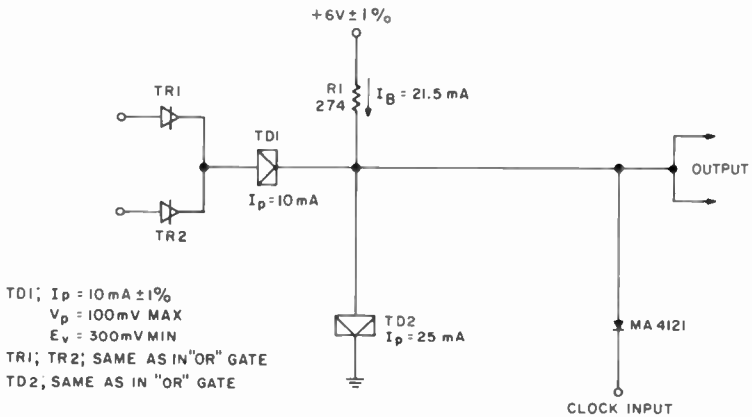

Fig. 14—Exclusive OR gate circuit diagram.

and (b) TD_1 must remain in the the high state to keep the inputs shut off; consequently,

$$2I_L^- \geq I_{V1}^+ . \tag{4}$$

Here, I_L is the input current when the input is low and I_{V1} is the valley current of TD_1. The worst cases of items (a) and (b) above are best illustrated in Figure 15 which shows that to satisfy Equation (4), I_{V1}^+ must not exceed 1 mA.

(2) *Both Inputs Low or Both Inputs High*—The output under these conditions should be low. Consequently,

$$I_B^+ + I_{V1}^+ \leq I_{P2}^- - I_{S2} , \tag{5}$$

where

I_{P2} = 25 mA = nominal peak current of TD_2
I_{S2} = 1.5 mA = safety current for TD_2
I_{V1}^+ = 1 mA = maximum valley current of TD_1.

From Equation (5),

$$(1.02)\ I_B + 1 = (0.99)\ 25 - 1.5\,,$$
$$I_B = 21.5\ \text{mA}.$$

Note that when both inputs are low, $I_{V1} = 0$. Consequently, Equation (5) is a worst case.

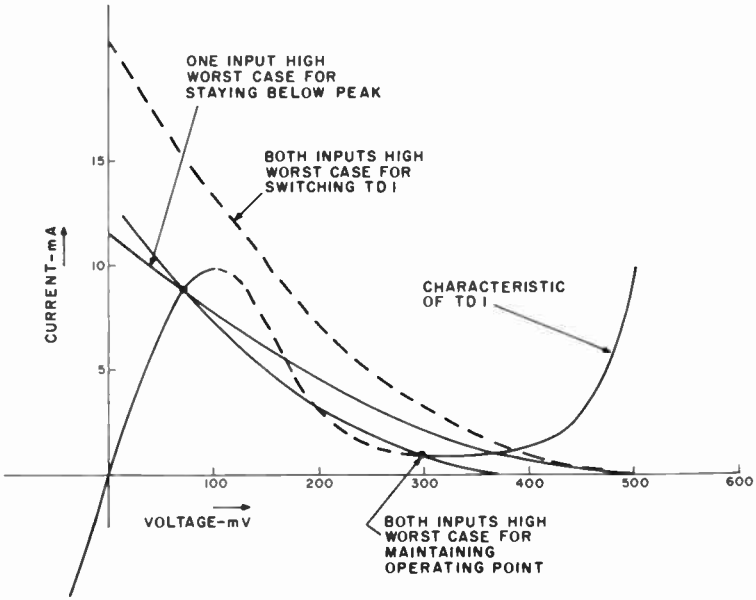

Fig. 15—Graphical representation of Exclusive OR worst cases.

(3) *One Input High*—Under these conditions, (a) TD_1 must not switch; consequently,

$$I_H{}^+ \leq I_{P1}{}^- - I_B \qquad (6)$$
$$I_H{}^+ = 0.99(I_{P1}) - 1.5 = 9.9 - 1.5$$
$$= 8.4\ \text{mA (actual } I_H{}^+ = 6.95\ \text{mA})\ ;$$

and (b) TD_2 must switch when activated

$$I_H{}^- + I_B{}^- \geq I_{P2}{}^+ + I_{LO} + I_{OV}$$
$$I_H{}^- = (1.01) I_{P2}{}^+ + I_{LO}{}^+ + I_{OV} - (.98)\ I_B$$
$$I_H{}^- = 25.25 + 1 + 1 - (21.5)\ (.98) = 6.05\ \text{mA (actual } I_H{}^- = 6.2\ \text{mA}).$$

C. OR Gate

The design of the Exclusive OR gate takes in all the design cases for the OR gate (Figure 16). The worst cases of the Exclusive OR gate are shown graphically in Figure 17, which shows the obtainable fan-out and the extremes of the output voltage. The maximum fan-out is determined by load line D. Load line D results when load line C is shifted to the left during the time when the following stage is inactivated, presenting the most severe loading condition by demanding a high current.

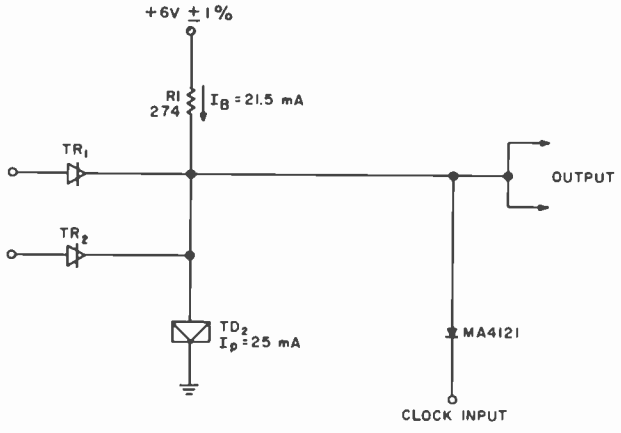

TD_2; I_p = 25 mA ±1%
V_p = 100 mV MAX
V_v = 400 mV MIN, V_f = 550 mV ±4% @ $I = I_p$
TR_1; TR_2; IS 11 mA @ 500 mV C = 1 pF MAX Ip = mA MAX

Fig. 16—OR gate circuit diagram.

System Timing

To establish the capability of a large number of gates operating together, a timing analysis was performed.[10] Timing provides information on how accurately the clock must arrive at each gate and the effect of its arrival accuracy on system speed. A portion of the system is shown in Figure 18, where information from X_1 is transferred into Y_2 by the phase Y clock. The time relations between the idealized clock and output wave forms are illustrated in Figure 19. The solid lines indicate operation under nominal timing conditions; the dashed

[10] H. J. Gray, *Digital Computer Engineering*, Prentice-Hall, Inc., Englewood Cliffs, N. J., p. 95, 1963.

lines indicate the region of timing tolerances over which the system will operate. These represent worst-case variations in arrival of clock phases, variation in clock pulse width, and variation in gate delay.

Before performing the timing analysis, gate delay will be defined. Since the switching of these gates is controlled by current rather than voltage, the delays will be defined in terms of currents, as indicated

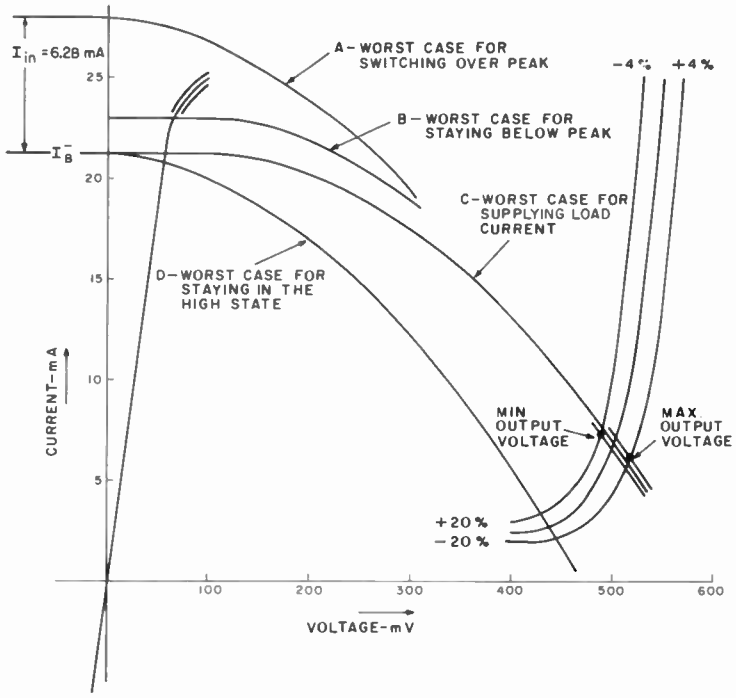

Fig. 17—Graphical representations of worst-case loading.

in Figure 20. In the noninverted output case, the clock must reach the indicated amplitude to initiate switching over the peak. The output current remains low until the tunnel diode switches over the peak, after which the output current builds up with rise time T_R. The delay, when referenced to the 50% points, is $T_R + d$. The inverted output has the additional delay of having to switch the tunnel diode of the next stage (see explanation of Figure 6). Consequently, in the inverted output case, the signal current has to build up as in the noninverted case and then decay after switching the tunnel diode. It, therefore, takes an additional fall time (which is equal to the rise time) for the inverted output. Thus, the inverted output delay is $2T_R + d$.

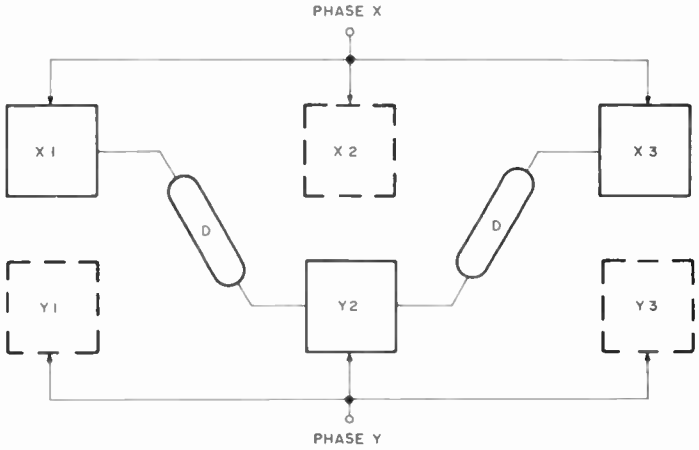

Fig. 18—Illustration of timing requirements.

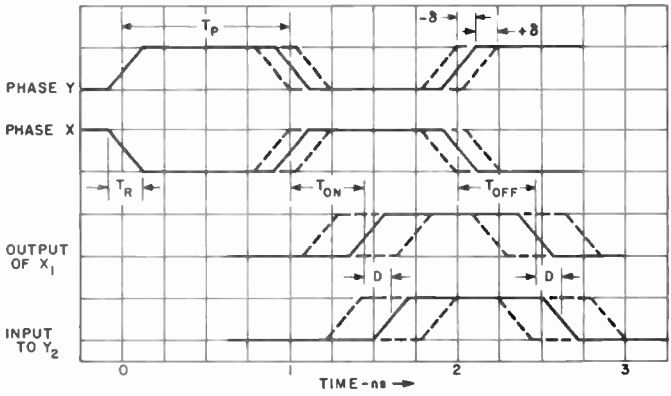

Fig. 19—Allowable timing tolerances.

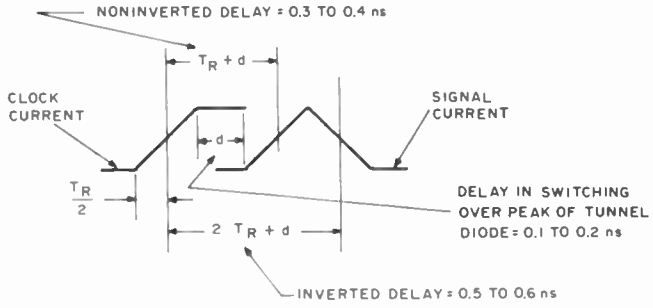

Fig. 20—Definition of delay.

Experimental results and calculations have indicated that the non-inverted output delay can vary from 0.3 to 0.4 ns and the inverted output can vary from 0.5 to 0.6 ns. For worst-case timing calculations, an overall delay variation of 0.3 to 0.6 ns will be assumed. Thus, the turn-on time (T_{on}) is defined as the delay required to establish a high or low level following a positive clock pulse transition. The turn-off time (T_{off}) is defined as the time required to inactivate a gate after a negative-clock-pulse transition.

A. Worst-Case Timing Conditions

(1) *Maximum-Delay Condition*

Referring again to Figures 18 and 19, the output from X_1 must arrive at Y_2 before phase Y goes high. If this condition is not satisfied, the output of Y_2 relative to the phase Y clock will have the inherent delay of X_1 added to that of Y_2. The output of X_3 will have the delay of X_1, Y_2 and X_3. It can be seen that after several stages, the signal will arrive too late (i.e., after the clock has gone low) and operation will stop. It is necessary, therefore, that the latest signal reach Y_2 before phase Y goes positive. Here, the effect of rise time will be included since it is of appreciable duration. This condition is expressed as the maximum-delay condition;

> Maximum delay in the turn-on of phase X + maximum gate delay + maximum external delay + ½ rise time ≤ earliest turn-on of phase Y + ½ rise time.

This gives rise to the equation

$$(T_P + |\delta|) + T^+_{on} + D^+ + (\tfrac{1}{2})\ T_R \leqq (2T_P - |\delta|) + (\tfrac{1}{2})\ T_R\,, \quad (7)$$

where T_P = nominal clock pulse width and nominal separation between phase X and phase Y
$|\delta|$ = magnitude of time deviation from T_P
T^+_{on} = maximum gate turn-on delay
D^+ = maximum external wiring delay
T_R = rise time.

(2) *Minimum-Delay Condition*

The second condition to be satisfied is that the phase Y pulse must go negative before the output of X_1 reaches Y_2. If this condition is

not satisfied, the output of X_1 may cause Y_2 to switch high just before phase Y is removed. If Y_2 was low during phase Y, a low output level should be transferred to X_3. However, the momentary switching of Y_2 could falsely transfer a high output level to X_3. This means that the earliest signal from X_1 must come later than the latest phase Y turn-off. This is called the minimum-delay condition;

Minimum delay in the turn-on of phase X + minimum gate delay + minimum external delay $\geqq$ latest turn-off of phase Y.

The minimum-delay condition gives rise to the equation

$$(T_P - |\delta|) + T^-_{on} + D^- \geqq (T_P + |\delta|) , \tag{8}$$

where

T^-_{on} = minimum gate turn-on delay
D^- = minimum external delay.

(3) *Minimum-Overlap Condition*

A third condition to be satisfied is that in order to transfer information from X_1 to Y_2, the output from X_1 must be maintained until Y_1 has started switching. If the output is removed too soon, Y_1 will fail to switch, resulting in loss of information. It has been found that it is sufficient to allow the output to start decreasing as soon as the clock has reached the indicated current level. This is called the minimum-overlap condition;

Minimum delay in turn-off of phase X + minimum gate delay + minimum external delay $-$ ½ fall time $\geqq$ latest turn-on of phase Y + ½ clock rise time.

Consequently,

$$(2T_P - |\delta|) + T^-_{off} + D^- - (\tfrac{1}{2})T_R \geqq (2T_P + |\delta|) + (\tfrac{1}{2})T_R . \tag{9}$$

B. Design for Optimum Timing Reliability

Experiments have indicated that, for practical purposes,

$T^+_{on} = T^+_{off} = 0.6$ ns,
$T^-_{on} = T^-_{off} = 0.3$ ns,
$D^+ = D^- = D$,
$T_R = T_f$ (all clock rise times and fall times are the same) $= 0.2$ ns.

From Equation (7),

$$T_P \geqq 2\,|\delta| + T^+_{on} + D. \tag{10}$$

From Equation (8),

$$|\delta| \leqq \frac{T^-_{on} + D}{2}. \tag{11}$$

From Equation (9),

$$|\delta| \leqq \frac{T^-_{off} + D}{2} - \frac{T_R}{2}. \tag{12}$$

Since $T^-_{off} = T^-_{on}$, the $|\delta|$ in Equation (12) is always smaller than that in Equation (11). Since a small $|\delta|$ represents a more stringent requirement, Equation (12) will be used.

By setting $T_P = 1$ ns (which corresponds to 1,000 MHz) in Equation (10),

$$\begin{aligned} D &\leqq T_P - T^+_{on} - 2\,|\delta| \\ &\leqq 1 - 0.6 - 2\,|\delta| \\ &\leqq 0.4 - 2\,|\delta|. \end{aligned} \tag{13}$$

From Equation (12),

$$\begin{aligned} D &\geqq 2\,|\delta| - T^-_{off} + T_R \\ &\geqq 2\,|\delta| - 0.3 + 0.2 \\ &\geqq 2\,|\delta| - 0.1. \end{aligned} \tag{14}$$

Equations (13) and (14) are plotted in Figure 21. Since both D and $|\delta|$ must be positive, the allowable values for D and $|\delta|$ are in the region indicated by the cross-hatched area. For optimum timing reliability, it is desirable to make the tolerable $|\delta|$ as large as possible. It can be seen from Figure 21 that this is obtained at the intersection of the two lines. Therefore, the system will operate reliably with a clock timing tolerance of $\delta = \pm 0.125$ ns, corresponding to a wiring delay of 0.15 ns. If the wiring delay is either reduced or increased,

a reduction in reliability will result. (The wiring delay can be maintained to within close tolerance.)

From the above illustration, it can be concluded that the optimum value of $D = D_{op}$ is obtained from the simultaneous solution of Equations (13) and (14) or Equations (10) and (12). Consequently, by

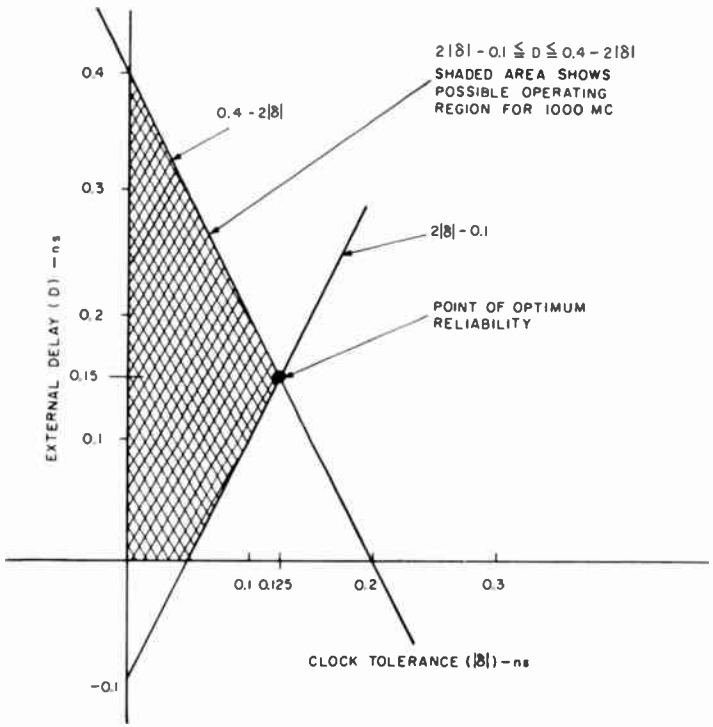

Fig. 21—Optimum timing design.

eliminating D between Equations (10) and (12), T_P is obtained as a function of δ under optimized conditions;

$$\begin{aligned} T_P &= 2\,|\delta| + T^{+}_{on} + 2\,|\delta| - T^{-}_{off} + T_R \\ &= 4\,|\delta| + 0.6 - 0.3 + 0.2 \\ &= 4\,|\delta| + 0.5\,. \end{aligned} \tag{15}$$

If we let $|\delta| = |x|\ T_P$, then

$$\begin{aligned} T_P &= 4\,|x|\ T_P + 0.5 \\ &= \frac{0.5}{1 - 4\,|x|} \quad \text{for } D = D_{op}\,. \end{aligned} \tag{16}$$

Equation (16), valid only for $D = D_{op}$, is plotted in Figure 22, which shows the effect of timing tolerance on the repetition rate. It shows that, for maximum speed, the clock timing tolerance should be kept to a minimum.

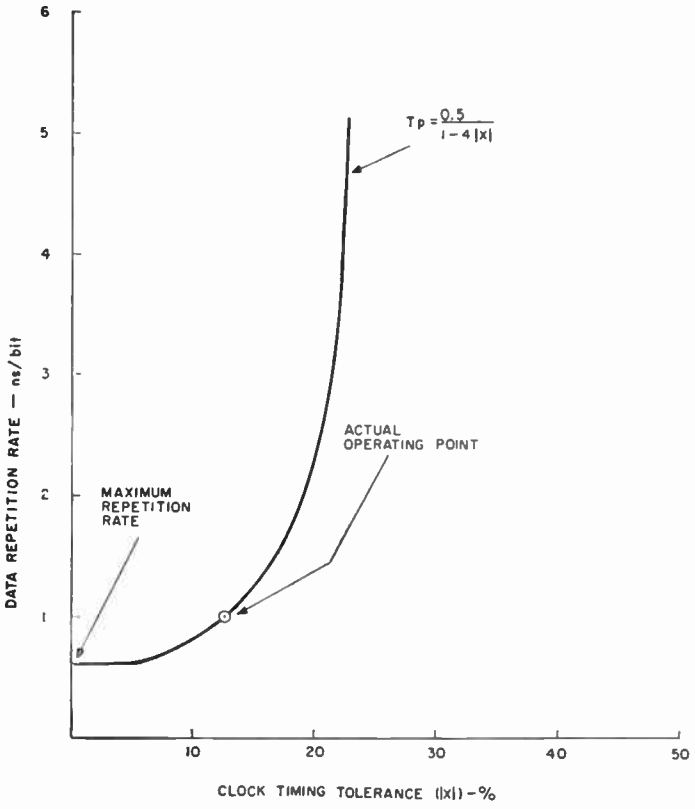

Fig. 22—Effect of clock tolerances on speed.

Computer Simulation

To provide more insight into the basic mode of operation, the circuit behavior was simulated with a digital computer. Computer analysis provides a means of comparison with laboratory results and indicates potential problem areas and the direction to be taken for obtaining improvement. In addition, once a program is written for a circuit, it is a relatively simple matter to change reactive elements and study their effect on performance. Computer analysis is especially useful with the speeds involved here, since components must be placed very close to-

gether to keep stray inductance to a very low value (0.5 nH), and this prevents the insertion of current-reading instruments in the circuit path. Since the circuits are current operated, it is of great value to know the current wave forms. They provide information on how close a tunnel diode comes to the peak due to transients when switching is not desired, or how much current overdrive is provided when switching is desired.

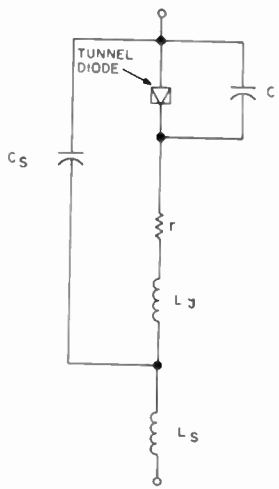

Fig. 23—Tunnel-diode equivalent circuit.

The equivalent circuit of a tunneling device is relatively simple, which makes it possible to analyze complex circuits employing many devices. A proposed equivalent circuit for the tunnel diode is shown in Figure 23, which shows an ideal tunnel diode with its passive and reactive elements.[3] In the circuit,

C_J = junction capacitance, which is somewhat nonlinear with voltage,
r = bulk resistance,
L_J = stray inductance inside the package,
C_S = stray capacitance of the package,
L_S = stray inductance outside the package.

It has been found that with negligible sacrifice in accuracy, the equivalent circuit can be simplified to that shown in Figure 24. Here, the tunnel diode includes the bulk resistance, and the junction capacitance (C_J) is considered constant. Experiments indicated that the

equivalent circuits of the other semiconductor diodes employed also could be approximated by the circuit shown in Figure 24.

The basic mode of operation was studied by simulating a complete Exclusive OR gate, as shown in Figure 25. This gate was chosen since it is the most complex and it includes all the modes of the OR gate and the AND gate. To provide all modes of operation and a direct comparison with experimental data, the output of the top circuit portion is connected to the input of the bottom portion; similarly, the output of the bottom portion is connected to the input of the top portion. This is the same connection employed experimentally in generating a 7-bit pseudo-random sequence.

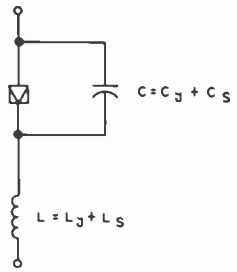

Fig. 24—Simplified equivalent circuit of tunnel diode.

The input-output connections have 0.2-ns delays inserted to prevent race conditions and loss of information. The 33-ohm resistors in series with the tunnel rectifiers were included as in the experimental model to provide the proper value of signal current. This was necessary since the available tunnel rectifiers had too low a voltage drop. Reset diodes D_1 and D_2 have 50-ohm resistances in series to simulate the characteristic impedance of the transmission line supplying the clock. The time-varying voltages $e_1(t)$ and $e_4(t)$ simulate the voltage waveforms supplied to the circuit from the preceding stage, while $e_2(t)$ and $e_3(t)$ simulate wave forms that could be present at the input of the following stage.

The simulated circuit is solved by numerical integration of a set of differential equations, each of which expresses the summation of currents at the numbered nodes. The nonlinear elements are approximated by straight-line segments that provide the required current–voltage relation used in the computation. Resistors R_2 and R_9 are included to simplify the equations of their nodes. The values of the reactive elements include the strays due to wiring. A special computer program was employed to deal with the delay and reflection introduced

by the transmission lines.[11] The computed wave forms are shown in Figures 26 to 31. To show the wave forms more clearly, the data rate was reduced to 2 ns per bit.

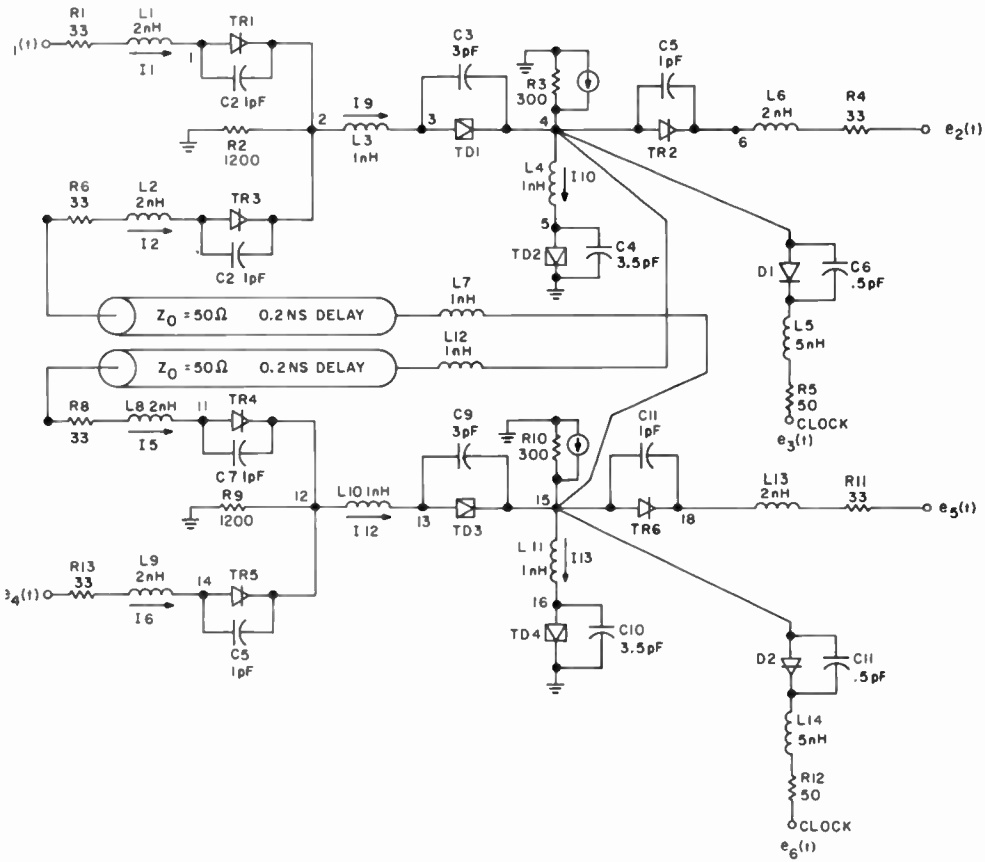

Fig. 25—Computer simulation of Exclusive OR gate.

Several cases deserve special attention:

(1) *Case I:*

At $t = 2$ ns, TD_4 is activated by $e_6(t)$. Since, at this time, I_5 and I_6 are low, I_{13} does not exceed the peak and V_{15} remains low. In the Exclusive OR gate and in the OR gate, this is the case when both inputs are low. In the AND gate, this is the case when one or both inputs are low.

[11] C. R. Pendred, "Transient Analysis of Transmission Lines with Nonlinear Terminations," *Proc. IEEE*, Vol. 52, No. 2, Feb. 1964.

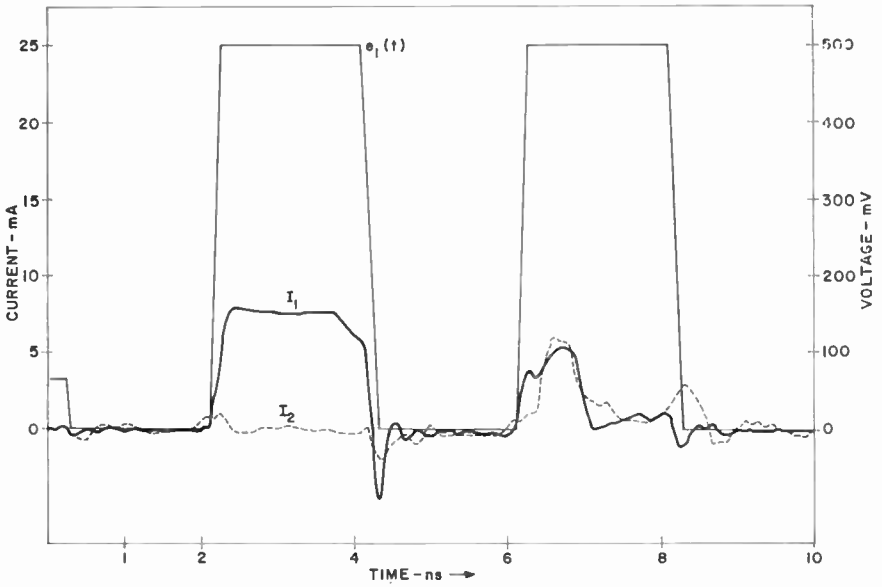

Fig. 26—Computed wave forms.

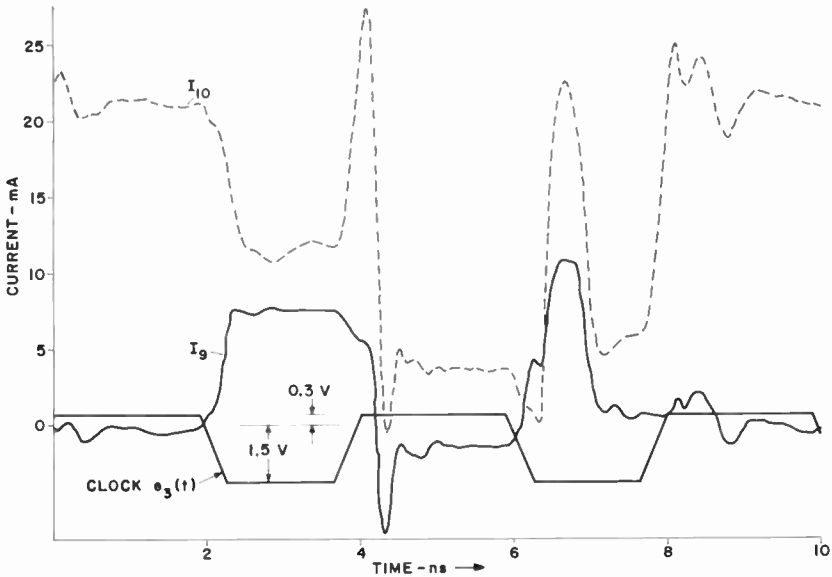

Fig. 27—Computed wave forms.

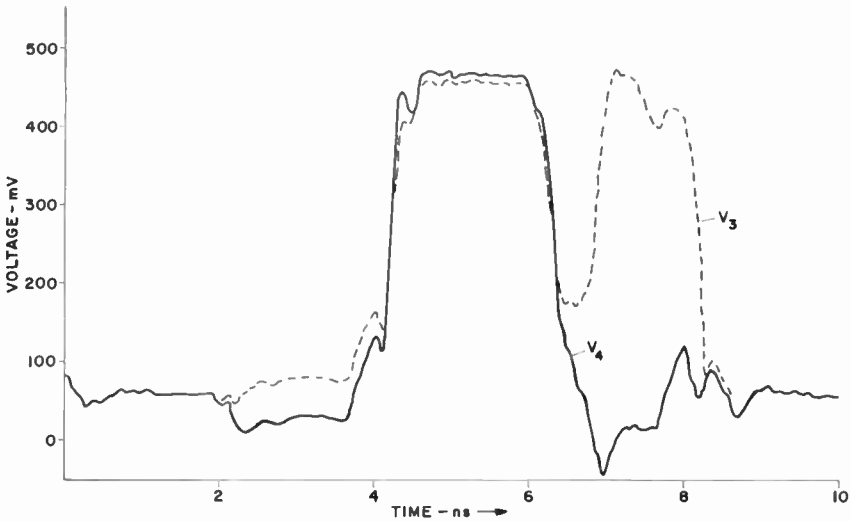

Fig. 28—Computed wave forms.

(2) *Case II:*

At $t = 4$ ns, TD_2 is activated by $e_3(t)$. Since, at this time, I_1 is high and I_2 is low, I_{10} exceeds the peak and V_4 switches high. In the Exclusive OR gate, this is the case when any one of the inputs, but not both, is high. In the OR gate, this is the case when one or both inputs are high. In the AND gate, this is the case when both inputs are high.

(3) *Case III:*

At $t = 6$ ns, TD_4 becomes activated by $e_6(t)$. Since, at this time, I_5 is high and I_6 is low, I_{13} exceeds the peak and V_{15} switches high.

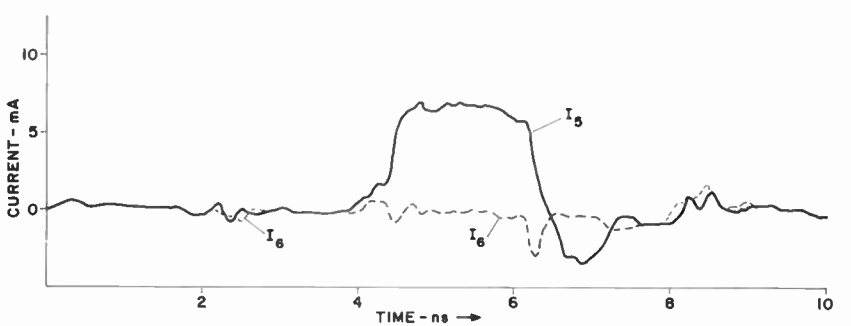

Fig. 29—Computed wave forms.

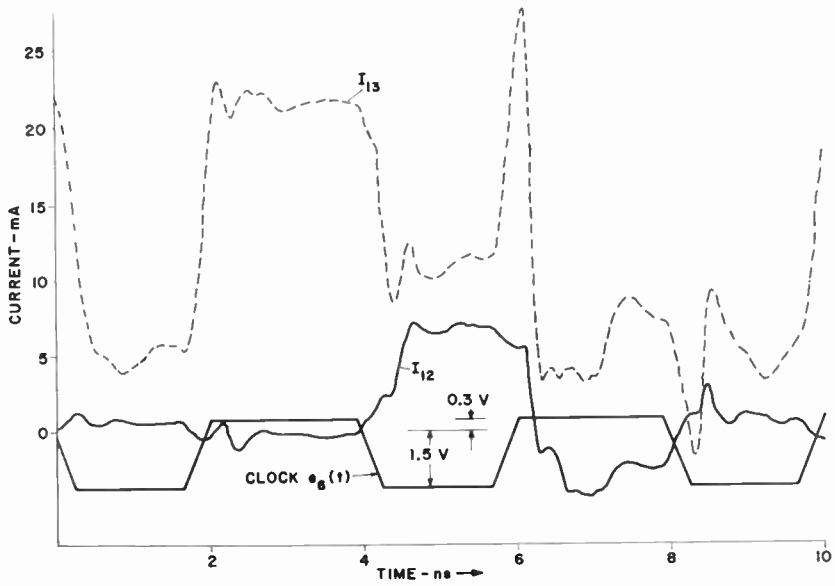

Fig. 30—Computed wave forms.

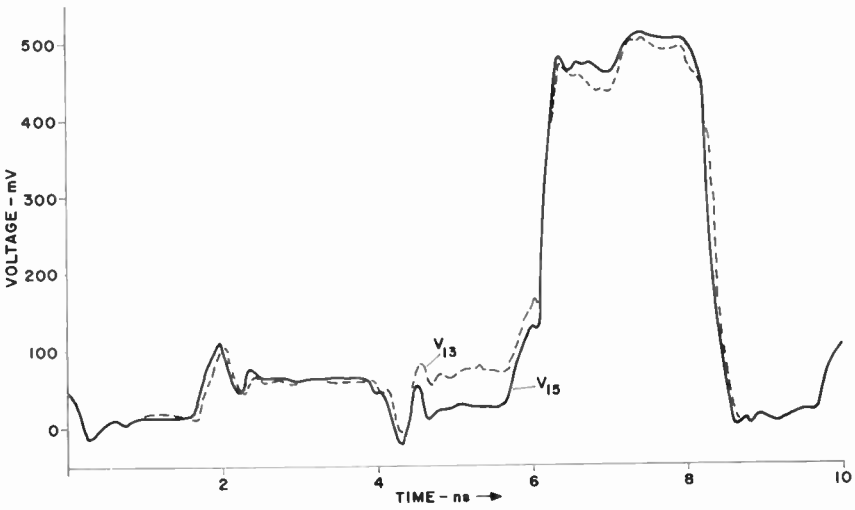

Fig. 31—Computed wave forms.

After a 0.2-ns transmission-line delay, the output of TD_4 is applied to the input of TD_2 making I_2 high. At the same time $e_1(t)$ is high which makes I_1 high. The sum of currents I_1 and I_2 exceeds the peak of TD_1 causing it to switch as evidenced by V_3. (Note, during this time, TD_2 is inactive and V_4 is low.) At about $t = 7$ ns, the input current to TD_2 which is designated by I_9, is switched low. Consequently, at $t = 8$ ns, when TD_2 is activated, I_{10} does not exceed the peak and V_4 remains low. This case applies to the Exclusive OR gate when both inputs are high.

Experimental Results

A 3-stage shift register was constructed and connected to operate as a shift-register generator to demonstrate the feasibility of this circuit approach. A complete circuit diagram of the three stages is shown in Figure 32. In the shift-register generator configuration, data was obtained on the ability of the circuit to shift and perform logic as well. The circuit consists of two shift-register gates and one Exclusive OR gate. Since the Exclusive OR gate is the most critical gate, this experiment imposes the most severe burden on speed. Considerably higher shift speeds can be attained when used as a shift register only, since the gate delay of the shift-register gates, as indicated in the discussion of system timing, involves no inversion and is, therefore, about half the Exclusive OR delay.

The circuits use only one +6-volt power supply and two sine-wave clocks 180° out of phase with each other. Sine waves were used for convenience, but computer analysis indicated that the use of square waves provides somewhat better performance, because to provide fast clock excursions, the sine-wave amplitude must be much larger than that of a square wave and consequently causes more capacitive feedthrough. A sine wave can be used instead of a square wave because the only requirement of the timing waveform is either (1) to deactivate the gate by causing conduction in the clock diodes during the negative cycle or (2) to activate the gate by reverse biasing the clock diodes during the positive cycle. The sine-wave amplitude need only exceed a certain minimum; beyond that point it merely increases the reverse bias on the clock diodes during the positive swing and provides more inhibit current during the negative swing. This additional inhibit current flows through the 25-mA tunnel diodes. However, due to the steep conduction of the tunnel diodes in that region, the tunnel-diode output voltage remains essentially at zero.

The three stages are connected to generate a maximum length pseudo-random sequence. In general, the length of such a sequence is

$2^n - 1$, where n is the number of register stages.[12] For three stages, the sequence repeats every seven bits. Figure 33 shows such a sequence generated at a 400-MHz bit rate. The corresponding phase clocks

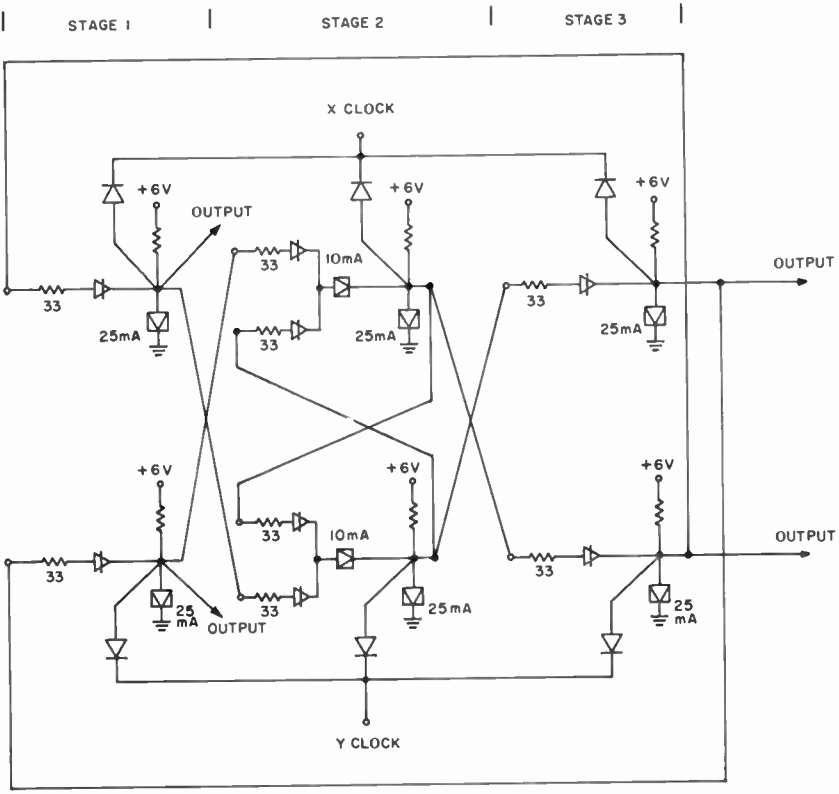

Fig. 32—Laboratory circuit of 3-stage shift-register generator.

are shown in Figure 34. The X and Y outputs each generate two return-to-zero sequences at bit rates of 200 MHz. When superimposed as shown, they result in an NRZ sequence at a 400-MHz bit rate. Operation of the circuit at a bit rate of 1 ns or 1,000 MHz is shown in

[12] T. G. Birdsall and M. P. Ristenbatt, "Introduction to Linear Shift-Register Generated Sequences," University of Michigan Technical Report No. 90, Oct. 1958.

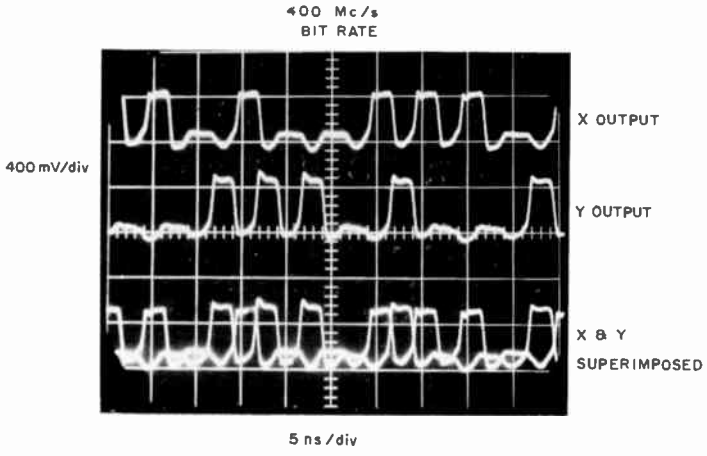

Fig. 33—Output wave forms of Figure 32 (400-MHz bit rate).

Figure 35. Under these conditions, reliable operation was achieved with a power-supply tolerance variation of ±5%.

Figure 36 shows a photograph of the experimental breadboard. One half contains three stages connected as a shift-register generator that drives three other logic gates of the same type. In the construction, extreme care had to be taken to keep stray inductance and capacitance to a minimum. Some of the interconnecting lines on top are visible; other lines are on the bottom. They are miniature coaxial lines varying in length between 0.5 and 1 inch. All gates have a fan-in of two and a fan-out of two.

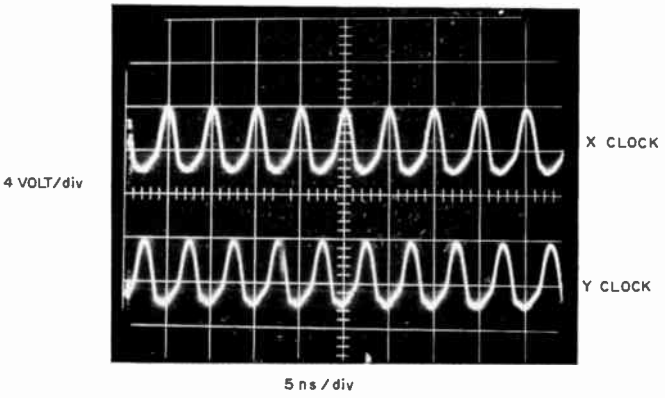

Fig. 34—Clock wave forms of Figure 32 (400-MHz bit rate).

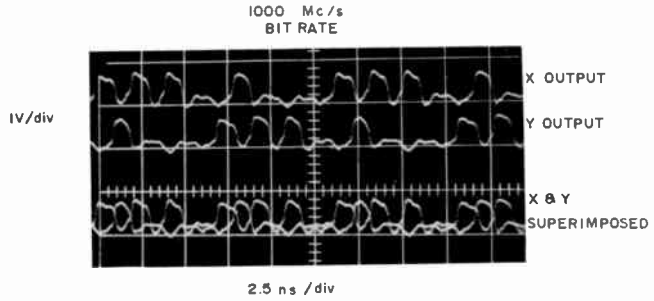

Fig. 35—Output wave forms of Figure 32 (1000-MHz bit rate).

CONCLUSIONS

A set of tunnel-diode logic gates capable of operating at a gigacycle repetition rate has been presented, together with d-c worst-case tolerance analysis, computer analysis for dynamic operation, timing analysis, and experimental verification. The results are in basic agreement and indicate reliable operation with the specified device and power supply tolerance.

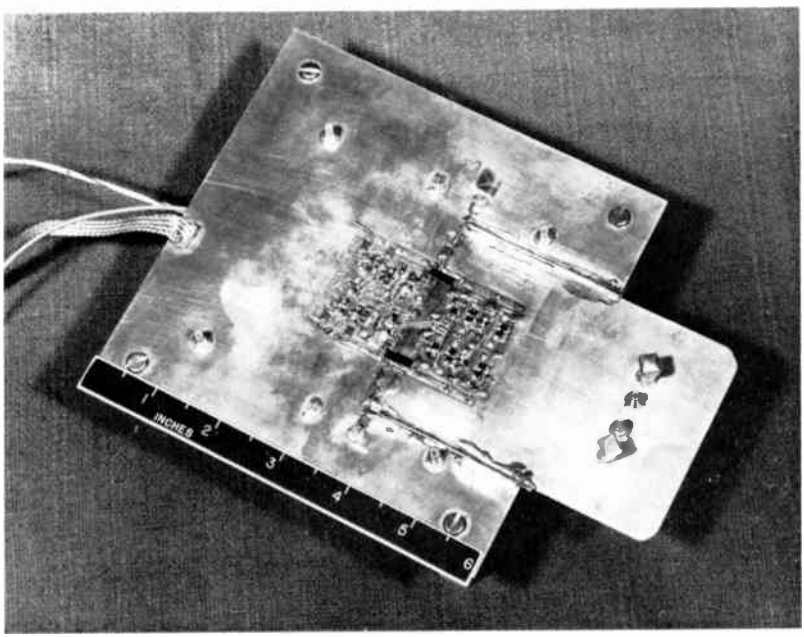

Fig. 36—Breadboard of six logic gates.

A three-stage experimental model, using these gates to shift and perform logic, operated reliably at a gigacycle repetition rate with a power-supply tolerance of ±5%. However, the d-c tolerance and computer analysis indicated that a variation of ±1% is required for tunnel-diode peak currents and power supply. Based on the latter tolerance specification, an allowable fan-in and fan-out of two each can be obtained. Based on the timing analysis, the maximum allowable clock timing tolerance is ±12.5%. The circuits are simple to construct and employ relatively few devices. However, care must be used to keep stray reactances to a minimum.

The analysis and experimental observations indicated the potential for operation at considerably higher speeds. In the experimental shift-register generator, data is logically manipulated and then shifted in a total time of 1 nanosecond for both operations. Less than half of this time is used in the shifting process. It therefore appears possible that shift registers could be built to operate at twice the present gigahertz speed.

Acknowledgment

The work described in this paper was performed in partial fullfilment of the requirements toward receiving the M.S.E. Degree from the University of Pennsylvania. The author wishes to thank his advisor, Dr. H. J. Gray, of the Moore School of the University of Pennsylvania. He also wishes to thank C. R. Pendred for his support in computer circuit simulation, W. P. Palanker for the assistance in the experimental work, and R. K. Lockhart and R. H. Bergman for their interest and encouragement throughout the program.

THE RESOLVING-POWER FUNCTIONS AND QUANTUM PROCESSES OF TELEVISION CAMERAS

By

OTTO H. SCHADE, SR.

RCA Electronic Components and Devices
Harrison, N. J.

Summary—The resolving power of an imaging system is a significant figure of merit when given as a function of object contrast and exposure. It is shown that the resolving-power functions can be expressed in terms of the quantum densities and transfer functions of the imaging system without recourse to specific electronic or photographic units for which conversion factors or equations are given. The formulation is general, without restriction to specific systems. The quantum densities in the storage surfaces of television camera tubes and the mechanism of signal transfer by the electron reading beam are discussed in detail to determine the constants and parameters for the calculation of resolving-power functions for a variety of operating modes, including continuous and single-image readouts. It is shown that resolving powers exceeding 100 cycles/mm are obtainable with high-quality electron optics.

I.—INTRODUCTION

THE PRINCIPAL purpose in most applications of a high-definition imaging system is the detection and recognition of the fine structure of small objects over a large range of object contrasts. Given as a function of object contrast and exposure, the resolving power becomes a significant figure of merit. It is a function of all system parameters—the gain, frequency transfer function, and granularity or noise level of the system. A low-noise system having a moderately good frequency response can provide the same resolving power as a system having a considerably higher frequency response and higher noise level, particularly at low object contrasts.

High signal-to-noise ratios in small areas require, in principle, a high particle, or quantum, density, i.e., a large number of photons, electrons, or grains per unit area. It follows that high resolution can be obtained at very low levels of illumination only by long time exposures and accumulation of quanta in a suitable storage surface. Therefore, when the gain of a system is increased by the addition of multiplier or intensifier stages to compensate for reduced photon* input

* Photon in this paper is used as a unit of radiation energy. It is not meant to imply a "noisy" flow of random quanta.

(for low light-level operation), the resolving power of a theoretically perfect system decreases. However, because a practical system contains additional noise sources that may limit performance more than noise in the photon conversion process, the resolving power of a practical system may be increased at low light levels. The usefulness of signal-intensifier stages depends on the location and value of the noise sources in the system. It further depends on the frequency characteristic of the intensifier stage, which must be considerably better than that of the remaining system elements in order not to offset a decrease in overall noise by a decrease of high-frequency signals.

The calculated values of resolving-power functions can be used to predict the performance of an imaging system and evaluate proposed changes in system elements intended to improve the sensitivity or the general performance of the system.

The performance of a photographic or electronic imaging system is determined by the transfer functions and granularity of its imaging stages. In general, the information transferred through the system is described basically by the variation of particle density in a sampling area $\bar{a}$ as a function of the image coordinates. The input radiation energy is directed by a lens to an imaging surface. In an electronic (television) camera, the radiation energy excites electrons in a photosensitive surface. This process is subject to statistical variations.* The excited electrons are stored as a charge image in the storage surface. An unmodulated electron stream (the reading beam) is injected and absorption-modulated as it neutralizes the charges. After considerable amplification, the signal modulation is transferred to an electronic writing beam and converted back to a spatial light modulation on the image surface of a display tube (picture tube).

In a photographic camera, the radiation energy releases electrons in the emulsion of the photographic film. The electrons are converted and stored as a silver atom image. In a subsequent development process the silver atoms are amplified to much larger grains, forming a visible negative image. For reversal of polarity, the spatial modulation of the negative may be reversed by a chemical process or it may be transferred to a unmodulated photon stream by absorption-modulation to expose a second photosensitive surface. The conversion from radiation energy to electrons to atoms and the development to grains is repeated in this surface, resulting in a positive image.

Because of the random distribution of "particles" in these conversion or transfer processes, the density representing a particular

* The field produced by the radiation (photon stream) from an incoherent source is essentially noise-free.

"signal" amplitude is subject to statistical fluctuations termed "noise." Signal amplitude and noise level can be determined by a particle count in a representative sampling area $\bar{a}$ or, more accurately, by a count of independent "statistical units." Near the input of a system a statistical unit may be a single electron or atom. In later stages the unit is amplified to become a large aggregate still representing one independent statistical unit. The number of output signal units in a given sampling area $\bar{a}$, therefore, cannot exceed the number of input units; that is, the statistical unit gain cannot exceed unity. A large number of independent units of different size, however, are added to the signal

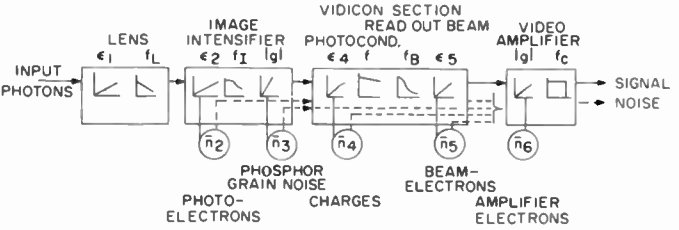

Fig. 1—Transfer stages and noise sources of an intensifier vidicon camera.

units in various stages of the process by the particle structures or granularity of new surfaces, or by modulation carriers that increase the deviations and the number of particles that must be counted in an evaluation of system granularity or noise. To avoid counting errors it is expedient to determine the independent signal-to-noise ratios by separate counts whenever a new independent particle structure or flow is introduced into the system, i.e., at all points of noise insertion. This approach may be illustrated by the block diagram of a television camera shown in Figure 1. The imaging stages are shown as boxes enclosing the density-transfer curve and the frequency-transfer curve over which signal and noise from preceding stages are transferred. The granularities are shown as noise generators ($\bar{n}_n$) feeding into the stage output. It should be noted that photon streams are noise-free carriers,* although they may be modulated by noise from another source, as in stage 3. The noise-transfer paths are shown by separate lines. It is seen that the frequency spectrum of the photoelectron noise, for ex-

* The existence of a noisy photon "particle" stream or a "coherent" electron emission from a photoemitter, that is, a one-to-one correspondence of electrons and exciting photons, has yet to be demonstrated. These assumptions are generally made to explain that photon noise is not observed in the current of a photoemitter.

ample, may be drastically reduced by the combined frequency response of the system; however, noise injected near the system output retains a much wider frequency spectrum. Therefore, individual signal-to-noise ratios are computed for the various noise sources in a given sampling area $\bar{a}$ and transferred separately to the system output, where they are combined to give the signal-to-noise ratio of the system.

The resolving power is generally specified as the fundamental spatial frequency of the smallest 3-bar test object that can be resolved. It has been determined[1] that detection of a pair of these standard test objects in a single-image "frame" requires a threshold signal-to-noise ratio $K = 3.6$ for the area of one bar, whereas detection in a continuous "live" image requires a threshold value $K = 2$. Essentially, the solution for resolving power involves the calculation of the area $\bar{a}$ of the test object bar reproduced with a specified signal-to-noise ratio. It will be shown that resolving power can be computed, in general, from particle densities without recourse to specific photographic or electronic terminology. The particle densities can be converted by simple relations into the practical units used in photography or television engineering, i.e., into optical, charge, or current densities. Sampling areas, spatial frequencies, or pass bands can be translated into electrical frequency channels. The unit length used throughout this paper is defined as one millimeter, which is the standard unit for spatial frequencies. The corresponding unit area of one square millimeter is used to specify particle, current, or charge densities, and unit signal-to-noise ratios, which are indicated by the subscript (1).

II—Theory

1. Generalized Expressions for Signals and Noise

The absolute signal at any location within an image area A may be defined as a count $\bar{n}_s$ of signal units or particles within an equivalent area $\bar{a}$; that is,

$$\bar{n}_s = \bar{n}_{s(1)}\,\bar{a}, \tag{1}$$

where $\bar{n}_{s(1)}$ is the signal density per unit area caused by a photon exposure, and $\bar{a}$ is the equivalent sampling area. The bar signs indicate that the values are mean values of many samples observed on repetitive image frames (television or motion picture), or, when only one image is available, taken from an area of uniform density.

The rms deviation or rms noise for a random particle source is

given by

$$\bar{n}_n^{1/2} = (\bar{n}_{n(1)}\bar{a})^{1/2}, \tag{2}$$

where $\bar{n}_{n(1)}$ is the particle density producing noise.

Carrier Modulation Factors

When the signal alone constitutes the particle density producing noise, i.e., when $\bar{n}_{n(1)} = \bar{n}_{s(1)}$, removal of the signal results in a zero noise level. This condition occurs in optical transfer stages and may also apply to photoemitters or other bombardment-induced emitters and to transfer processes for high-level signals. It does not apply when excess particle densities $\bar{n}_{d(1)}$ of applicable magnitude are injected by a signal carrier. The mean particle density $\bar{n}_{n(1)}$, which determines the noise of a particle-type carrier, is thus generally

$$\bar{n}_{n(1)} = \bar{n}_{s(1)} + \bar{n}_{d(1)}.$$

The ratio of the signal density to the total particle density $\bar{n}_{n(1)}$ in such a transfer stage is called the carrier modulation factor, m_c;

$$m_c = \bar{n}_{s(1)}\ (\bar{n}_{s(1)} + \bar{n}_{d(1)})^{-1}. \tag{3}$$

The excess particle density in a photographic system is called the "fog" density. "Fog" densities of appreciable magnitude may be injected into a television system by the dark current of photoconductors and of the readout beam. In general, every independent carrier or particle stream in a system is a source of noise and has a modulation factor m_c. *The absolute signal-to-noise ratio in a unit area* at a noise source is, therefore,

$$\begin{aligned} |R|_{(1)} &= \bar{n}_{s(1)}\ (\bar{n}_{s(1)}/m_c)^{-1/2} \\ &= (\bar{n}_{s(1)}\ m_c)^{1/2} \end{aligned} \tag{4}$$

The condition $n_{s(1)} = n_{n(1)}$ is the special case where $m_c = 1.0$.

When the signal is transferred by a radiation carrier wave (light) as in photographic processes, image intensifiers, or picture tubes, the optical photon carrier itself is considered noise-free. The optical carrier from a phosphor is generated by electron excitation and noise modulated by the particle structure of the phosphor. The carrier

modulation factor has the value

$$m_{c(\text{phos})} = 1, \tag{3a}$$

because signal and noise disappear upon removal of the excitation.

The signal-to-noise ratio of a phosphor surface is best determined by measurement as for photographic grain structures. The phosphor is excited to a high output by a uniform electron excitation. The surface is scanned at a relatively slow speed (to minimize electron noise) with a microphotometer aperture. The measured d-c signal-to-rms-noise ratio $|R|_m$ is converted to the absolute signal-to-noise ratio in a unit area as follows:

$$|R|_{(1)\text{phos}} = |R|_m \bar{a}_m^{-1/2}, \tag{4a}$$

where $\bar{a}_m$ = area of microphotometer aperture in mm^2. The value $|R|_{(1)\text{phos}}$ is a constant. The phosphor noise deviations are invariable with respect to the image coordinates and can thus be recorded and canceled, at least in theory.

A difference signal may be defined as the difference in intensity units or particle counts taken with the same sampling area in two density levels:

$$\Delta \bar{n}_{s(1)} = \bar{n}_{s(1)a} - \bar{n}_{s(1)b}. \tag{5}$$

A difference signal is, for example, the peak value of an (equivalent) rectangular impulse of area $\bar{a}$ rising above or falling below a reference (background) level, or it may be the equivalent peak-to-peak value of a repetitive impulse series, i.e., a square-wave modulation superimposed on a mean level (as in resolving-power test charts). The difference signal, mean signal, and modulation factor (m) of a square-wave signal are related by the following equation:

$$\Delta \bar{n}_{s(1)} = 2m\bar{n}_{s(1)}, \tag{6}$$

where $\bar{n}_{s(1)} = 0.5\ (\bar{n}_{(1)a} + \bar{n}_{(1)b})$ = mean level count and $m = 0.5\ (n_{(1)a} - \bar{n}_{(1)b})/\bar{n}_{s(1)}$ = modulation factor. The modulation factor m_o of the optical test signal (in a bar test pattern) is related to the contrast ratio C by

$$C = (m_o + 1)/(1 - m_o),$$

or

$$m_o = (C - 1)/(C + 1). \tag{6a}$$

2. *Calculation of Signal-to-Noise Ratios in Resolving-Power Test Objects*

The intensity function of standard resolving-power test objects (see Figure 2) in the direction across the bars is essentially a square-wave modulation of a mean level. The signal of interest is the differ-

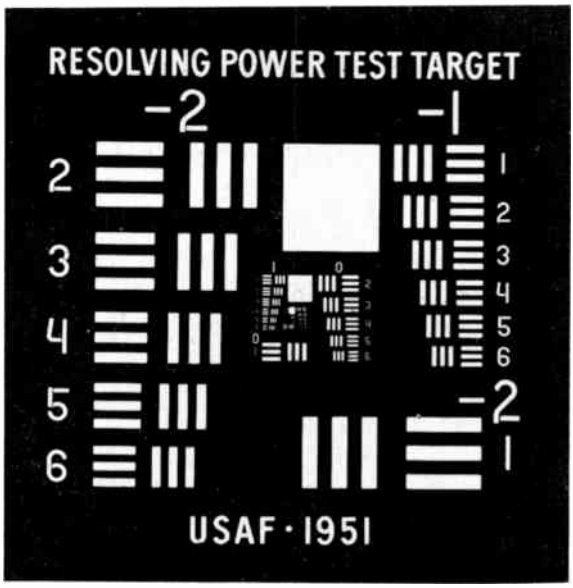

Fig. 2—Resolving power test object.

ence signal, which is given by

$$(\Delta I/\bar{I})_o = \Delta \bar{n}_{s(1)}/\bar{n}_{s(1)} = 2\, m_o. \tag{7}$$

The random deviation in intensity, granularity, or noise in the signal is specified by the absolute signal-to-noise ratio, which may be computed from Equations (4) and (4a).

Hence the *difference signal-to-noise ratio* at the point of noise insertion (in a stage i) is defined as follows:

$$(R\,\Delta)_i = |R|_{(1)i}\bar{a}_i^{1/2}\,(\Delta I/\bar{I})_i \tag{8}$$

where a_i is the noise equivalent sampling area and $(\Delta I/\bar{I})_i$ is the difference signal in stage i. When transferred through a system, the object bar areas a_o and their relative intensities are changed progres-

sively by convolution with the spread functions of the system stages. The bars of the standard test object have a width $W_o = 1/N$ mm and a length $l_o = 5W = 5/N$, where $N = 2f$ = television line-number/mm. Their area is therefore $a_o = 5/N^2$. The period or line number of the bars remains unchanged, so that $W_i = W_o$ throughout the system. The nonperiodic length l_i of the image, however, is increased by a spread factor to $l_i = S_i l_o$. *The spread factor* in any one stage (i) can be computed as follows:

$$S_i = l_i / l_o = [1 + \{0.2N/N_{e(i)}\}^2]^{1/2}, \tag{9}$$

where $N_{e(i)}$ is the equivalent pass band* of the system preceding and including stage (i) between the limits zero and N. The image area of the bars is, therefore, $\bar{a}_i = 5S_i/N^2$.

The amplitude of the difference signal is reduced in the periodic W direction by the mean square-wave response factor $r\bar{\Delta}_i$. (For small amplitudes this factor can be replaced by the sine-wave component, i.e., by $r\bar{\Delta}_i = 0.81\,\bar{r}_i$.) The amplitude is reduced further by the reciprocal spread factor $1/S_i$ in the l direction. It follows that the difference signal in stage (i) has the value $(\Delta I/\bar{I})_i = (\Delta I/\bar{I})_o r\bar{\Delta}_i/S_i$ and, from Equation (7), $(\Delta I/\bar{I})_i = 2m_o r\bar{\Delta}_i/S_i$.

With these substitutions, Equation (8) can be rewritten

$$(R\,\Delta)_i = [|R'|_{(1)i}(5S_i/N^2)^{1/2}]\,[2m_o r\bar{\Delta}_i/S_i]. \tag{8a}$$

After transfer to the output of the system, the difference signal from any given point in the system has the value,

$$(\Delta I/\bar{I})_{\text{out}} = 2m_o r\bar{\Delta}_{\text{syst}}/S_{\text{syst}}$$

Excess particle densities (noise), however, are injected at different points in the system, and the integration is larger for noise injected near the input and decreases for noise injected closer to the system output. The change of the rms noise value is determined by the two-dimensional noise pass band of the system elements *following* the noise source. *The equivalent pass bands at a noise source* (i.e., at a given stage (i)) are the reciprocal values of the dimensions of the noise equivalent sampling area $\bar{a}_i$ (see Appendix),

$$N_{e(l)_i} = 1/l_i, \text{ and } N_{e(w)_i} = 1/W = N$$

* See also Appendix, Equations (57) to (59).

The equivalent noise pass band $N_{e(l)_i}$ is changed at the system output to $N_{e(l)\text{syst}} = 1/l_{\text{syst}}$. The corresponding one-dimensional *noise bandwidth ratio* is, therefore, $\rho_{(l)_{\text{k-out}}} = N_{e(l)\text{syst}}/N_{e(l)_i} = l_i/l_{\text{syst}}$.

If the lengths are replaced by the spread factors $S_i = l_i/l_o$ and $S_{\text{syst}} = l_{\text{syst}}/l_o$, the noise bandwidth ratio can be expressed by the spread factor ratio;

$$\rho_{(l)_{k\text{-out}}} = S_i/S_{\text{syst}}. \tag{10a}$$

The equivalent noise pass band $N_{e(w)_i} = N$ is changed by the sine-wave response function $(\bar{r}_k \cdot \bar{r}_l \ldots \bar{r}_{\text{out}})$ (N) of the system elements $(k\text{-out})$ following the noise source, without change of the dimension W, to the following function:

$$N_{e(w)_{k\text{-out}}} = \int_0^N (\bar{r}_k \cdot \bar{r}_l \ldots \bar{r}_{\text{out}})^2 dN$$

The corresponding *noise-bandwidth* ratio is therefore given by

$$\rho_{(w)_{k\text{-out}}} = N_{e(w)_{k\text{-out}}}/N \tag{10b}$$

Thus, the signal-to-noise ratio $(R\,\Delta)_{i\text{-out}}$ at the system output is obtained by replacing the signal ratio $(\Delta I/\bar{I})_i$ in Equation 8 by the expressions given for $(\Delta I/\bar{I})_{\text{out}}$, and dividing by the square root of the two one-dimensional bandwidth factors:

$$\begin{aligned}(R\,\Delta)_{i\text{-out}} &= |R|_{(1)i}\,[5S_{\text{syst}}/(N^2\rho_{(w)_{k\text{-out}}})]^{1/2}\,[2m_o r\bar{\Delta}_{\text{syst}}/S_{\text{syst}}] \\ &= |R|_{(1)i}\,4.48\,m_o r\bar{\Delta}_{\text{syst}}/[(S_{\text{syst}}\rho_{(w)_{k\text{-out}}})^{1/2}N].\end{aligned}$$

Thus far it has been assumed that the amplitude transfer is linear. Because amplitude transfer generally is not linear, absolute signals must be multiplied by the following transfer factor, $|g|_i = \bar{n}_{(1)\text{out}}/\bar{n}_{(1)\text{in}}$, which is the ratio of the output particle count to the input particle count. However, modulating signals, such as a difference signal or noise, are multiplied by the gradient of the transfer curve, defined by $g_i = d\bar{n}_{(1)\text{out}}/d\bar{n}_{(1)\text{in}}$. The peak-to-peak modulation factor $2m_o$ is the ratio of a modulating signal to the absolute signal level that has been transferred from the input to stage (i). It must, therefore, be multiplied by the transfer ratio $(g/|g|)_{o\text{-}i} = \gamma_{o\text{-}i}$ of the stages *preceding* the noise insertion point. Beyond this point, the absolute signal is no

longer of interest because a difference signal-to-noise ratio ($R\,\Delta$) is a *modulation ratio* for which the amplitude transfer ratio is unity in all succeeding stages.

Hence, the complete equation for a signal-to-noise ratio originating in a stage (i) after transfer to the system output is given by

$$(R\Delta)_{i\text{-out}} = |R|_{(1)i}\gamma_{o\text{-}i}\, 4.48\, m_o r\bar{\Delta}_{\text{syst}}/[(S_{\text{syst}}\rho_{(w)_{k\text{-out}}})^{1/2}N], \quad (11)$$

where $|R|_{(1)i}$ is the absolute signal-to-noise ratio at source (i) in $\bar{a} = 1\ \text{mm}^2$ (Equation 4),

$\gamma_{o\text{-}i}$ is the total system gamma at operating points preceding the noise source,

$\gamma = d \log n_{\text{out}}/d \log n_{\text{in}} = g/|g|$

$r\bar{\Delta}_{\text{syst}}$ is the square wave response factor of entire system at N

m_o = modulation factor of test object (Equation (6))

S_{syst} is the spread factor of the system in the bar length direction

$$S_{\text{syst}} = [1 + (0.2N/N_{e(l)\text{out}})^2]^{1/2}$$

$\rho_{(w)_{k\text{-out}}}$ = bandwidth factor (Equation (10b))

3. *The Difference Signal-to-Noise $(R\bar{\Delta})_{syst}$ of a System Containing Several Noise Sources*

The signal-to-noise ratio at the output of a system such as that shown in Figure 1 can be computed by first combining the products $(|R|_{(1)i}\gamma_{o\text{-}i})/\rho_{(w)}^{1/2}$, depending on the location of the noise source, and subsequently multiplying their combined value by the common factors. The mean-squared noise from the various stages is combined by adding the squared reciprocal products as follows:

$$|R|_{(1)(\text{syst})}{}^{-1} = (P_2 + P_3 + \ldots + P_{\text{out}})^{1/2} \quad (12a)$$

where

$$P_n = \rho_{w(n+1)\to\text{out}}/(|R|_{(1)n}\gamma_{1\to\text{out}})^2$$

The product P_n for a particle-type carrier (stages $n = 2, 4, 5, 6$, in Figure 1) can be converted with Equation (4) to the following expression:

$$P_n = \rho_{w(n+1)\to\text{out}}/(\bar{n}_{s(1)n}m_{c(n)}\gamma^2{}_{1\to n}) \quad (12b)$$

where $m_{c(n)}$ is computed from Equation (3).

For stages having a noise-free carrier modulated by another noise source, such as stage (3) in Figure 1, the product P_n is computed with the value $|R|_{(1)n}$ | for stage 3, $|R|_{(1)n} = |R|_{(1)\text{phos.}}|$. The difference signal-to-noise ratio of the system is computed according to Equation (11), where

$$(R\Delta)_{\text{syst}} = |R|_{(1)\text{syst}}\, 4.48\, m_o r\bar{\Delta}_{\text{syst}}/(S_{\text{syst}}{}^{1/2}N) \tag{13}$$

Equation (13) can be solved for the test-object modulation (m_o) required for a specified resolving power (f_r) by letting $(R\Delta)_{\text{syst}}$ equal the threshold value K, as follows:

$$m_o = 0.448K\, f_r S_{\text{syst}}{}^{1/2}/(r\bar{\Delta}_{\text{syst}}|R|_{(1)\text{syst}}) \tag{14}$$

where $f_r = N/2 =$ resolving power in cycles/mm,

$K = 3.6$ for a single image,

$K = 2$ for continuous observation of a live image,

$S_{\text{syst}} =$ spread factor (Equation (11) for $N = 2f_r$, $N_{e(\text{syst})}$ computed for the upper limit $f_r = N/2$),

$r\bar{\Delta}_{\text{syst}} =$ square-wave response factor of system* at f_r,

$|R|_{(1)\text{syst}} =$ value computed with Equation (12).

4. *Optimum Filtering and Aperture Correction*

In a normal low-pass frequency spectrum, to maximize the signal-to-noise ratio, the spatial frequency band or corresponding video pass band of the system should not exceed the resolving-power frequency (f_r). Furthermore, optimum filtering requires that the viewing distance to the reproduced image, i.e., the magnification to the retina of the eye, be adjusted to utilize best the frequency selectivity of the visual system.[1] The use of a fixed optimum filter for a given test object is not suitable because it would destroy the correlation with other signals in the image. There are, however, fixed filter processes that can improve the resolving power of the system without destroying correlation in the image. These processes are known as aperture cor-

*Computed from first three terms of the Fourier Series;

$$r\bar{\Delta}_{\text{syst}} = \frac{8}{\pi^2}\left(\bar{r}_f + \frac{1}{9}\bar{r}_{3f} + \frac{1}{25}\bar{r}_{5f} + \dots\right).$$

rection in television, masking in photography, and image enhancement or optical processing in general. These processes provide a gradual increase of the high-frequency signal response, relative to the low-frequency response of the system, that partially or fully compensates for the decreasing frequency-response functions of the system elements.[2] A gain in signal-to-noise ratio and resolving power is realized

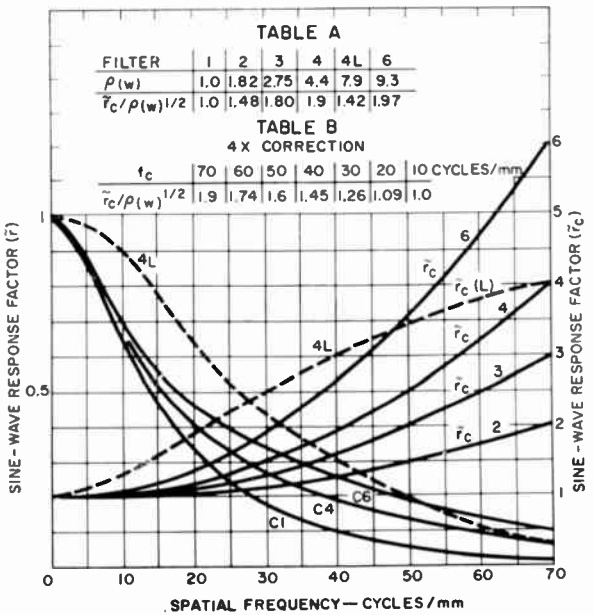

Fig. 3—Aperture correction function $r_c(f)$.

when the rms noise, i.e., the bandwidth integrals, increases more slowly than the high-frequency signal amplitude (response factor $\bar{r}_{syst}$). This effect may be achieved by a one-dimensional correction in the scanning direction and can be accomplished readily in television systems by simple circuits. The effects of such a correction can be assessed, in principle, as follows.

Figure 3 shows the sine-wave response factor ($\bar{r}_c$) as a function of spatial frequency (f) for a typical electrical correction circuits as well as the corrected vidicon-camera response function (C_1, C_4, C_6) for a bandwidth of 70 cycles/mm. Neglecting other than the scanning-beam noise source preceding the correction circuit, the increase in the signal-to-noise ratio ($R\Delta$) is given by the ratio $\bar{r}_c/\rho_{(w)}^{1/2}$, which is tabulated in Table A of Figure 3.

Table A shows that little is gained by signal corrections larger than 3:1. It is further apparent that a concave slope of the correction function (and a later start) provides a higher gain in the high-frequency signal-to-noise ratio than a correcting function such as $4L$. This function will provide a sharper image because it substantially increases the equivalent pass band of the camera, whereas optimum filters for maximum resolving power must discriminate against a larger low-frequency range. Table A shows further that a moderate aperture correction (4:1) improves the signal-to-noise ratio ($R\Delta$) by a factor of 1.9, which reduces the test-object modulation required for $f_r = 70$ cycles/mm. The ratios $\bar{r}_c/\rho_{(w)}{}^{1/2}$ for a 4× aperature correction at $f = 70$ cycles/mm are given in Table B of Figure 3 as a function of frequency. It is evident that aperture correction substantially increases the contrast and visibility, whereas the increase in resolving power is relatively small.

The signal-to-noise ratios and resolving-power functions of systems containing one-dimensional or two-dimensional aperture correction processes can be computed from Equations (12) and (14) by including the sine-wave response-function $r_c(f)$ and/or spread factor (S) of the correction process in the system response. The correction process may be electrical, optical, or photographic. When the correction is two-dimensional and equal in both directions, the increase of the test-bar signal [by the factor S/S_c] outweighs the increase in rms noise [factor $(S/S_c)^{1/2}$]. The resolving power is increased only slightly beyond the value obtained by a one-dimensional correction, but it is improved for both horizontal and vertical test object bars.

These results point out the difference in optimizing a system for high resolving power and not for high sharpness ("acutance", high $N_{c(\mathrm{syst})}$).

III. Characteristics of Television Cameras

The resolving power of the storage surface in television cameras is basically independent of area. However, the observable resolving power may be a function of area because it depends on the parameters of the camera, that is, the optics used for exposure, the electron optics required for signal readout, and the signal development process, which are generally functions of area (X, Y) and time. The development of a signal, for example, requires a certain time for each square millimeter of the storage surface. Thus, the sequential signal development in a television camera requires a read-out time proportional to the number of square millimeters in a given storage surface.

The time required for reading out a unit surface area (1 mm^2) is a

function of the unit capacitance, the charge potential, and the V/i characteristics of the reading beam. To clarify the dependence of sensitivity, conversion efficiency, and resolution on the time-to-capacitance ratio t/C, and to avoid misinterpretation of the resolving-power functions computed subsequently for specific operating modes, a discussion of the signal read-out process is appropriate.

1. Characteristics of Charge Storage Surfaces

The storage surface of a television camera tube is charged and discharged by essentially constant currents. The charge $q_{(1)}$ in a unit area of storage surface is given by

$$q_{(1)} = C_{(1)} V = \bar{\imath}_{s(1)} t, \tag{15a}$$

and the electron density is given by

$$n_{(1)} = q_{(1)}/q_e, \tag{15b}$$

where

$q_{(1)}$ = charge/mm^2 (coulombs),

$C_{(1)}$ = capacitance/mm^2 (farads),

V = potential (volts),

$\bar{\imath}_{s(1)}$ = mean current density (per mm^2) during time t

$q_e = 1.6 \times 10^{-19}$ = charge of one electron.

The electron or charge density in the storage surface is built up by a current (i) during a short exposure time $t = t_e$. This charge potential can be removed or read out by an identical current when the read-out time t_f equals t_e, or by smaller or larger currents when t_f is made correspondingly larger or smaller than t_e.

The maximum charge potentional that can be read out by a low-velocity electron beam is generally limited to $V_{max} = 6$ volts, because of electron reflection and secondary emission at the storage surface. (This value may be somewhat higher for very porous surfaces and lower for smooth surfaces, and it decreases for high field gradients.) For high-definition signals, the value of the read-out current is limited to less than 200 nA because of the increasing spread of electron velocities with current density. Therefore, in high-definition storage surfaces, which must have a high unit capacitance and a large surface area, the minimum read-out time may be in the order of seconds.

The unit capacitance $C_{(1)}$ required for a storage surface having the resolving power of high-resolution aerial film (470 cycles/mm for Kodak type 4404) can be determined from the noise equivalent particle density of this emulsion, which has the value $\bar{n}_{s(1)f} = 1.0 \times 10^7$ electrons per mm^2 at maximum resolving power.[1] Because of the added beam-current noise in the television read-out, the equivalent electron density

Table I—Approximate Characteristics and Minimum Readout Times of Charge Storage Surfaces ($V = V_{max}$, 90% Discharge)

Type of Surface	Equiv. Thickness (microns)	$C_{(1)}$ (pF)	$n_{s(1)}$/volt	Charge Potential V_{max}	Readout Time* t_f (Sec) (A=1 cm^2)	(A=25 cm^2)
4404 Film	2	8	5×10^7	4.25	0.0345	0.86
ASOS photo-conductor	1	160	1×10^9	6	0.385	9.60
		80	5×10^8	6	0.192	4.8
Porous photo-conductor (Vidicon)	4	10	6.25×10^7	6	0.024	0.60
Plumbicon	14.3	3.7	2.3×10^7	6	0.0089	Insuff. storage
S.E.C. (Westinghouse)	12	0.8	5×10^6	6	0.0019	0.0475
Glass Target Image Orthicon	25	0.35	2.2×10^6	4	0.00158	0.0395

* $t/C = 24$ for $V_{max} = 6$ V
$t/C = 45$ for $V_{max} = 4$ V

must be approximately 5 times this value, that is, $\bar{n}_{s(1)f} \simeq 5 \times 10^7$ electrons/mm^2. This value represents the equivalent charge density of the 4404 emulsion obtained with a 1-volt potential, because this emulsion has a sufficient number of grains for 4.25 times this density, or an equivalent electrical potential of 4.25 volts. The equivalent unit capacitance of this film is $C_{(1)} = 8 \times 10^{-12}$ farad.

The noise equivalent sampling area of the 4404 emulsion has a diameter of 2 microns. Because the equivalent potential spread of a point charge on an electrical storage surface is approximately equal to its thickness d, an electrical storage surface having a thickness of 2 microns has the same sampling area as the 4404 emulsion. (The beam senses the potential and not the charge itself.)

Table I compares the constants of various charge storage surfaces with these reference values.

The small thickness (d) of ASOS (antimony sulfide–antimony oxisulfide) and porous photoconductors used in vidicons indicates equiva-

lent sampling areas comparable to or smaller than the 4404 emulsion and higher resolving powers (for the surface itself) because the electron densities (n_{st}, V_{max}) exceed that of the highest-definition aerial film.

The *minimum* read-out time (t_f) computed for a 90% discharge (see following section) is given for a 1 cm² area (one-inch vidicons and similar television camera tubes) and for the 25-cm² area of developmental high-definition vidicons.

The last three surfaces listed in Table I have small capacitances and are thus particularly suited for live pickup in standard television systems because an adequate discharge can be obtained in 1/30 second. Their resolving power is lower, however, because of the greater thickness and lower electron density.

2. *The V/i Characteristics of Low-Velocity Electron Beams*

The current (i) landing on a storage surface is a function of the potential (V_{st}) of the storage surface relative to the cathode of the electron gun and the electron absorption factor (α) of the surface. The beam current (I_b) passing through the defining aperture of the gun is adjustable by the control electrode (g_1). The parameter I_b' in Figure 4(a) is the current approaching the collector (after having passed through a field mesh). When V_{st} is several volts positive, and $\alpha = 1$, all electrons can land on the collector, i.e., the beam is saturated. When V_{st} is reduced, the collected current (i) decreases slowly at first (as in beam power tubes), until the saturation knee is reached, below which it decreases exponentially. The absorption factor α of the collector electrode used in these measurements is a constant* judging from the fact that current saturation is obtained. A "perfect" electron gun with a cathode temperature of 1100°K would have a straight-line characteristic (on semilog paper) as indicated in Figure 4a, and its saturation currents would be horizontal constant-current lines breaking away from the steep unsaturated current curve at saturation points $i = I_b'$. The electron absorption factor (α) of practical storage surfaces is generally smaller than unity because of electron reflection that occurs at voltages smaller than 10 volts and has a maximum near 6 volts. The effect of electron reflection is demonstrated by the V/i characteristics shown in Figure 4(b). The collector current never reaches the saturation value $I_s = I_b'$. The characteristics were measured on a special 4½-inch vidicon tube having an electron multiplier, a field mesh, and a split target; one-half being

* It is assumed that $\alpha = 1$

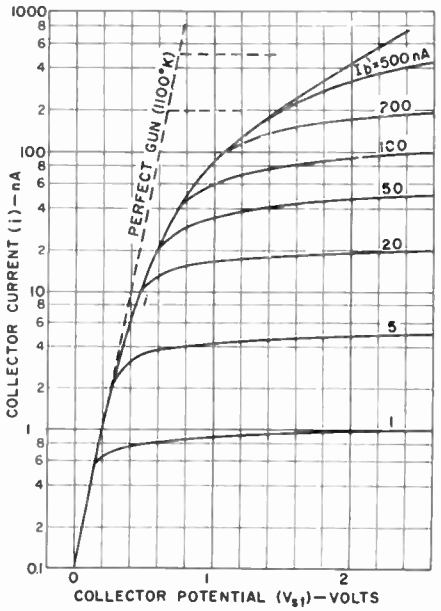

Fig. 4a—V/i characteristics of electron beams for a constant electron absorption factor α and a 2-mil gun aperture.

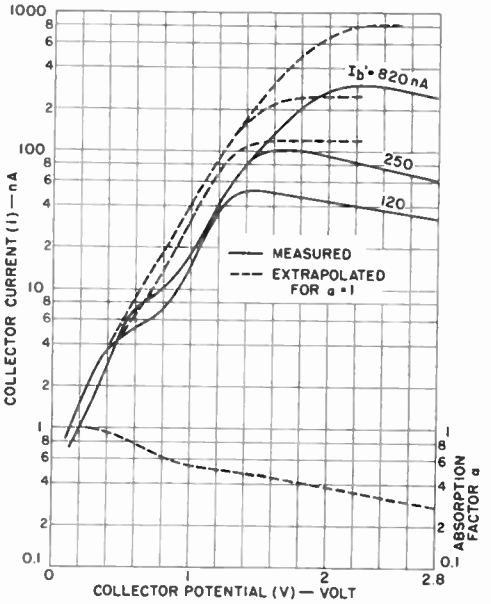

Fig. 4b—V/i characteristics of electron beams for a variable electron absorption factor $\alpha(V_{s1})$ and a 1.7-mil gun aperture and a 750-wire/inch field mesh.

an ASOS surface and the other half a solid collector. The beam current I_b' approaching the storage surface or the collector (after passing the mesh) has the value $I_b' = i/m_b$, where i is the current measured in the collector or storage surface leads, and $m_b = (I_b' - \Delta I)/I_b'$ is the modulation of the return beam measured in the output circuit of the multiplier. The total beam current I_b leaving the de-

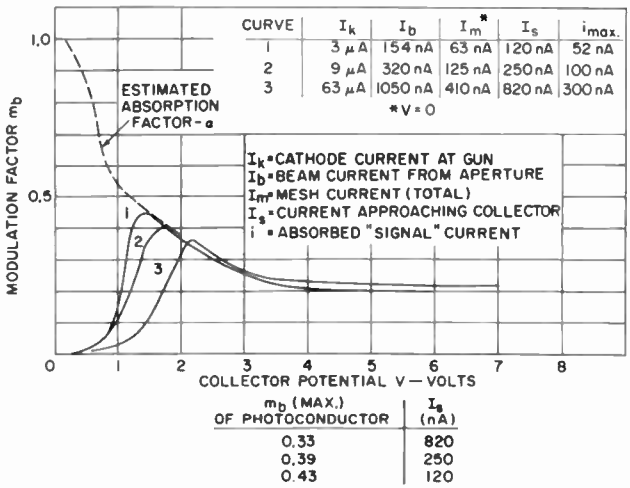

Fig. 4c—Measured beam modulation factors as functions of collector potential.

fining aperture of the electron gun is obtained from the relation

$$I_b = I_b'/\tau_m,$$

where τ_m is the mesh transmission factor. The V/i characteristics shown in Figure 4(b) were measured on the solid collector permitting a direct measurement of collector potential. The absorption factor α of the collector (a "TIC" coating) happened to be nearly the same as that of the particular ASOS surface. The broken-line curves in Figure 4(b) are the V/i characteristics estimated for zero electron reflection, i.e., an electron absorption factor $\alpha = 1$. The estimated absorption factor as a function of collector potential below the V/i characteristics is also shown in Figure 4(b).

Figure 4(c) shows the measured beam modulation factors as functions of collector potential. The potentials V in Figures 4a and 4b are relative values with respect to an arbitrary cutoff potential V_o set at a current of 0.1 nA. (The actual potentials are negative retarding potentials in the exponential region.)

age surface after having passed the field mesh. This current may be lower than the current leaving the electron gun by a factor of 1.5 to 2 because of current absorption by a field mesh between gun and storage surface.

It is evident from Figure 5 that a 100% discharge by a low-velocity electron beam is theoretically impossible. The "perfect" electron gun would give a slightly lower residual potential ($V_r = 0.33$ volt or 9% for the example) and nearly the same beam modulation ($m_b = 0.55$).

The *total current* (i) read out by the reading beam is given, in general, by

$$\begin{aligned} i &= \Delta V/(t_f/C) \\ &= (V_{st} - V_r)/(t_f/C). \end{aligned} \tag{19a}$$

The potential of the *storage surface* at the instant before read-out* is as follows:

$$V_{st} = V_s + V_r + V_o,$$

where V_s = signal potential caused by the current i_s of the exposure, V_r = potential carried over from a preceding readout or a preceding erase cycle, and V_o = potential sum of excess charges plus a control voltage† $V_c(t)$.

The *signal current* (i_s) is the difference

$$i_s = i - i_o,$$

where

$$i_o = (V_o - V_{r_o})/(t_f/C) \tag{19b}$$

is the "black level" current read out without exposure ($V_s = 0$). (For the example, $i_s = 3.5/33.3 = 0.105\ \mu$A, assuming $V_o = 0$.) The conversion efficiency (η_c) has the value

$$\eta_c = \Delta V/V_s = (\bar{i} - \bar{i}_o)\, t_f/(CV_s) \tag{20}$$

(For the example, $\eta_c = 3.5/4 = 0.875$.) The *transfer efficiency* of the read-out beam (stage 5), working into an electron multiplier, has the value

$$\epsilon_5 = \eta_c \tau_m, \tag{21}$$

where τ_m = transmission factor of the field mesh.

* With respect to beam cutoff.

† Use of an external control voltage requires an erase time, otherwise $V_c(t) = 0$

4. *Demodulation of Residual Charges*

The carry-over of residual charges into successive images caused by an incomplete discharge (capacitive lag) results in a cross modulation of image signals. A small residual potential (V_r) can be obtained by a long read-out time or by a decrease in the storage capacitance (C) to increase the value t/C. Low-capacitance image orthicons, for example, having a total capacitance $C = 100$ pF, have a discharge time ratio $t_f/C = 333$ for $t_f = 1/30$ second. A reading beam $I_b' = 0.05\ \mu$A can then discharge a storage potential $V_{st} = 2.5$ volts to a residual potential $V_r = 0.075$ volt (3%) because $t_2/C = 283$. The beam-modulation factor, however, decreases to $m_b = 0.145$, resulting in a higher noise level.

Because it is not possible to remove the relatively large residual charge in storage surfaces of higher capacitance (without destroying their storage), a mechanism must be introduced to demodulate the residual charge. Demodulation will produce a constant value V_r (X, Y) at all points on a storage surface and thereby prevent a spatial cross modulation of independent charge images.

Demodulation can be accomplished by introducing a certain amount of lateral charge integration (lateral "leakage" in the PbO vidicon or high-temperature glass targets of image orthicons), which levels out stored charges in a certain time. Unless controllable, a lateral integration introduces a definite time limit for the read-out, because it reduces the image storage efficiency and degrades the sine-wave modulation transfer function of the storage surface as a function of time.

Residual charges can be further demodulated *by the addition of a uniform charge bias.* A controllable bias charge can be introduced by a uniform light exposure of the storage surface using an auxiliary light source, or by a uniform dark current applied to the storage surface. The most complete demodulation is obtained when an "erase" time can be inserted between image exposures. In this case a large demodulating bias charge (V_b) can be added to the residual charge by a bias light exposure which, after discharge in the erase time, reduces the residual a-c modulation to zero.

In the *continuous exposure read-out mode,* the additive bias charge (V_b) must be small to prevent a general demodulation of image signals. An optimum charge bias value is one that is approximately equal to the residual charge ($V_b \simeq V_r$), and should be located in the knee of the t/C function. The vidicon example yielded $V_r = 0.5$ volt for $V_{st} = 4$ volt, $I_b' = 0.2\ \mu$ A, and $t_f = 1/30$ second. With the added bias potential, $V_b = 0.5$ volt, the initial potential becomes $V_{st} = 4.5$ volts, resulting in $t_1/C = 22.5$, $t_2/C = 10.8$, and $V_r = 0.53$ volt. At zero exposure, the black

level potential has the value $V_b = 0.5$ volt. The discharge time begins at $t_2/C = 13.3$ and ends at $t_2/C = 33.3 + 13.3 = 46.6$ yielding $V_{rb} \simeq 0.28$ volts. The residual modulation amplitude is the difference between the residual potentials at maximum and minimum exposures:

$$\Delta V_r = V_r - V_{rb} = 0.53 - 0.28 = 0.25 \text{ volt.} \tag{22}$$

Thus the residual modulation has a maximum value $\Delta V_r/(V_{st} - V_r) = 0.063 = 6.3\%$, which is roughly one-half of the cross modulation obtained without a bias charge. The bias charge can be produced by the dark current of the porous photoconductor (controllable by adjusting the target voltage). The value i_d of the dark current is

$$i_d = (V_b - V_{rb})\, C/t_f. \tag{23}$$

(For the example, $i_d = (.05 - 0.28) \times .0001 \times 30 = 0.0066\ \mu$A.)

It is interesting that the combination of a "perfect" reading beam with a "perfect" storage surface (having zero dark current) has a higher cross modulation (9%) than the practical one-inch vidicon with dark current.

It follows that storage surfaces without dark current should be operated with appropriate bias lighting, which incidentally is introduced to some extent by light scattering in the optical system or haze in the external scene.

5. *Signal Transfer and Readout Gamma*

(a) Single Exposure-Erase Mode

The transfer of the stored signal charges into signal currents is determined by the beam current and the readout time ratio* t/C.

The charge read out is represented by the potential difference $(V_{st} - V_r)$, which may be computed for a set of potentials V_{st} on the storage surface as discussed in the preceding section. Figure 6 shows

* It is assumed that C is a homogeneous capacitance without dielectric lag. When the charge distribution within the thickness of the dielectric is not uniform, the total charge cannot be removed during a single pass of the scanning beam over an elemental capacitance, even though the surface charge may be completely removed. A surface charge may have built up again which can be removed in a second beam contact. A number of beam contacts will then provide a more complete discharge than a single contact, although the total time of the multiple contact may be the same as that of the single contact. As a consequence, the effective capacitance C of such storage surfaces appears to have a larger value for a single slow-scan read-out than for a multiple-frame fast-scan read-out of equal duration.

the transfer functions obtained for the time ratios $t/C = 2$, 10, and 20, assuming a beam current $I_b' = 200$ nA and zero dark current ($i_d = 0$).

The curves show that the signal voltage becomes constant for potentials higher than $V_{st} = 6.4$ volts for $t/C = 20$ because the residual potential V_r lies on a constant-current line. The saturation potential increases for longer read-out times and decreases for shorter readout times.

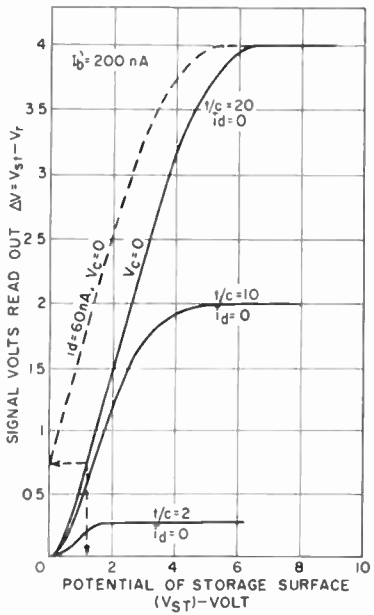

Fig. 6—The transfer function $\Delta V(V_{st})$ for several values t/C.

The effect of dark current $i_d = 60$ nA (for a 25-cm² surface) is shown in Figure 6 by the curve labeled "$i_d = 60$ nA, $V_c = 0$". The dark current adds the value $V_d = i_d\, t/C = 1.2$ volts. Thus, the entire curve $i_d = 0$, $V_c = 0$ is displaced as a function of t during the read-out time towards the end position $i_d = 60$ nA, $V_c = 0$ where the black-level potential has increased to 1.2 volts. The build-up of the dark current charge can be counteracted by the addition of a negative (sawtooth) control voltage $V_c\ (t)$ to the photoconductor voltage during the read-out time. This voltage stabilizes the function $i_d\ (V_{st}, t)$ when $V_c(t) = -V_d(t)$. The dark current charge is thus depressed below the read-out threshold. However, the dark current charge must be removed during a subsequent erase time.

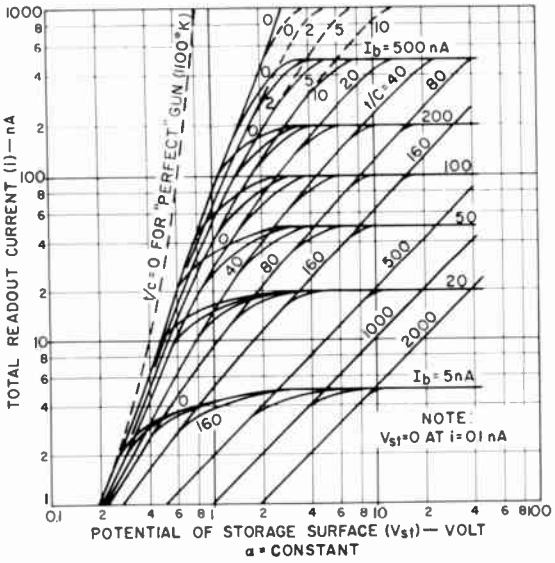

(a)

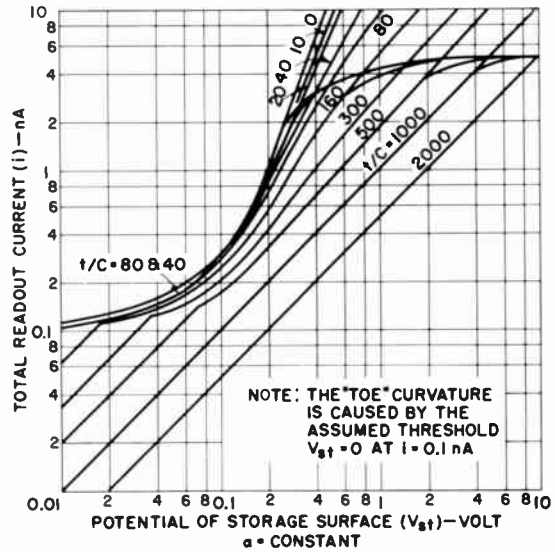

(b)

Fig. 7(a, b)—Current transfer function $\bar{i}(V_{st})$ of the reading beam from a 2-mil gun aperture and storage surfaces with constant α (see Figure 4a).

The exponential V/i characteristic of the unsaturated beam results in a nonlinear relation of signal and storage surface potential in single exposure–erase modes. This nonlinear relationship is shown more clearly when the potential difference $\Delta V = (V_{sl} - V_r)$ or the corresponding total read-out current $i = i_s + i_o$ (see Equation (19b)) is plotted in log-log coordinates as shown in Figures 7a and 7b.

The exponent, or gamma, of the current-transfer function increases to high values when the development time t/C is reduced. (The "toe"

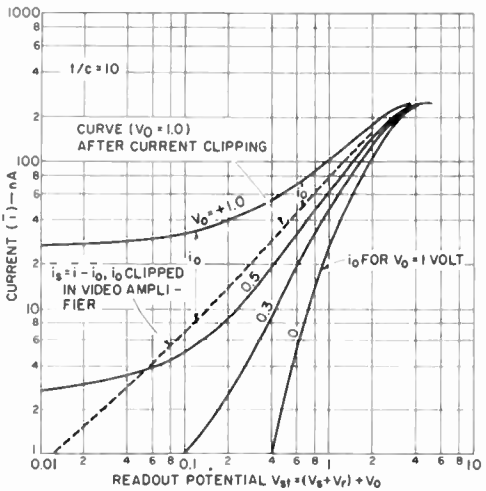

Fig. 8—Variation of readout gamma (γ_6) by bias potentials V_o and black-level clipper in video amplifier.

curvature at low potentials is introduced by the choice $V = 0$ at $i = 0.1$ nA). This behavior is contrary to the increase of gamma with development time in photographic emulsions.

The effective read-out gamma can be greater than two for fast read-out without a bias charge (negligible or compensated dark current and zero bias lighting). The gamma can be varied within wide limits by the addition or subtraction of a bias potential (V_o) by adjustment of the bias lighting and particularly the read-out threshold bias. The dark current charge built up during the read-out time can be compensated for by a sawtooth component in the control voltage $V_c(t)$.

Figure 8 shows the variation of the read-out gamma with bias potential V_o for $t/C = 10$. Apparently, the input signal latitude is increased by the addition of a bias voltage to the signal charges. It is evident that addition of an excessive bias value (for example, a large

dark current charge not depressed below the read-out threshold) results in signal compression in the low-light region. The "toe" curvature of the transfer functions can be reduced by current "clipping" in the video amplifier, as shown by the broken-line curve $\bar{i}_s = \bar{i} - \bar{i}_o$ in Figure 8. A read-out bias improves the conversion efficiency η_c when reading out very small potentials (see Section V-4).

(b) Continuous-Exposure Read-Out Mode without Erase Cycle

For low-capacitance storage surfaces, the signal transfer becomes linear as the value of t/C becomes larger. (See $t/C > 160$ in Figure 7.) It remains linear in continuous-exposure read-out cycles when t/C is decreased, because of the absence of an erase time. When the discharge is incomplete, the residual potential V_r builds up in successive scan cycles until the read-out current (i_s) equals the exposure current (i_e). At this point the *equilibrium potential* (V_e) of the storage surface equals the storage potential V_{st} in Figure 7 at any given signal current $i_s = i_e$. For $I_b' = 200$ nA, $i_s = 80$ nA, and $t/C = 2$, for example, the equilibrium potential is $V_e = 1.1$ volt. The potential swing, i.e., the signal amplitude in each frame time, has the value $\Delta V_e = i_e(t/C) = 0.08 \times 2 = 0.16$ volt. The signal-transfer function i_s (ΔV_e) is a linear function because equilibrium requires that $i_s = i_e$ for any value of current. *The read-out gamma is unity in the continuous exposure mode.* The equilibrium potential V_e of a storage surface is not a single value, but a function of the light intensity, i.e., of the exposure current distribution i_e (X, Y) in the stored image. The read-out efficiency is the ratio $\Delta V_e/V_e$, which is 15% for the example, whereas *the conversion efficiency* η_c is 100% *in the steady-state condition* because $i_s = i_e$.

The transient time required to build up the steady-state equilibrium charge is somewhat longer than the constant-current charging time required to reach equilibrium potential (V_e) because of the simultaneous discharge by the beam current. The mean discharge current $\bar{i}$ in the transient time t_t/C has values varying from $0.2i_e$ to $0.4i_e$, depending on the shape of the single-exposure transfer function.

When the signal current has the value $\bar{i}_s = 0.3i_e$, the transient time is given by

$$t_t/C = V_e/(0.7i_e) \tag{24}$$

For the above example, $V_e = 1.1$ volt and $i_e = 0.08\mu$A; $t_t/C = 19.7$ sec/μF. A build-up to 70% of the final signal current, i.e., to 0.7×80 nA, requires a storage surface potential V_{st} of approximately 0.92 volt (see curve $t/C = 2$ in Figure 7); thus the time t_t/C is 83% of the above value.

6. *The Self-"Sharpening" Effect of the Reading Beam*

The discharge action of an electron beam can be analyzed in detail by moving its line-spread function over a sharp potential step perpendicular to the scanning direction. The line-spread function of the beam is divided into sections of equal width that are considered as a sequence of independent beams effecting a progressive discharge. A $\cos^2$ line-spread function, for example, may be divided into six sections having fractional beam currents proportional to the areas 0.028, 0.167, 0.305, 0.305, 0.167, and 0.028, their sum equaling unity. The discharge by any

Table II—Computation of Effective Line Spread Function

n	$\Sigma \Delta t/C$	$V_{n-1} = 2$	ΔV	i (μA) ($t_f/C = 20$)	i (μA) ($t_f/C = 40$)	i (μA) ($t_f/C = 80$)
1	$0.028 \times 20 = 0.56$	$V_n = 1.90$	0.10	.030	.0225	.0262
2	$0.167 \times 20 = 3.34$ $\Sigma = 3.90$	1.45	0.45	.135	.128	.0762
3	$0.305 \times 20 = 6.10$ $\Sigma = 10.00$	0.84	0.61	.183	.081	.0202
4	$0.305 \times 20 = 6.10$ $\Sigma = 16.10$	0.60	0.24	.072	0.18	.006
5	$0.167 \times 20 = 3.34$ $\Sigma = 19.44$	0.55	0.05	.015	.009	.00075
6	$0.028 \times 20 = 0.56$ $\Sigma = 20.00$	0.54	0.01	.003	.00075	—
				$m_b = 0.364$	$m_b = 0.206$	$m_b = 0.115$

one of the n sections can be computed using $(\Delta t/C)_n = a_n\,(t/C)$, by varying the time instead of the current in the product $(i\,t/C)$, where a_n is the normalized area of the section. The residual potential V_r of the first section is the starting potential of the second section and so on. Thus, the potentials V_r are read on the t/C curve for the full beam current (Figure 5) at the points $\sum_{o}^{n} \Delta t/C$ as shown in Table II for an initial potential $V_{max} = 2$ volts, $I_b' = 0.2\ \mu$A, and $t/C = 20$.

The last three columns give the mean current in the six sections (six times the mean value in the total time t/C). The current distribution $i = f(x)$ of the signal current is obtained by drawing an appropriate amplitude curve through the mean values of the six sections as shown in Figure 9(a).

The area under the curve $i_s(x)$ is equal to the product of m_b and the area under the curve $i_b(x)$ of the beam approaching the storage

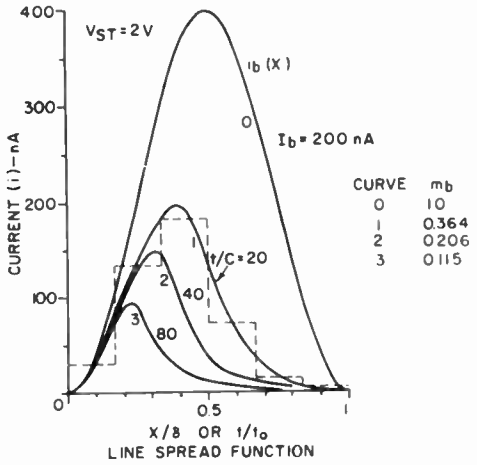

Fig. 9a—Effective line spread function of unsaturated reading beams as a function of the return beam modulation m_b, computed for the discharge functions (Figure 5).

surface, where m_b is the modulation factor computed with Equation (18). It is apparent that a low modulation factor (excess beam current) results in a completion of the discharge by a fraction of the total beam cross section. The front portion of the beam is 100% absorbed while the back portion is only partially absorbed. Thus, the beam is "self-sharpening".

The sine-wave response increases in inverse proportion to the width of the spread function. It has its lowest (normal) value at potentials near the saturation value (see Figure 6 or 7) where the beam modulation is close to 100% and no beam sharpening can occur.

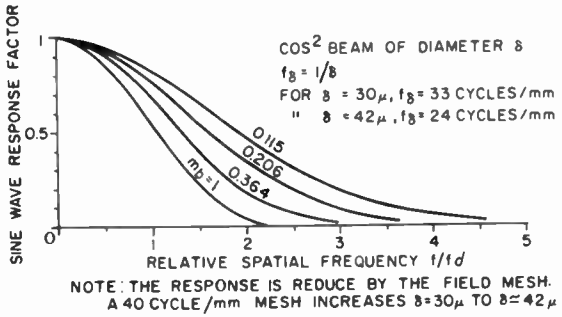

Fig. 9b—Spatial frequency response (MTF) of the self-sharpening beam.

It is noted that the effective line-spread functions are asymmetric, indicating a phase error; also, their centers are shifted ahead of the total beam center, indicating a small geometric displacement (a fraction of the beam radius) in the direction of scanning. The effective beam width decreases further when m_b is reduced by increasing the read-out time ratio t_f/C as shown in Table II and Figure 9(a). The frequency spectrum increases in inverse proportion to the width of the line-spread function, which is closely proportional to the fourth root of the modulation factor of a $\cos^2$ beam;

$$\Delta f/\Delta f_o = \delta_o/\delta \simeq 1/m_b^{1/4}. \tag{25}$$

The corresponding increase in sine-wave response can be very substantial as shown in Figure 9(b), and has been observed in actual operation. For example, the sine-wave response of a 4½-inch vidicon having a 2.2-mil gun aperture measured 44% at 1200 television lines when scanned at 30 frames per second; when the scan was reduced to 15 frames per second, the response increased to 72%; a further reduction by a factor of 5 increased the response to 90% at 1200 television lines.

The discharge of an area is generally accomplished by scanning it on parallel traces. The pitch of the scanning lines or "raster" in the Y direction should be approximately 1/5 of the beam diameter for equal resolution in the X and Y directions, assuming a circular beam having a gaussian or $\cos^2$ line-spread function in all directions.

Thus, the progress of the beam across an edge parallel to the X-direction occurs in incremental steps, leading to beam sharpening very similar to the beam sharpening in the X direction. A high raster line density increases the time required by the beam to pass across a potential step in the Y direction. Because the beam generally moves in a minus Y direction, the bottom edge of the beam will completely saturate as it moves into a positive potential step; however, the trailing top edge will pass over an already discharged area that will reject most or all of the beam electrons.

Returning now to the discharge of a vertical edge (that is, a potential step in the X-direction by a circular beam and not by a line-spread function, which is uniform in the Y direction), it can be seen that the bottom portion (1/5) of the beam area will be saturated, while the top portions will move over previously scanned areas. Thus, the "working" area of the beam is rotated approximately 45° because of the Y component in the beam motion; that is, the center of the working beam area is moved in the resultant direction of the X and Y motions. The effective line cross section given in Table II has the correct value.

It is rotated 45° when the raster line density is chosen to give equal resolution in the X and Y directions. This means that the self-sharpening effect has the computed value in both diagonal directions* but is reduced to $(1/\sqrt{2})$ times the computed value in the X and Y directions. This balance can be altered by changing the ratio of the beam diameter to the raster line density. When the raster pitch is equal to the effective beam diameter (this is the largest pitch permitting discharge of an area without leaving interline charges), the beam is sharpened predominately in the X direction, while a very fine raster pitch turns the working cross section and gives maximum sharpening in the Y direction. This result is substantiated by measurements of the sine-wave-modulation transfer functions in X and Y directions as a function of raster-line density. Thus, it may be of advantage to choose a high raster-line density to increase the Y response of the beam, using the self-sharpening effect to provide a "vertical aperture correction", because its X *response* can be increased by electrical "horizontal" aperture correction in the video system.

7. *Discharge Functions for Variable* α

Figure 10 shows the effect of electron reflection at the storage surface ($\alpha < 1$) on the discharge functions. These curves were computed from the corresponding V/i characteristics shown in Figure 4b. The principle effects are:

(1) The primary beam current I_b' approaching the storage surface is considerably larger for a given signal current (i), resulting in lower beam modulation factors, increased noise, and increased beam-spread functions.

(2) The beam cannot be saturated ($I_s < I_b'$) because of increasing electron reflection, which decreases maximum signal currents and results in negative slopes in the saturation range. This increase in electron reflection requires a corresponding increase in beam current to prevent instability (blocking of high-light signals).

(3) The transfer functions below saturation are similar to those obtained without electron reflection (compare with Figure 7). Their slopes, however, show irregularities introduced by the onset of electron reflection.

The beam modulation factor m_b of existing camera tubes, therefore, has values $m_b \leqq 0.4$.

* The spatial frequency limit imposed by the electrical pass band and raster line density of a standard television system is likewise a maximum in the diagonal directions because of the rectilinear scanning.

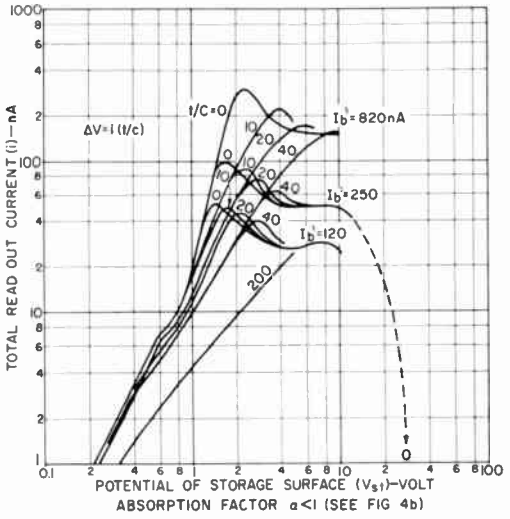

Fig. 10—Current transfer functions $\bar{i}(V_{st})$ of the reading beam from a 1.7-mil gun aperture and an ASOS photoconductor having a variable absorption factor (see Figure 4b).

Table III summarizes the slow-scan read-out characteristics obtained from Figure 10 for a 50 × 50 mm photoconductor having a total capacitance $C = 2500\, C_{(1)} = 0.25\ \mu$F and a collection factor $\alpha\ (V_{st}) < 1$. The potential read out is computed with $\Delta V = i(t_f/C)$, where i is in microamperes and t/C is in seconds/microfarad.

The conversion efficiency (η_c), calculated from Equation (20), is computed for a black-level potential $V_b = 0$, obtainable with a control voltage function $V_c(t) = V_b(t)$. The return-beam modulation $m_b = i/I_b'$

Table III—Read out Characteristics of 50 × 50 mm Photoconductor $(\alpha(V_{st}) < 1)$ Aperture Diameter of Gun = 2 mils

V_{st}	t_f	t/C	i (μA)	I_b' (μA)	$i(t/C)$	η_c	m_b
3.0	2.5	10	0.18	0.820	1.8	0.6	0.22
3.0	5.0	20	0.085	0.300	1.7	0.56	0.28
3.0	10.0	40	0.054	0.250	2.15	0.71	0.215
2.0	2.5	10	0.073	0.250	0.73	0.365	0.29
2.0	5.0	20	0.050	0.180	1.0	0.50	0.28
2.0	5.0	20	0.045	0.120	0.9	0.45	0.275
2.0	7.5	30	0.037	0.120	1.1	0.55	0.25
2.0	10.0	40	0.030	0.120	1.2	0.60	0.25

appears to be relatively low. High resolving power requires small beam currents, favoring the three operating conditions given for $V_{st} = 2$ volts, $I_b' = 120$ nA.

Table III is specific for a storage surface having an absorption factor that varies as a function of potential as shown in Figure 4b. Surfaces having substantially constant absorption factors can be obtained by surface treatment.

IV—Constants and Signal Densities in Television Cameras

Television cameras may contain as many as five noise sources, as shown by the block diagram in Figure 1. The index numbers shown in Figure 1, which indicate an imaging stage or noise source, will be retained throughout the following discussion, even though a particular system may contain fewer stages. The various constants or functions required to compute the signal-to-noise ratio of the system (Equation (12)) are computed as follows.

1. The Carrier Modulation Factors (m_c)

For the television camera shown in Figure 1, the modulation factors of the signal carriers in each of the first three stages are unity, i.e. $m_{c1} = m_{c2} = m_{c3} = 1.0$. (The product P_3 of the intensifier is computed using Equation (12a)). The modulation factor m_{c4} of the storage surface, however, may have a smaller value ($m_{c4} < 1$) because of dark currents, which inject an excess electron density. The modulation factor m_{c5} of the reading beam is likewise smaller than unity. Because charge and discharge signal currents are alike, signal and dark currents in a real camera can be conveniently measured under steady-state operating conditions, that is, $t_f = t_c = t_d = 1/30$ second, and with a small scanned image area (A_m) (for example, $A_m = 50$ to 100 mm^2)†. The dark current ($\bar{i}_d$) of a photoconductor and the total peak (white) charging current ($\hat{i}$) (see Figure 11(a)) can be measured with a d-c meter in the target circuit; the ratio of the total charging current to the beam current approaching the storage surface ($\hat{i}/I_b'$) can be measured with a d-c meter connected to the multiplier output circuit. The beam modulation for the test condition in Figure 11(b) has the reference value,

$$m_{br} = \hat{i}/I_b' \tag{26}$$

and the mean signal current is

$$\bar{i}_s = (\hat{i} - \bar{i}_o)/2 \tag{27}$$

† With blanking removed.

The carrier modulation factor of the storage surface (m_{c4}) is obtained by replacing the particle densities in Equation (3) by appropriate charges;

$$m_{c4} = \overline{V}_s/\overline{V}_{st} = \overline{V}_s/(\overline{V}_s + V_r^* + V_b^* + V_d). \tag{28}$$

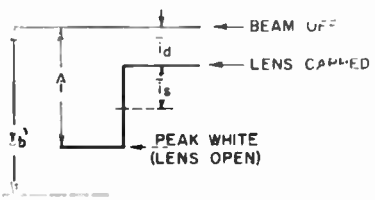

(a)

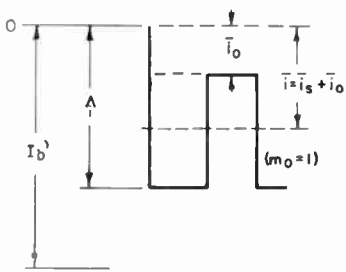

(b)

Fig. 11—Current components of the return beam.

where $\overline{V}_s = \bar{i}_{s(1)} t_c / C_{(1)}$ = *mean* potential of signal charge,

$\overline{V}_r^*$ = residual potential† from a preceding read out,

$\overline{V}_b^* = \bar{i}_{b(1)} t_d' / C_{(1)}$ = mean potential of bias charge from a bias *light* exposure,

$\overline{V}_d = \bar{i}_{d(1)} t_d / C_{(1)}$ = mean potential of dark-current charge.

For numerical evaluations of resolving power as a function of the light exposure $\bar{E}$, it is expedient to use a reference exposure $\bar{E}_r$, computed for a given signal charge, and vary it by an "exposure factor" defined by

$$F_E = \bar{E}/\bar{E}_r \tag{29}$$

† See footnote to Equation (33a) on p. 494.

With this modification, Equation (28) can be written

$$1/m_{c4} = 1 + (V_r^* + \overline{V}_b^*) + V_d/\overline{V}_{s(\text{ref})}\, F_E. \tag{30}$$

The dark-current density $i_{d(1)}$ is a function of temperature and the applied photoconductor voltage (E_T). For ASOS photoconductors at room temperature ($C_{(1)} \simeq 100$ pF), the value $i_{d(1)}$ is of the order of 0.006 to 0.05 nA/mm^2 at $E_T = 5$ to 20 volts. Porous photoconductors ($C_{(1)} \simeq 10$ pF) have higher dark currents because the applied voltage is generally higher to compensate for their lower quantum efficiency (ϵ_4). The exposure $\bar{E} = \bar{E}_r \times F_E$ is computed subsequently in meter-candle-seconds from the incident photon density (see Appendix).

The carrier modulation factor m_{c5} of the read-out beam has the value

$$m_{c5} = \bar{\imath}_s/I_b'. \tag{31}$$

It can be seen from Figure 11(b) that the peak current $\hat{\imath}$ must be given the value

$$\hat{\imath} = (\bar{\imath}_s + \bar{\imath}_o) + m_o\bar{\imath}_s = \bar{\imath} + m_o\bar{\imath}_s \tag{32}$$

to discharge the peak white level of a test object chart at low frequencies where the mean signal modulation, m_o, is unity. Substituting Equations (32) and (26) into Equation (31) yields

$$\begin{aligned} m_{c5} &= m_{br}\left(m_o + \frac{\bar{\imath}_s + \bar{\imath}_o}{\bar{\imath}_s}\right)^{-1} \\ &= m_{br}\left(m_o + \frac{\bar{\imath}}{\bar{\imath}_s}\right)^{-1}, \end{aligned} \tag{33}$$

where $\bar{\imath}_o$ = black-level current (see Equation (19b)). The current ratio in Equation (33) can be replaced in the continuous exposure mode by the potential ratio $\overline{V}_{st}/\overline{V}_s$ because $t_e = t_f = t_d = t_d'$. It follows from Equation (28) that in this case $\bar{\imath}/\bar{\imath}_s = 1/m_{c4}$, and

$$m_{c5} = m_{br}\left[m_o + \frac{1}{m_{c4}}\right]^{-1} \text{ continuous exposure.}\dagger \tag{33a}$$

† In the continuous exposure mode the residual potential V_r^* compensates for the loss in conversion efficiency (η_c), which becomes $\eta_c = 1$. Hence, the term must be deleted; that is, $V_r^* = 0$ in Equation (28) for the continuous exposure mode, where V_r^* establishes an equilibrium potential. The bias light term V_b^* must be deleted when used as a pulsed light during an erase cycle because its residual is contained in V_r^*.

Storage surfaces can be "biased" to introduce a *read-out threshold* at any desired charge level. By setting the threshold voltage to clip off haze and dark-current charges, the signal modulation in the read-out stage is raised. It follows that in this case $i_o = 0$, which results in the following *beam modulation factor (with "clipping"):*

$$m_{cc5} = m_{br}/(m_o + 1). \tag{34}$$

Equation (34) is not applicable to normal steady-state operating conditions because the stored charges below read-out threshold must be removed during an "erase" cycle to prepare the surface for a new exposure.

2. *Signal Densities in a Five-Stage System (Figure 1)*

Starting with the steady-state mean signal current $\bar{\imath}$ computed or measured by scanning a "white" test object of area A_m during a frame time $t_f = t_{e(m)}$, the mean signal current density $\bar{\imath}_{s(1)}$ per mm² is

$$\bar{\imath}_{s(1)} = \bar{\imath}/A_m. \tag{35}$$

The mean unit charge $\bar{q}_{(1)}$ is obtained using Equation (15a);

$$\bar{q}_{(1)} = C_{(1)}\overline{V} = \bar{\imath}_{s(1)\text{ref.}} t_e/F_E,$$

where the relative exposure factor F_E defined by Equation (29) has been added.

Peak potentials of the storage surface are given by

$$V_{st} = \bar{\imath}_{s(1)\text{ref}}\,(1 + m_o)\,F_E t_e/C_{(1)} \tag{36}$$

to establish a relative exposure scale calibrated in volts of target potential.

The mean signal electron density in the storage surface obtained with Equation (15b) is given by

$$\begin{aligned}\bar{n}_{(1)4} &= \bar{\imath}_{s(1)\text{ref.}} t_e F_E/\bar{q}_e \\ &= 6.25 \times 10^{18}\,\bar{\imath}_{s(1)\text{ref.}} t_e F_E \text{ ampere second.}\end{aligned} \tag{37}$$

For the system of Figure 1, the remaining signal densities are computed using this value, as follows:

$$\begin{aligned}
&\text{input photons to intensifier} && \bar{n}_{s(1)1} = \bar{n}_{s(1)4}/(\epsilon_4 |g|_{ph}),\\
&\text{photo electrons} && \bar{n}_{s(1)2} = \bar{n}_{s(1)4}\epsilon_2/(\epsilon_4 |g|_{ph}),\\
&\text{photons to storage surface} && \bar{n}_{s(1)3} = \bar{n}_{s(1)4}/\epsilon_4,\\
&\text{output signal electrons} && \bar{n}_{s(1)5} = \bar{n}_{s(1)4}/\epsilon_5, \qquad (38)
\end{aligned}$$

where ϵ_2 = effective quantum efficiency of the photoemitter,

ϵ_4 = effective quantum efficiency of the storage surface,

ϵ_5 = transfer efficiency of the stored charges to the electron multiplier, calculated using Equation (21),

$|g|_{ph}$ = photon gain of intensifier.

The effective quantum efficiency of good photoemitters (ϵ_2) is in the order of 10%, whereas photoconductors have efficiency values (ϵ_4) ranging from 0.1 to 0.75 % depending on the applied voltage. The transfer efficiency of the reading beam, in tubes with electron multiplier, is equal to the field mesh transmission factor τ_m in the steady-state operating mode ($t_f = t_c$), where an equilibrium potential is established. In the slow-scan mode, the frame time (t_f) may be shorter than required for a complete discharge, leaving a residual charge (V_r) that must be erased before a new exposure can be made. The transfer efficiency ϵ_5 as given by Equation (21) is reduced by the incomplete discharge.

3. *Spatial Frequency Response (Sine-Wave Modulation Transfer Functions, MTF).*

The resolving power of a low-velocity beam is determined, in principle, by the size of the electron source which, in turn, is defined by the exit aperture of an electron gun and by the characteristics of the electron optic that images this source on the storage surface.

The size of the image is determined by the magnification (M), which should be smaller than unity, and by the electron point-spread function of the optic. An ideal electron optic can image any point source of electrons in the defining aperture of the electron gun as a point on the storage surface. The resolving power of the electron beam is then determined entirely by the size of the defining aperture of the electron source, the image magnification, and the distribution of electron velocities in the defining aperture. The size of the effective beam landing on the storage surface is smaller than the aperture. The rejection of low-energy electrons by a low landing potential at

the storage surface does, in fact, result in a smaller effective beam diameter and a higher resolving power than obtained with a high-velocity beam. For example, a defining aperture of 15-micrometer diameter, with a magnification $M = 0.5$ and a $\cos^2$ velocity distribution, would yield a beam-resolving power of the order of 260 cycles/mm and a 50% sine-wave response factor at 140 cycles/mm. It is apparent that the point image spread function of the real electron optic is a determining factor in approaching this performance.

The electron density and velocity distribution in the defining aperture of the electron gun are prominent factors in the development of signals from stored charges at the target by absorption modulation.

Thus, the modulation transfer function (MTF), in large measure, is a function of the quality of the electron optic. A new electron optic differing substantially from those used in commercial cameras has been designed by the author for high-definition camera tubes.* The electron gun in the camera tube defines a small source of electrons that is imaged by the electron optic on the storage surface. Fields are provided to deflect the electron beam emerging from the gun aperture so that it scans the image area and to decelerate the beam electrons to a low landing velocity (V_{st}) at the storage surface. Therefore, the diameter of the beam at the storage surface depends on the diameter and velocity spread function of the electron source at the defining aperture as well as on the image magnification and spread-function of the electron optic. This electron optic is a pure magnetic optic that provides a uniform phase correction for deflected electron trajectories by special magnetic field functions without the use of electrostatic-lens fields. The aperture magnification is $M = 0.5$, and the optic provides a flat field of focus, uniform landing, and a substantially uniform MTF (within 5%) without astigmatism in the image field and requires no dynamic corrections. Thus, in a large image surface, the MTF is substantially independent of the scanned area and can be measured by scanning a small area (1 cm^2) in $t_f = 1/30$ second in the continuous exposure mode.

The MTF's, curves 4 and 5 in Figure 12, that refer to a high-resolution gun (1-mil aperture) and a standard gun (1.5- to 2-mil aperture), respectively, were measured in 4.5-inch camera tubes having an electron optic of 27-to 28-cm focal distance and 4 nodal points, a field mesh of 1000 and 750 wires/inch respectively, operated at $E_{mesh} = 500$ volts, and a magnetic field strength at the storage surface of 70 gauss.

* This work was sponsored by the Air Force Avionics Laboratory, Wright-Patterson Air Force Base, Ohio, Contract AF33(657)-7939.

These MFT's are also obtainable *at the center* of the storage surface with standard small-format electron optics in 1-inch or ½-inch vidicons.

The MTF curve 3 in Figure 12, labeled "superbeam, 140-gauss field," is representative of the performance of a new electron optic of shorter focal length computed for experimental 2-inch high-resolution camera tubes that contain an electron multiplier and have

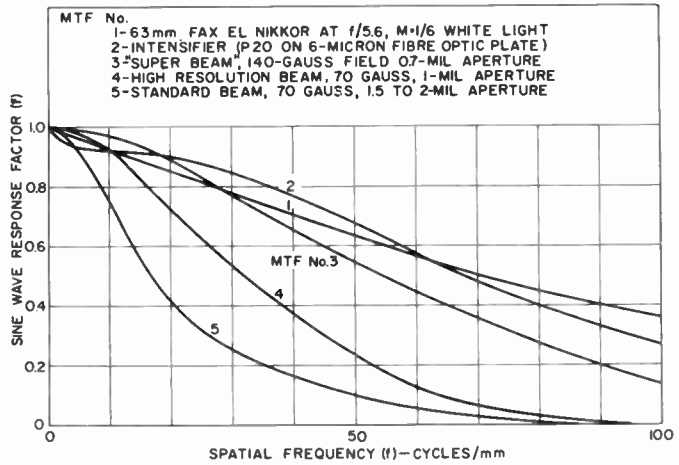

Fig. 12—Sinewave modulation transfer functions (MTF's) of television cameras.

an image format of 25 × 25mm. This electron optic has a 14-cm focal distance and 4 nodal points. It is scaled down from the larger optic by a factor of two, but the magnetic field strength is doubled. This design reduces the point spread-function of the optic to one half, and in combination with a correspondingly finer field mesh and a 0.7 to 0.5-mil gun aperture, increases the frequency scale of the MTF by a factor of two compared with the larger optic.

4. *Bandwidth Factors*

The bandwidth factors $\rho_{(w)}$ for the various noise sources are computed from the sine-wave modulation transfer functions $\bar{r}(f)$ of all system elements and their products. Curve 1 of Figure 12 shows the sine-wave modulation transfer function of an excellent $f/5.6$ camera lens, capable of covering a 50 × 50-mm area with substantially uniform frequency response. The MTF of an image intensifier is the function $\bar{r}_I(f)$ that represents the combined response of stages 2 and

3 in Figure 1. The MTF of the intensifier is dominated by the light diffusion in stage 3 (intensifier phosphor and fibre-optic coupling) and may be represented by curve 2 of Figure 12. The MTF of the read-out system (stage 5) is the function $\bar{r}_B(f)$, which is the combined response of the storage surface (stage 4), the field mesh, and the reading beam. Typical MTF curves for aperture correction in the video amplifier (stage 6) are shown in Figure 3.

In terms of spatial frequencies $f = N/2$, the bandwidth factors for the noise sources in Figure 1, may be computed, using Equation (10b), with the following conditions specified:

$$\begin{aligned}
\text{photoelectrons } \rho_{(w)\,2\text{-}6} &= \frac{1}{f_r}\int_0^{f_r} (\bar{r}_I\,\bar{r}_B\,\bar{r}_C)^2\,df \\
\text{intensifier phosphor } \rho_{(w)\,4\text{-}6} &= \frac{1}{f_r}\int_0^{f_r} (\bar{r}_B\,\bar{r}_C)^2\,df \\
\text{stored charges } \rho_{(w)\,4\text{-}6} &= \frac{1}{f_r}\int_0^{f_r} (\bar{r}_B\,\bar{r}_C)^2\,df \\
\text{reading beam } \rho_{(w)6} &= \frac{1}{f_r}\int_0^{f_r} (\bar{r}_C)^2\,df
\end{aligned} \tag{39}$$

The absolute signal-to-noise ratio of the system can now be computed using Equations (12) and (12a) for the product P_3. To solve for the test object modulation m_o at a given resolving power (f_r) as given by Equation (14), the spread factor of the system must be computed with

$$S_{\text{syst}} = [1 + (0.2\,f_r/f_c)^2]^{1/2} \tag{40}$$

where

$$f_c = \int_0^{f_r} (\bar{r}_L\,\bar{r}_I\,\bar{r}_B)^2\,df,$$

and the system response is

$$\bar{r}_{\text{syst}} = \bar{r}_L\,\bar{r}_I\,\bar{r}_B\,\bar{r}_C. \tag{41}$$

Equation (14) must be solved by successive approximation because Equations (32), (33), or (34) contain m_o.

5. *Modifications for Systems Containing Fewer Stages*

The resolving power functions f_r (m_o, E) of vidicons are computed with $\bar{n}_{s(1)1} = \bar{n}_{s(1)3} = \bar{n}_{s(1)4}/\epsilon_4$ in Equation (38). The intensifier (stages 2 and 3) is eliminated by letting the products P_2 and P_3 in Equation (12) equal zero, and setting $\bar{r}_I(f) = 1$ in Equation (39), (40), and (41).

The resolving power of image orthicons is computed as for image-intensifier vidicons having a low target capacitance (smaller currents) and by replacing the photon gain by a secondary gain. Thus, the signal densities in Equation (38) are

$$\bar{n}_{s(1)1} = \bar{n}_{s(1)4}/(|g|\ \epsilon_2) \quad \text{(input photons)},$$

$$\bar{n}_{s(1)2} = \bar{n}_{s(1)4}/|g| \qquad \text{(photoelectrons)},$$

where $|g|$ is the secondary emission gain of storage surface ($|g| = 2$ to 4). The phosphor noise source of the intensifier is eliminated by letting the product P_3 in Equation (12) equal zero.

To compute the performance of the camera tube alone, the lens function $\bar{r}_L(f)$ and the aperture correction function $\bar{r}_C(f)$ can be set to equal unity.

V—Quantum Limitations and Resolving Power of Television Cameras (Graphic Solutions of the Functions $f_r(\bar{E})$)

The quantum limitations and the effects of the modulation transfer function on the resolving power of a television camera can be understood more clearly by breaking up the relatively complex general solution into partial solutions that can be refined progressively. The graphic representation of resolving power (f_r) as a function of exposure ($\bar{E}$) minimizes numerical computations, because the quantum limits due to photoelectrons, grains, or dark currents are straight lines in log-log coordinates. The maximum mean level exposure $\bar{E}_1$ of a camera tube is determined by the maximum charge density $\bar{n}_{s(1)4}$ that can be stored and read out from its storage surface, and by the efficiency of the conversion process from radiation energy into charges. Because the charge that can be read out is equal to $(\bar{\imath}_s t_f)$, the mean signal current $\bar{\imath}_s$ has relatively high values for fast-scan conditions (small t_f) and much lower values for slow-scan conditions. Hence, the maximum exposure $\bar{E}_1$ may be limited by the potential limit of the storage surface or by the current limit of the electron gun. The latter can be increased by using a larger reading-beam diameter which, however, reduces its MTF. Therefore, a high-definition readout generally

requires longer frame times, which, in turn, are limited by dark current and the storage characteristics of the particular surface.

The maximum signal-current density $\bar{\imath}_{s(1)}$ permitted by the potential limit of the storage surface can be computed using Equation (36). The corresponding photon density $\bar{n}_{s(1)1}$ follows from Equations (37) and (38), or as discussed in Section IV-5. The mean level exposure $\bar{E}$ is computed in meter-candle-seconds as is customary for photographic emulsions. Its value depends on the spectral sensitivity of the photon conversion surface and on the spectral characteristics of the illuminant (see Appendix). For calculation purposes, a daylight illuminant (5000°K) and a spectral sensitivity equaling the standard luminosity function will be assumed. The conversion equation is then

$$\bar{E} = \bar{n}_{s(1)1}/7.5 \times 10^9 \text{ (m.c.s.)}, \tag{42}$$

where $n_{s(1)1}$ = incident radiation or photon density/mm^2

(1) Absolute Quantum Limits

The absolute photon limit of the resolving power is computed as follows. The basic quantum limitation of the resolving power by available radiation energy, converted 100% into photoelectrons as assessed by Rose,[4] is expressed by the difference signal-to-noise ratio $(R\Delta) = K = [\bar{n}_{s(1)1}{}^{1/2}][\bar{a}^{1/2}][2m_o]$ (compare with Equation (8)). The photon density $\bar{n}_{s(1)1}$ in the sampling area $\bar{a} = 5/N^2 = 1.25/f_r{}^2$ of one bar of the standard 3-bar test object has the value

$$\bar{n}_{s(1)1} = K^2 f_r{}^2/(5m_o{}^2). \tag{43}$$

By substitution of Equation (43) into (42), the exposure $\bar{E}$ required for a 100% conversion efficiency is

$$\bar{E} = \bar{E}_o/m_o{}^2,$$

where

$$\bar{E}_o = 0.267\, K^2 f_r{}^2 \times 10^{-10}, \tag{44}$$

m_o is the modulation factor of the test object, $m_o = (C-1)/(C+1)$ (C = contrast ratio), K is the threshold signal-to-noise ratio, and f_r is the resolving power in cycles/mm. *The absolute photon limit of the resolving power* is thus a one-half-power function of the exposure;

$$f_r = 1.94 \times 10^5 \bar{E}^{1/2} m_o/K. \tag{45}$$

The photoelectric quantum limits of photoemitters or photoconductors are obtained by multiplying the exposure $\bar{E}$ calculated from Equation (44) by the factor $(1/\epsilon)$, where ϵ is the effective quantum efficiency of the conversion surface;

$$\bar{E} = \bar{E}_0/(m_0^2\epsilon). \tag{46}$$

The resolving power (f_r) as a function of mean exposure $\bar{E}$ is illustrated in Figure 13 for several values of ϵ, a threshold value $K = 3.6$, and a

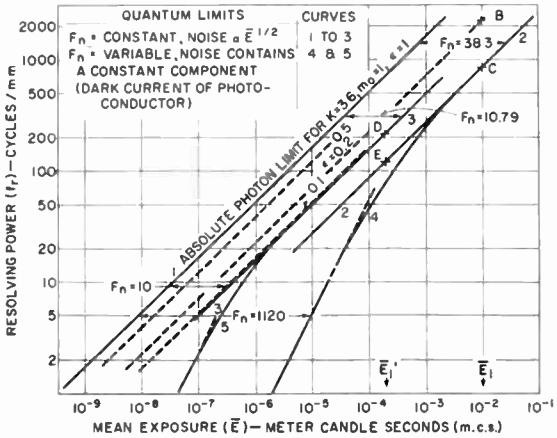

Fig. 13—Quantum-limited resolving power functions.

test object modulation $m_0 = 1$. The quantum efficiency of photoconductors varies from $\epsilon = 0.1$ to $\epsilon = 1.0$ depending on the material and applied potential. Good photoemitters have a 10% quantum efficiency, whereas the fastest photographic emulsions approach a quantum efficiency of only one percent.

These basic relations make no allowance for excess particle densities or "dark" charges injected by modulation carriers of transfer processes (dark current of photoconductor or the read-out beam), nor do they account for the substantial reduction of the modulation factor (m_0) by the MTF's of the imaging and readout systems. Hence, the exposure $\bar{E}$ must be increased by considerably larger factors than given by Equation (46).

(2) Quantum Limits Including Excess Particle Densities

For this purpose, it is assumed that *MTF's are not degrading the modulation.* Thus, in the general expression for the unit signal-to-

noise ratio $|R|_{(1)\text{syst}}$ of the system as given by Equation (12), the square-wave response ($r\bar{\Delta}$), input modulation (m_o), and all bandwidth factors $\rho_{(w)}$ are assumed to equal unity. By expressing the various signal densities from Equation (38) in terms of the photon density, the unit signal-to-noise ratio of an intensifier vidicon camera with electron multiplier simplifies to

$$|R|^2_{(1)\text{syst}} = \bar{n}_{s(1)1}\left(\frac{1}{\epsilon_2} + \frac{\bar{n}_{s(1)4}}{\epsilon_4|g|_{\text{ph}}\,|R|^2_{(1)\text{phos}}} + \frac{1}{m_{c4}\epsilon_4|g|_{\text{ph}}\,\gamma^2_4} + \frac{1}{m_{c5}\epsilon_4\epsilon_5|g|_{\text{ph}}\,\gamma^2_5}\right)^{-1} \tag{47}$$

The index numbers correspond to the intensifier vidicon system shown in Figure 1. The photon-limited resolving power can be restored in a system having a degraded signal-to-noise ratio by increasing the photon input density $\bar{n}_{s(1)1}$ by a factor F_n, called the "exposure factor", which is equal to the increase in mean-squared noise. Hence, the exposure must be increased to

$$\bar{E} = \bar{E}_o F_n. \tag{48}$$

For intensifier vidicons with electron multipliers, the exposure factor F_n is the denominator of Equation (47);

$$F_n = \frac{1}{\epsilon_2} + \frac{\eta_{s(1)4}}{\epsilon_4|g|_{ph}|R|^2_{(1)\text{phos}}} + \frac{1}{m_{c4}\epsilon_4|g|_{\text{ph}}\,\gamma^2_4} + \frac{1}{m_{c5}\epsilon_4\epsilon_5|g|_{\text{ph}}\,\gamma^2_5}. \tag{49}$$

The exposure factor for an image-orthicon camera is similar;

$$F_n = \frac{1}{\epsilon_2} + \frac{1}{\epsilon_2|g|} + \frac{1}{m_{c5}\epsilon_2|g|\epsilon_5\,\gamma^2_5}, \tag{50}$$

where $|g|$ = secondary emission gain of target. For a *vidicon with an electron multiplier*, the exposure factor is given by

$$F_n = \frac{1}{m_{c4}\epsilon_4\,\gamma^2_4} + \frac{1}{m_{c5}\epsilon_4\epsilon_5\,\gamma^2_5}. \tag{51}$$

The symbols in Equations (49), (50), and (51) have the previously established meanings;

ϵ_2 = quantum efficiency of photoemitter,

ϵ_4 = quantum efficiency of photoconductor,

$|g|_{ph}$ = photon gain of intensifier,

$|g|$ = secondary emission gain of image orthicon target,

$\epsilon_5 = \eta_5\tau_m$ = read-out efficiency—see Equation (21)

γ_n = point gamma of system from input to stage n (this term is omitted when $\gamma_n = 1$)

$1/m_{c4}$ $= 1 + (V_r^* + \overline{V}_b^* + \overline{V}_d)/V_{s(ref)}F_E$† (Equation (30))

$1/m_{c5}$ $= (m_o + i/i_s)/m_{br}$ (Equations (33) or (33a) for continuous exposure.)

It is evident from Equations (48) and (49) that insertion of a photon or electron gain stage ($|g|$) reduces the noise contributions from the stages following stage 2. The total quantum limit, however, can never reach the absolute photon limit because the first two stages alone require an exposure factor $F_n \simeq 10$ for the best photoemitters ($\epsilon_2 \simeq 0.1$). A high preamplification of signals has the disadvantage of reducing the maximum resolving power of the system as follows:

$$\bar{E}_1' = \bar{E}_1/|g|.$$

The degradation of resolving power by quantum limitations can be demonstrated by the following numerical examples.

(a) Storage surfaces without dark current, continuous exposure.

Given are the black-level potential $(\overline{V}_b + \overline{V}_d) = 0$, $\epsilon_4 = 0.2$, $\gamma_4 = \gamma_5 = 1$, $m_{br} = 0.4$, $\tau_m = 0.75$, $m_o = 1$. It follows from Equation (30) that $m_{c4} = 1$, and from Equation (33) that $m_{c5} = 0.2$. The read-out efficiency is $\epsilon_5 = \tau_m = 0.75$ in the continuous exposure mode. Hence, the exposure factor from Equation (51) is $F_n = 5 + 33.3 = 38.3$; thus the required exposure is $\bar{E} = 38.3\,\bar{E}_o$, where $\bar{E}_o$ is given by Equation (44). The quantum limits $f_r(E_o)$ and $f_r(\bar{E})$ for $K = 3.6$ are shown by curves 1 and 2 in Figure 13. The functions can be located by calculation of a single value because F_n is a constant. The beam current is adjusted at all exposures to maintain a constant modulation m_{br}.

† $V_r^* = 0$ for continuous exposure mode

The addition to the above vidicon of an intensifier section that has a photon gain $|g|_{ph} = 50$ and a quantum efficiency $\epsilon_2 = 0.1$ decreases the exposure factor to $F_n = 10 + 0.02 + 0.1 + 0.67 = 10.79$ (Equation (48)). The resulting exposure is calculated as $\bar{E} = 10.79\,\bar{E}_o$; the corresponding quantum limit is given by curve 3 in Figure 13. The gain in absolute sensitivity by a photon amplification $|g|_{ph} = 50$ is only 3.55; the capacitive lag, however, is reduced by a large factor.

The effect of the intensifier stage on the quantum-limited resolving power is readily assessed from Figure 13. Assume, for example, a maximum exposure for a photoconductor of $E = 10^{-2}$ meter-candle-seconds. The addition of the intensifier ($|g|_{ph} = 50$) reduces the maximum exposure to $\bar{E}_1' = 2 \times 10^{-4}$ meter-candle-second. The absolute photon limit at the exposure $\bar{E}_1$ would yield a resolving power $f_r = 5200$ cycles per mm. The photoconductor conversion noise ($\epsilon_4 = 0.2$) decreases the resolving power to $f_r = 2180$ cycles per mm (point B), and the read-out beam noise decreases further to 850 cycles per mm (point C).

When the intensifier is added, the maximum resolving power is reduced from point C to point D (Figure 13), i.e., from 850 to 215 cycles per mm because the maximum exposure is now $\bar{E}_1'$. However, the resolving power at this exposure is 1.8 times higher than that obtained without the intensifier. It is seen further from Figure 13 that the quantum limit of the intensifier tube (curve 3) approaches closely the quantum limit ($\epsilon_2 = 0.1$) of its photoemitter, demonstrating that amplification ahead of the read-out stage can overcome the limitations caused by beam noise at reduced exposure levels.

(b) Quantum limits including dark current (continuous exposure)

Because of the excess particle density introduced by dark current, the exposure factor F_n is a function of exposure and the read-out delay time t_d as expressed by the carrier modulation factor m_{c4}. If it is assumed, for example, that $\bar{V}_b = 0$ and $\bar{V}_{s(ref)} = 2$ volts at the maximum exposure $\bar{E} = 10^{-2}$ meter-candle-second, where $F_E = 1$ and $\bar{V}_d = 0.1$ volt, the carrier modulation factor of the storage surface is $m_{c4} = 1/(1 + 0.05/F_E)$. The factor F_n computed with the constants of the two preceding examples is given in Table IV.

The resolving powers for the functions $f_r(\bar{E})$ are the values f_r of the absolute photon limit function $f_r(\bar{E}_o)$ at the exposures $\bar{E}_o = \bar{E}/F_n$. For a vidicon without an intensifier the quantum-limit resolving power as function of mean exposure is given by curve 4 in Figure 13. At high exposures, the dark current is negligible; thus curve 4 coincides

with curve 2. At low exposures, the constant dark current noise becomes dominant, and the signal-to-noise ratio and resolving power (f_r) become linear functions of exposure.

When an intensifier is added, the dark current and beam noise become small compared to the photoelectron noise, as shown by the

Table IV—Calculation of F_n for a Vidicon
($\epsilon_t = 0.2$, $m_{br} = 0.4$, $\tau_m = 0.75$, $m_o = 1$, $i/i_s = 1/m_{ct}$)

(a) *Without Intensifier* (Figure 13, Curve 4)

F_E	$\bar{E}$	F_n (Eq. 51)	$\bar{E}_o = \bar{E}/F_n$
1	10^{-2}	5.25 + 34.1 = 39.4	2.53×10^{-4}
0.315	3.15×10^{-3}	5.25 + 34.1 = 41.6	7.56×10^{-5}
0.1	10^{-3}	7.5 + 41.6 = 49.1	2.03×10^{-5}
0.0315	3.15×10^{-4}	13.0 + 60.0 = 73.0	4.31×10^{-6}
0.01	10^{-4}	30.0 + 116.0 = 146.0	6.85×10^{-7}
0.001	10^{-5}	255.0 + 865.0 = 1120.0	8.95×10^{-9}
0.000315	3.15×10^{-5}	800.0 + 2670.0 = 3470.0	0.91×10^{-9}

(b) *With Intensifier** $|g|_{ph} = 50$ (Fig. 13, Curve 5)

F_E	E	F_n (Eq. 49)	$\bar{E}_o = \bar{E}/F_n$
1	2×10^{-4}	10.0* + 0.105 + 0.682 = 10.8	1.85×10^{-5}
0.315	6.3×10^{-5}	10.0 + 0.114 + 0.716 = 10.8	5.82×10^{-6}
0.1	2×10^{-5}	10.0 + 0.150 + 0.832 = 10.95	1.82×10^{-6}
0.0315	6.3×10^{-6}	10.0 + 0.26 + 1.2 = 11.49	5.50×10^{-7}
0.01	2×10^{-6}	10.0 + 0.60 + 2.32 = 12.94	1.55×10^{-7}
0.001	2×10^{-7}	10.0 + 5.0 + 17.3 = 32.3	6.2×10^{-9}
0.000315	6.3×10^{-8}	10.0 + 16.0 + 53.5 = 79.5	7.95×10^{-10}

* The phosphor grain noise is assumed to be negligible

values in Table IV. For a vidicon with an intensifier, the resolving power as a function of mean exposure is given by curve 5 in Figure 13. This quantum limit curve coincides with curve 3 at higher exposures, and the dark current limit is shifted to lower exposures by a factor approaching the photon gain. Thus, the gain in absolute sensitivity realized by preamplification is considerably higher than in image orthicons.

(c) *Quantum limits for the single-exposure read-out mode ($t_e < t_f$)*

The exposure factor F_n is computed from Equations (49), (50), or (51). However, because the conversion efficiency η_c decreases as $\bar{E}$ and

$\overline{V}_s$ decrease, the transfer efficiency ϵ_5 is now a function of exposure. Hence, the values η_c must be computed as a function of $\bar{E}$ (or F_E). The maximum potential of the storage surface V_{st} is selected to obtain the maximum permissible current, as determined from Figure 7 or Figure 10; the value η_c is computed using Equation (20) as a function of $\overline{V}_s$ and $\bar{E}$ for the particular time ratio t_f/C. The carrier modulation factor m_{c4} is no longer single valued for a given frame time because the read-out delay time t_d is a variable. At the beginning of the read-out time, $t_d = t_e$; at the end of the read-out time, it has increased to $t_d = t_f$. Therefore, during the frame time, the quantum limit curve of the dark current charges shifts towards higher exposures. A sample calculation given in Section V-3, which follows, demonstrates, however, that the dark-current limitation is only a second-order effect compared to the reduction of η_c. Furthermore, the gamma of the read-out process may be higher than unity so that γ_5 may be larger than unity when all preceding stages have unity gamma.

(3) The Loss of Resolving Power by the Modulation Transfer Function (MTF)

The quantum limits can be approached in real cameras only at low exposures and resolving powers because it is impossible to design light and electron optics that do not degrade the square-wave modulation (m_o) of the test object at higher resolving powers. The complete expression for resolving power (f_r) as a function of mean exposure is obtained by combining Equations (12), (38), (14), and (42);

$$\bar{E} = \bar{E}_o(f_r)\ F_n' S_{\text{syst}}/[m_o r\bar{\Delta}_{\text{syst}}(f_r)]^2,$$

where $\bar{E}_o(f_r)$ = photon limit computed with Equation (44) and F_n' = exposure factor computed with Equations (49), (50), or (51) in which the terms are multiplied by their respective bandwidth factors $\rho_{(w)}$. *The mean square-wave response factor* $r\bar{\Delta}_{\text{syst}}(f_r)$ of a system can be determined from the sine-wave MTF by the Fourier series

$$r\bar{\Delta}_{\text{syst}} = \frac{8}{\pi^2}\left(\bar{r}_f + \frac{1}{9}\bar{r}_{3f} + \frac{1}{25}\bar{r}_{5f} + \ldots\right)$$

When $\bar{r}_{\text{syst}} < 0.7$, the first term alone is sufficient and yields

$$r\bar{\Delta}_{\text{syst}} = 0.81\ \bar{r}_{\text{syst}}.$$

where the system reponse $\bar{r}_{syst}$ is the product of the reponse factors of each stage involved (see Equation (41)).

The bar length spread factor S_{syst} and the bandwidth factors $\rho_{(w)}$ can be omitted for most practical purposes, because they have second-order effects that partly cancel one another. Hence, the equation for the exposure $\bar{E}$ containing the correction for the MTF of the system can be simplified to

$$\bar{E} \simeq (\bar{E}_o/r\bar{\Delta}_{syst}{}^2)_{f_r} F_n/m_o{}^2. \tag{52}$$

Equation (52) has been written in this form because $r\bar{\Delta}$ is a function of resolving power (f_r) which, in turn, is a function of $\bar{E}_o$. The simultaneous solution for f_r requires a plot of the continuous function $f_r(\bar{E}_o/r\bar{\Delta}_{syst}{}^2)$.

The procedure is to compute the factor F_n for an exposure $\bar{E}$ and the corresponding exposure $E'' = \bar{E}m_o{}^2/F_n$, which is the exposure on the function $f_r(\bar{E}_o/r\bar{\Delta}_{syst}{}^2)$. The value f_r at this exposure is the resolving power at the exposure $\bar{E}$.

It is instructive in many cases to use the following alternative solution, starting with a plot of the quantum limit function $f_r(E_oF_n)$ as discussed in the preceding section. When this function is one-half-power function, the equation for mean exposure containing the correction for MTF becomes

$$\bar{E} = \bar{E}_oF_n/(m_or\bar{\Delta}_{syst})^2 \quad (\text{for } F_n = \text{constant}). \tag{53a}$$

When a constant noise source dominates the system noise, the function $f_r(\bar{E}_oF_n)$ is linear and the MTF correction is

$$\bar{E} = \bar{E}_oF_n/(m_or\bar{\Delta}_{syst}) \quad (\text{for constant noise}) \tag{53b}$$

because signal and resolving power are proportional to the exposure E. The MTF correction for the one-half-power and linear sections of a composite quantum limit function, such as given by curve 4 in Figure 13, can be made separately or may be made by the first solution given for Equation (52) as shown by the following examples:

(a) Image Orthicons (Continuous-Exposure Mode)

The quantum limit curve 2 in Figure 14 is obtained from Equations (50) and (48) for the constants $\epsilon_2 = 0.1$, $|g| = 3$, $m_{c4} = 1$, $m_o = 1$, $m_{br} = 0.4$ and $\epsilon_5 = 0.75$. The exposure factor from Equation (50) is

$F_{no} = 10 + 3.33 + 22.2 = 35.5$. The exposure limit $\bar{E}_1$ may be computed for the constants $C_{(1)} = 0.35$ pF, $V_{st} = 2.5$ volts and $t_e = 1/30$ sec. Equation (36) gives the mean signal current $\bar{\imath}_{s(1)4} = 0.0132$ nA/mm^2. The mean charge density obtained from Equation (37) is $\bar{n}_{s(1)4} = 2.75 \times 10^6$, and the photon density is $\bar{n}_{s(1)1} = \bar{n}_{s(1)4}/|g|\epsilon_2 = 9.15 \times 10^6$. Hence, the maximum mean level exposure from Equation (42) is $\bar{E}_1 = 1.22 \times 10^{-3}$ meter-candle-second, as indicated in Figure 14. (The peak highlight exposure for $m_o = 1$ is twice this value).

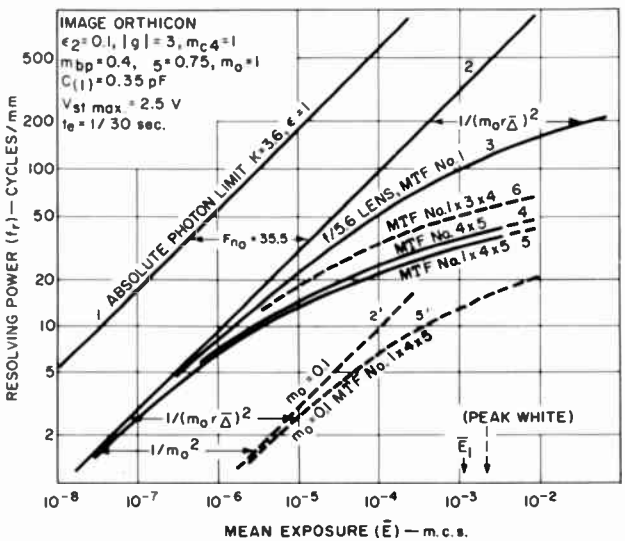

Fig. 14—Quantum limits and resolving power of image orthicons, continuous-exposure mode.

The effect of the MTF's is shown by multiplying the exposures of curve 2 by $1/r\bar{\Delta}^2$ according to Equation (53a). Curves 3 to 6 show the progressive degradation in resolving power caused by an excellent camera lens (curve 3), the image section, and the reading beam. The corresponding MTF's are given in Figure 12.

At maximum exposure ($\bar{E}_1$) the quantum limit of the resolving power is 300 cycles per mm. The lens decreases this value to 100 cycles per mm-sec. and the MTF product $1 \times 4 \times 5$ further decreases this value to 32 cycles per mm.

The MTF combination shown by curve 6 may represent an upper limit of improvement of the image-orthicon camera. At present, a target spacing of less than 1 mil and a high-voltage image section (with zero crosstalk) are required to realize these MTF values. The MTF

combinations in curve 4 or 5 may represent the top-level performance of present 3-inch image orthicons. The low-contrast resolving power ($m_o = 0.1$) is indicated by curves 2′ and 5′.

The addition of an intensifier stage to an image orthicon produces the following effects.

First, the exposure factor F_n is decreased by an amount proportional to the photon gain $|g|_{ph}$. The exposure factor computed from Equation (48) for $m_{c4} = 1$ and $\epsilon_4 = |g|$ is calculated to be $F_n = 10.5$ for $|g|_{ph} = 50$. This value approaches (within 5%) the quantum limit set by the photoemitter ($\epsilon_2 = 0.1$). The improvement in absolute sensitivity is only $35.5/11.5 = 3.16$. The capacitive lag at low light levels, however, is greatly decreased because the potentials of the storage surface are increased by the photon gain factor.

Second, the exposure limit decreases from $\bar{E}_1 = \bar{E}_1/|g|_{ph}$, which, in turn, reduces the maximum resolving power.

Third, the resolving power decreases, by a factor of $(1/r\bar{\Delta}_I^2)$ as a result of the MTF of the added image section.

Thus, the main advantage of an intensifier image orthicon is reduced capacitive lag at very low light levels. Wide-spaced, low-capacitance targets increase the relative high-frequency response at higher exposures because of electron redistribution, which depresses low frequencies and the d-c component. Thus, the observed resolving power may exceed the values computed for a *normal* image because of the bandwidth reduction caused by the differentiation.

(b) Vidicons (Continuous Exposure Mode)

Given are the constants $\epsilon_4 = 0.5$, $\epsilon_5 = 0.75$, $m_o = 1$, $m_{br} = 0.4$, $\bar{V}_b = 0$, $C_{(1)} = 100$ pF, $t_c = t_d = 1/30$ sec, $\bar{\imath}_{d(1)} = 0.02$ nA/mm^2. The maximum signal current density for a peak white signal of 200 nA in an area $A = 1$ cm^2 has the value $\bar{\imath}_{s(1)4} = 1$ nA. The mean charge density computed from Equation (37) is $\bar{n}_{s(1)4} = 2.08 \times 10^8$ for $F_E = 1$. Hence, the photon density is $\bar{n}_{s(1)1} = 4.16 \times 10^8$, and from Equation (42) $\bar{E}_1 = 5.55 \times 10^{-2}$ meter-candle-second. The exposure factor for zero dark current ($m_{c4} = 1$) computed from Equation (51) is $F_{no} = 15.3$. Therefore, the corresponding quantum limit, shown by curve 2 in Figure 15 is spaced from the absolute photon limit (curve 1) by the amount of this factor. The variable factor F_n for the quantum limit containing dark current (computed with Equation (51)) is given by curve 3 in Figure 15. The linear section of curve 3 is extended by a broken line to intersect curve 2 at the point P. The effect of the MTF for the one-half power curve (curve 2), calculated from Equation (53a)

is given by curve 2F; the MTF correction for the linear section of curve 3 (with extension) calculated from Equation (53b) is shown by curve 3F. The two branch curves cross at the exposure level indicated by point P. The final solution, curve 4, is displaced horizontally from curves 2F and 3F in the transition region by the same factors (distances on a log E scale) by which curve 3 is displaced from curves 2 and the extension of curve 3.

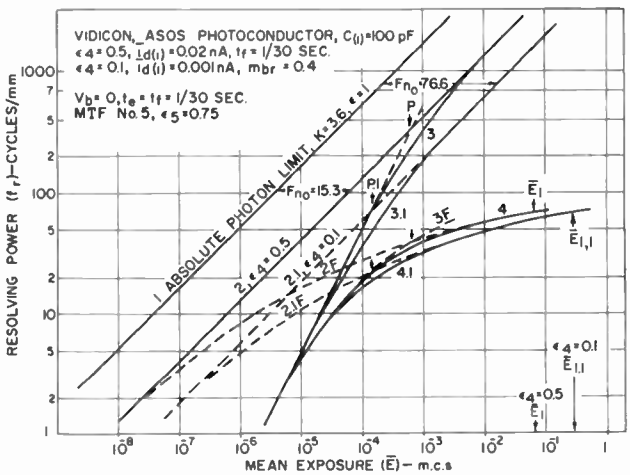

Fig. 15—Quantum limits and resolving power of vidicons, continuous exposure mode.

The resolving power at the maximum exposure $\bar{E}_1$ is $f_r = 68$ cycles per mm. $\bar{E}_1$ is current limited by $i_{s(1)}$ because the potential $V_{st} = 2V_s$ is only 0.67 volt. The functions 3.1 and 4.1 show that a reduction of the photoconductor efficiency (ϵ_4) from 0.5 to 0.1 by a reduction of target voltage (E_T) displaces the high-light section of curves 3 and 4 towards higher exposures. The dark-current limit, however, remains essentially constant because $i_{d(1)}$ is closely proportional to E_T^2.

(c) Intensifier Vidicons

Figure 16 shows the resolving power as a function of mean exposure for an intensifier vidicon, for which the constants are given as in Figure 15, and $|g|_{ph} = 50$. The resolving power function (curve 4) and quantum limits (curves 2 and 3) of the vidicon section are shown for comparison. The factor F_n computed from Equation (49) determines the quantum limit curve 3(I) of the intensifier vidicon. This curve approaches the photoelectron limit $\epsilon = 0.1$ at high exposures.

The MTF of the intensifier vidicon is the product of the MTF of the reading beam (MTF #5 in Figure 12) and the MTF of an image section assumed to have the MTF #3 given in Figure (12). At high exposures the resolving power function 4(I) of the intensifier vidicon crosses curve 4. The maximum resolving power is decreased to $f_r = 45$ cycles per mm at the exposure limit $\bar{E}_{1(I)} = \bar{E}_1/|g|_{ph}$. The low-light resolving power, however, is increased considerably because the steep dark current limit is moved to lower exposures by a factor equaling

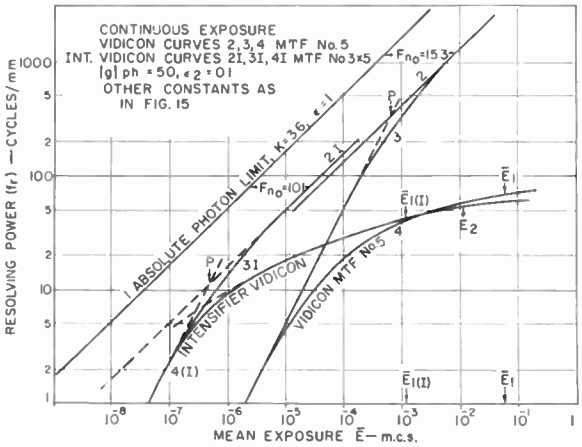

Fig. 16—Quantum limits and resolving power of intensifier vidicons (curves 2I, 3I, 4I) and vidicon (curves 2,3,4).

the photon gain $|g|_{ph}$. Inspection of Equation (49) shows that a reduction of the photoconductor efficiency (ϵ_4) can offset part of the photon gain. Because (ϵ_4) is to a first approximation proportional to the applied photoconductor voltage, and the dark current is proportional to the square of the applied voltage, the exposure range of the intensifier vidicons is controllable to some extent, but its maximum resolving power remains lower because of the reduction by the MTF of the image section. The capacitive lag at low exposure levels is reduced by the increased photoconductor potential (V_{s1}), i.e., the lag at a given exposure $\bar{E}$ of the intensifier vidicon has the same value as the lag of the vidicon (see Equation (24)) at the exposure $\bar{E}|g|_{ph}$.

(d) Resolving-Power Functions for Different Reading Beams

Figure 17 shows the resolving power as a function of mean exposure for the reading beam of a vidicon computed for various values

of MTF. The functions were computed numerically by solving Equations (12) and (14) by computer. The constants are the same as used for Figure 15 except that the mesh transmission is $\tau_m = 0.5$, and $\gamma_4 = \gamma_5 = 0.9$. The auxiliary functions showing the absolute photon limit (curve 1) and the quantum limits (curve 2 and 3) have been added to show the correlation with the graphic solutions. The field-mesh transmission factor τ_m, which determines ϵ_5, was decreased because a finer mesh was required to obtain smaller electron-beam diameters. This decrease is indicated by the corresponding shift of the quantum limit curves (including γ).

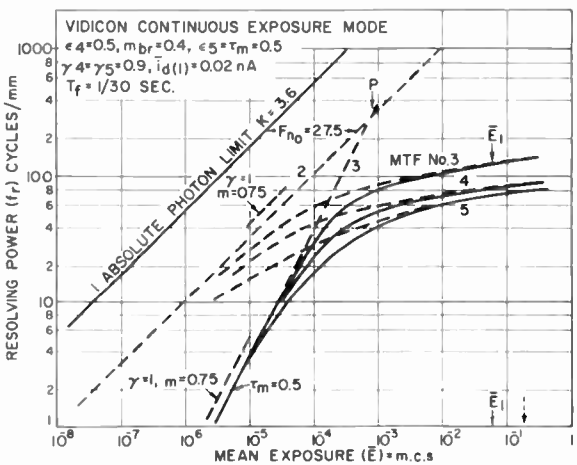

Fig. 17—Resolving power of vidicon for three MTF's of the reading beam.

The solution by computer, which includes all second-order effects, verifies the accuracy of the simplified progressive method of determining the resolving power functions $f_r(\bar{E})$.

It should be noted, however, that as the diameter of the electron beam becomes smaller, the capacitive lag increases because the current scale of the V/i characteristic is multiplied by a factor proportional to the area of the defining aperture.

(e) Variation of Frame Time and Test Object Contrast (Continuous Exposure Readout)

The dark-current charge increases in proportion to the read-out time delay. For low values of F_E, the exposure factor F_n is a linear function of readout delay time (t_d). The displacement of the linear dark-current quantum limit, however, is proportional to the one-half

power of the delay time t_d because the absolute photon limit $f_r(\bar{E}_o)$ is a one-half-power function. This fact is demonstrated in Figure 18 by the family of curves showing resolving power as a function of mean exposure computed for delay times $t_d = t_f$, varying from 1/30 second to 10 seconds and for the MTF #4. The maximum exposure limits are indicated.

As the test object modulation m_o is decreased,* the resolving power functions shift to higher exposures. The linear section of the quantum

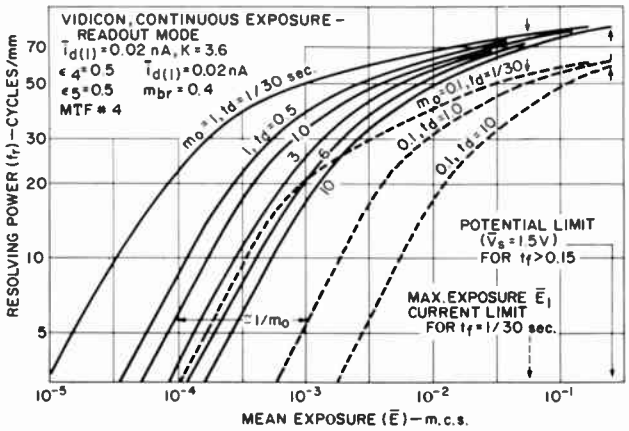

Fig. 18—Resolving power of vidicon for different frame times (t_f).

limit curve (due to dark current) is displaced to higher exposures by the factor $1/m_o$, whereas the exposures of the one-half-power section of the quantum limit are displaced by the factor $1/m_o^2$. The knee (point P in Figure 16) of the composite curve occurs at a lower resolving power. Thus, the complete function containing the MTF correction has a different shape as shown by the broken-line functions in Figure 18, computed for $m_o = 0.1$.

(4) The Low-Light Exposure Limit and the Single-Exposure Erase Mode

At low exposure levels, the resolving power computed for the continuous exposure mode is valid only for stationary test objects in the steady-state condition because the storage surface requires time to build up an equilibrium potential where charge and discharge are equal.

* See Equation (52), (53)

At the maximum exposure $\bar{E}_1$, for example, a signal current $\bar{\imath}_s = 100$ nA develops the potential $V_s = i_s\ (t/C) = 3$ volts for $t/C = 30$ sec/μF. The equilibrium potential $V_r = 3.3$ volt for $i = 100$ nA and $t/C = 30$ can be read from Figure 7a. Thus, equilibrium is reached quickly. When the mean exposure and signal current $\bar{\imath}_s$ are reduced to 1/100 of the above values, the signal potential decreases to $\overline{V}_s = 0.03$ volt. However, the equilibrium potential for $\bar{\imath}_s = 1$ nA, decreases to $V_r = 0.21$ volt, which requires many exposures to build up. The reading beam leaves a large residual potential in the storage surface, $V_r = V_r - V_s = 0.18$ volt. The residual charge CV_r may be a pure signal charge for zero dark current or it may contain a normal percentage of residual dark-current charges. Thus, the signal read out in the equilibrium condition is a normal signal as long as the exposure and the test object position are constant. The test object, however, will blur exceedingly or even become entirely invisible when moved because the signal current read out after a single exposure is only $\bar{\imath}_s = 0.145$ nA, which is equal to one-seventh of the normal signal current. Thus, the useful exposure range for moving objects is shorter than 100:1, even when the exposture time (t_e) is made only a fraction of the frame time necessary to obtain sharp optical images in successive frames.

Hence, the storage surface must be cleared between exposures to prevent double exposures. To shorten the erase time for residual modulation in a single-gun tube, the residual charges in the storage surface are first increased by a uniform-bias light-exposure flash to demodulate the charges. The large charges are then removed (in darkness) by a high-current, defocused beam using a high-speed multiple frame scan, which results in a low total residual potential V_r*. The presence of dark currents requires a low ratio t/C to minimize the dark current equilibrium potential. Figure 10 indicates that the residual potential of a large-area storage surface having a total dark current $\bar{\imath}_d = 50$ nA and a $t/C \leqq 1$ (for a focused read out beam from a 2-mil gun aperture) is $V_{r_d} \simeq 1.25$ volts. Measurements indicate that a defocused beam from the same aperture reduces V_{r_d} by approximately 20%; that is, $V_{r_d} \simeq 1.0$ volt. A high beam current is required to discharge the initially much higher total potential with small t/C ratios.

A control voltage $V_c(t)$ connected in series with the target voltage source is desirable to set and maintain an optimum black-level potential V_o for the read-out beam. The control voltage $V_c(t)$ is the sum of three components, pulse, negative sawtooth, and d-c, each adjustable to maintain a constant optimum black level within the duration of the frame time;

$$V_o = V_r^* + V_d(t) + V_c(t) = \text{constant},$$

The control voltage source is not a stored charge but is generated by a low impedance source and therefore is essentially noise free. Although this control voltage may add to or subtract from the potential of the storage surface V_{st}, as far as the read-out is concerned it does not affect the mean-squared noise of the charges *in* the storage surface; that is, the total particle density from which the modulation factor m_{c4} is computed. Thus, one obtains

$$1/m_{c4} = 1 + (V_r^* + \overline{V}_d)/\overline{V}_s. \tag{54}$$

The bias light exposure occurred during the erase time so that V_r^* contains all residual charges producing noise. The signal charges $\overline{V}_s$ are added during the exposure and, subsequently, as a function of t_d, the dark current charges $\overline{V}_d$, and the control voltage V_c. The potential V_{st} seen by the reading beam is

$$V_{st} = V_s + V_o. \tag{55}$$

The conversion efficiency η_c, which is a function of exposure because an equilibrium potential is not obtained, is computed with Equation (20).

The current ratio $\bar{\imath}/\bar{\imath}_s$ in Equation (33) is determined with the help of Figure 10, where the mean potentials $\overline{V}_{st} = \overline{V}_s + \overline{V}_o$ furnishes $\bar{\imath}$, and the black-level potential $V_{st} = V_o$ determines $\bar{\imath}_o$. The control-voltage component $V_c(t)$ permits adjustment of the black-level potential V_o to any desired value and thus controls the read-out gamma, γ_5, which is otherwise very high at low exposure levels. The operating gamma is determined from a log-log plot of $\bar{\imath}_s = \bar{\imath} - \bar{\imath}_o$ as a function of V_s, as shown in Figure 8.

The signal output in the single-exposure read-out mode is decreased by the remaining charge on the storage surface. At low potentials the signal decreases considerably because of the exponential V/i characteristic of the reading beam. Consequently, the conversion efficiency η_c decreases or, when η_c is made more constant by a black-level bias V_o, the ratio $(\bar{\imath}/\bar{\imath}_s)$ increases. This increase, in turn, reduces the carrier modulation m_{c5} of the reading beam. The loss of signal and consequent increase in F_n is thus controlled by the product $(\bar{\imath}/\bar{\imath}_s)/(\eta_c\gamma_5^2)$, which appears in the last term (for stage 5) of Equations (49), (50), and (51).

The incomplete discharge or capacitive lag is a function of the total capacitance $C = C_{(1)}A$ of the storage surface and the V/i characteristic

of the electron beam. Numerical values depend on the effective beam diameter, which determines the current scale of the V/i characteristic and its derivatives, and on the area of the storage surface. Thus, the resolving-power function is specific for a particular image area and electron gun.

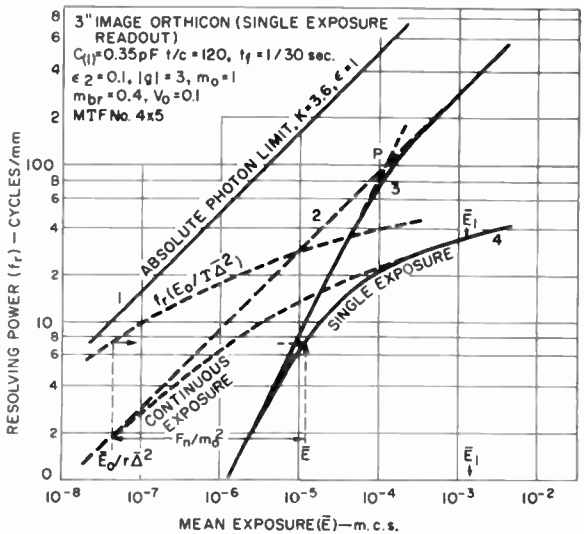

Fig. 19—Resolving power of 3-inch image orthicon, single-exposure readout, $t_f = 1/30$ sec.

(a) Three-Inch Image Orthicon, Single-Exposure Read-Out, ($t_f = 1/30$ second, 2-mil gun aperture)

The total capacitance of the storage surface is $C = 277$ pF ($C_{(1)} = 0.35$ pF). The time-to-capacitance ratio for $t_f = 1/30$ sec is $t_f/C = 120$ sec/μF. For a maximum peak signal potential $V_{s(\max)} = 2.5$ volts, the mean potential for $m_o = 1$ is $\overline{V}_s = 1.25$ volts, for which the maximum $\bar{E}_1$ is computed.

Potentials and currents for calculation of the modulation factors m_{c4} and m_{c5} using Equations (54) and (33) and the conversion efficiency η_c are given in Table V, as a function of the exposure $\bar{E}$. (A somewhat higher black-level potential V_o reduces the read-out gamma.) The absolute photon limit $f_r(\bar{E}_o)$ is shown by curve 1 in Figure 19. The quantum limit $f_r(\bar{E}_o F_n)$ computed in Table V for the single-exposure read-out mode is shown by curve 3. Curve 3 changes in position somewhat for different values of the black level bias $\overline{V}_o$. Similar

Table V—Calculation of F_n for a 3-Inch Image Orthicon, Single-Exposure Readout
($\epsilon_2 = 0.1$, $|g| = 3$, $m_o = 1$, $m_{br} = 0.4$, $t/C = 120$, $V_o = 0.1$)

$\bar{E}$ (meter-candle-seconds)	$V_s + V_o = V_{st}$			$i - i_o = i_s$ (Fig. 7)			η_c	γ	i/i_s	$1/m_{c5}$	F_n
1.22×10^{-3}	1.25	0.1	1.35	10.0	0.265	9.735	0.933	1.2	1.03	5.06	10 + 3.3 + 17 = 30.3
1.22×10^{-4}	0.125	0.1	0.235	0.85	0.265	0.585	0.561	1.3	1.45	6.1	13.3 + 28.5 = 41.8
1.22×10^{-5}	0.0125	0.1	0.1125	0.396	0.265	0.31	0.298	1.3	9.55	26.4	13.3 + 275 = 288.3
6.11×10^{-6}	0.0062	0.1	0.1065	0.28	0.265	0.015	0.288	1.2	18.7	49.3	13.3 + 548 = 571
1.22×10^{-7}	0.0012	0.1	0.1012	0.267	0.265	0.002	0.20	1.1	133.0	335.0	13.3 + 5600 = 5613

Note: All currents are given in nanoamperes; i_o clipped in video amplifier

Table VI—Calculation of F_n for a 4.5-Inch Vidicon, Single-Exposure Readout, $t_f = 4$ sec.
($\epsilon_4 = 0.5$, $m_o = 1$, $m_{br} = 0.3$, $t/C = 10$, $i_d = 50$ nA, $V^*_r = 1.0$, $V_d = 0.25$, $V_o = 1.2$)

$\bar{E}$ (meter-candle-seconds)	$\bar{V}_s + V_o = \bar{V}_{st}$			$\bar{i} - \bar{i}_o = \bar{i}_s$ [Fig. 7]			η_c	γ_5	$1/m_{c4}$	$1/m_{c5}$	F_n
4×10^{-1}	1.5	1.2	2.7	150	28	122	0.81	0.85	1.833	7.4	3.67 + 34 = 37.7
1.2×10^{-1}	0.45	1.2	1.67	62	28	34	0.755	1.1	3.78	9.42	7.6 + 27.7 = 35.3
4×10^{-2}	0.15	1.2	1.35	38	28	10	0.67	1.05	9.35	16.0	18.6 + 58 = 76.6
1.2×10^{-2}	0.045	1.2	1.245	31	28	3.0	0.67	1.0	28.8	37.7	57.5 + 151 = 208.5
4×10^{-3}	0.015	1.2	1.215	29	28	1.0	0.67	0.98	83.5	100.0	167 + 400 = 567
4×10^{-4}	0.0015	1.2	1.202	28.1	28	0.1	0.67	0.98	831.0	1000.0	1670 + 4000 = 5669

Note: All currents are given nanoamperes; i_o clipped in video amplifier

to a dark current limit, the function is linear at low exposures. At high exposures, however, it becomes a one-half power function as shown by curve 2. Curve 2 is located slightly closer to the absolute photon limit than the corresponding curve 2 in Figure 14 for the continuous exposure operation. Thus, *the residual charge due to incomplete discharge in the exponential region of the V/i characteristic introduces the equivalent of a dark-current limit,* that is, a constant noise source.

The extrapolated linear and one-half-power components of the quantum limit curve 3 intersecting at P may be constructed to make the correction for the MTF of the camera or tube as shown in Figure 15 for a vidicon with dark current; however, the value f_r for the function $f_r(\bar{E})$ may be determined more directly by constructing the function $f_r(\bar{E}_a/r\bar{\Delta}^2)$ as outlined for Equation (52).

The MTF used in the example is the combined MTF of curves 4 and 5; that is, the product of curves 4 and 5 of Figure 12. Thus, curve 4 is the resolving power function of a 3-inch image orthicon, with its electron optic operating in the single-exposure read-out mode. The MTF for the example is that obtained with a 1.5- to 2-mil defining aperture in conformance with the V/i characteristic used for obtaining the discharge efficiency.

(b) High-Resolution 4½-Inch Vidicon, Single-Exposure Read-Out

The image area of the photoconductor is 2500 mm². For $C_{(1)} = 160$ pF and a slow-scan read-out time $t_f = 4$ sec, one obtains $t/C = 10$ sec/μF. For a total dark current $\bar{\imath}_d = 50$ nA, and a delay time $t_d = t_f/2 = 2$ at the center of the image, the potential resulting from dark-current charges is $\bar{V}_d = 0.25$ volt.

It is assumed further that a defocused beam with a fast erase scan discharges the storage surface to the dark current equilibrium potential $V_r^* = 1$ volt, resulting in $1/m_{c4} = 1 + (1.25/\bar{V}_s)$. Given the constants $m_o = 1$, $m_{br} = 0.3$, one obtains further $1/m_{c5} = 3.33\ (1 + \bar{\imath}/\bar{\imath}_s)$. Table VI lists currents and potentials for calculating the exposure factor F_n using Equation (51).

Figure 20 shows the quantum limit curves 1, 2, and 3a. The resolving-power function (curve 4a) includes the correction for the beam MTF #5, to conform with the current scale of the V/i characteristics that were used in Figure 10 to calculate F_n. The maximum peak white exposure is limited to $2\bar{E}_{1a} = 3$ volts, which is roughly one decade higher than the limit for the continuous-exposure read out at $t_f = 1/30$ second, also shown for comparison.

A second example may illustrate the effect of reducing the area of

the photoconductor by a factor of 20, which is approximately the difference in the image surfaces of a 4.5-inch and a 1-inch vidicon. The corresponding reduction in total capacitance increases the ratio t/C to 200 sec $/\mu$F for the same frame time and reduces the currents considerably as shown by the data in Table VII.

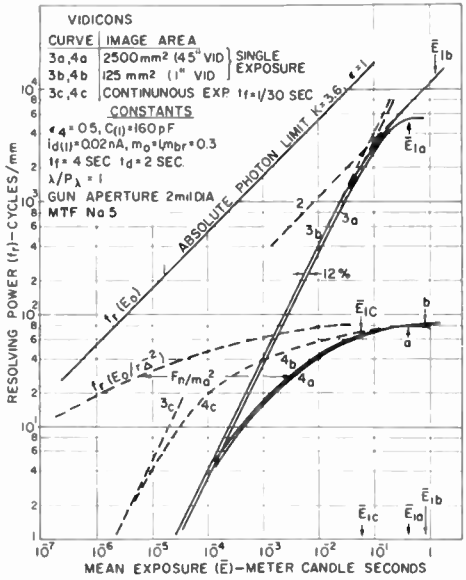

Fig. 20—Resolving power of 1-inch and 4.5-inch vidicon, single-exposure readout $t_f = 4$ sec.

The exposure range of the 1-inch tube is extended by a factor of 2 into the high-light range, but the low-light exposure limit is lowered only 12%, as shown by the quantum limit curve 3b and the resolving power function 4b in Figure 20. For zero dark current ($V_d = 0$), the constant noise quantum limit is determined by the residual potential V_r* from the erase scan (V_r* is a function of t/C), the exponential V/i characteristic, and the diameter of the reading beam. The quantum limit curves 3a and 3b in Figure 20 are approximately one decade higher than the low dark-current limit of the continuous-exposure mode at $t_f = 1/30$ second. This dark current limit curve is shown for comparison by curve 3c, for which the conversion efficiency is unity.

Comparison of Equations (51) and (49) indicates that the addition of an intensifier section decreases the value of the terms for stage 4 and 5 by the photon gain $|g|_{ph}$. In combination with the reduction of

all exposures by $|g|_{ph}$, the linear section of curve 3a or 3b is displaced towards lower exposures by the factor $|g|_{ph}$ as illustrated in Figure 21 for three different MTF combinations. The maximum exposure is current limited by the current density of the reading beam. The smaller peak currents, i_s, obtained from small gun apertures, decrease the maximum exposure as indicated by the values $\bar{E}_2$ and $\bar{E}_3$ in Figure 21. An image-intensifier section is very effective in restoring low-light sensitivity for the single-exposure read-out mode.

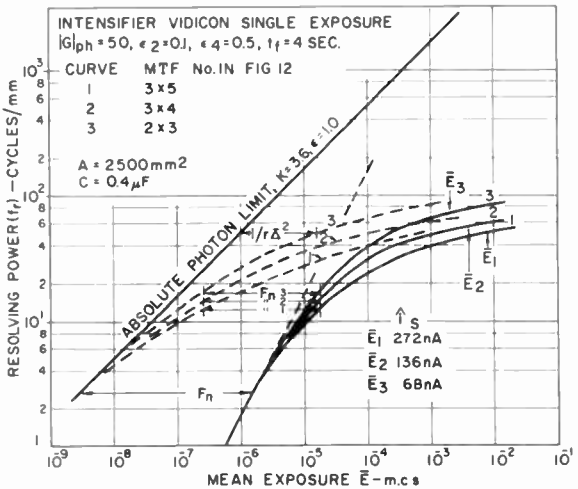

Fig. 21—Exposure range and resolving power in a single image for two high light exposures (E_{max}) of a 1-inch vidicon.

(5) Resolving Power and Exposure Range of a Single Image

When the return-beam modulation factor m_{br} remains constant for all potentials in the charge image, the functions $f_r(\bar{E})$ are identical to the functions computed for separate exposures (Figures 14 through 20). This is not the case when the signal is read out as a return-beam modulation because the beam current I_b' approaching the storage surface has a constant value adjusted for the maximum charge level. Therefore, the return-beam modulation factor (m_{br}) decreases by the factor ($\bar{i}/\bar{i}_{max}$) when reading out lower potentials in the charge image (see Equation (18)). The last term in the equation for computing F_n increases therefore by the ratio ($\bar{i}_{max}/\bar{i}$) as shown by the values in Table VIII computed for a 1-inch vidicon and two values of high-light exposure in the single-exposure read-out mode.

Table VII—Calculation of F_n for a 1-Inch Vidicon, Single-Exposure Readout $t_f = 4$ sec.
($\epsilon = 0.5$, $m_o = 1$, $m_{br} = 0.3$, $t/C = 200$, $i_d = 2.5$nA, $V^*_r = 0.34$, $V_d = 0.25$)

$\bar{E}$ (meter-candle-seconds)	$\overline{V}_s + V_o = \overline{V}_{st}$			$\overline{i} - \overline{i}_o = \overline{i}_s$			η_c	γ_v	$1/m_{c1}$	$1/m_{c5}$	F_n
1.6	6.0	0.5	6.5	30.00	1.88	28.12	.93	0.95	1.1	6.8	2.2 + 21.0 = 23.2
8×10^{-1}	3.0	0.5	3.5	17.20	1.88	15.32	1.02	0.98	1.2	7.1	2.4 + 19.3 = 21.7
4×10^{-1}	1.5	0.5	2.0	9.40	1.88	7.52	1.0	1.0	1.4	7.5	2.8 + 20.0 = 22.8
1.2×10^{-1}	0.45	0.5	0.95	4.10	1.88	2.22	0.985	1.0	2.3	9.4	4.6 + 25.5 = 30.1
4×10^{-2}	0.15	0.5	0.65	2.61	1.88	0.73	0.975	1.0	5.0	15.2	10 + 42 = 52
1.2×10^{-2}	0.045	0.5	0.545	2.10	1.88	0.22	0.975	1.0	14.0	35.0	28 + 96 = 124
4×10^{-3}	0.015	0.5	0.515	1.95	1.88	0.07	0.932	1.0	40.0	96.0	80 + 274 = 354
4×10^{-4}	0.0015	0.5	0.5015	1.887	1.88	0.007	0.93	1.0	396.0	900.0	800 + 2600 = 3400

Note: i_o clipped in video amplifier

Table VIII—Calculation of F_n for a 1-Inch Vidicon, Single-Exposure Readout, for the Functions $f_r(\bar{E})$ of a Charge Image (Constants as in Table VII)

$\bar{E}$ (meter-candle-seconds)	Charge Image Value F_n	Charge Image Value F_n	Separate Exp. Value F_n
1.6	2.2 + 21 = 23.2		2.2 + 21.0 = 23.2
8×10^{-1}	2.4 + 33.5 = 35.9		2.4 + 19.3 = 21.7
4×10^{-1}	2.8 + 62.5 = 65.3		2.8 + 20.0 = 22.8
1.2×10^{-1}	4.6 + 186 = 190.6	4.6 + 25.5 = 30.1	4.6 + 25.5 = 30.1
4×10^{-2}	10 + 483 = 493	10.0 + 66 = 76.0	10.0 + 42 = 52
1.2×10^{-2}	28 + 1370 = 1398	28.0 + 188 = 216	28 + 96 = 124
4×10^{-3}	80 + 3300 = 3380	80 + 450 = 530	80 + 274 = 354
4×10^{-4}	300 + 41500 = 42300	800 + 5650 = 6450	800 + 2600 = 3400

The factor F_n for separate exposures is given for comparison. Figure 22 shows quantum limits (curves 3.1 and 3.2) and the resolving-power range (curves 4.1 and 4.2) for the two exposure limits $\bar{E}_{\max 1}$ and $\bar{E}_{\max 2}$. The low-light resolving power for the exposure $\bar{E}_{\max 1}$ when compared with independent exposures (curve 4), is moved to higher exposures by the factor $(42300/3400)^{1/2} = 3.5$. The difference de-

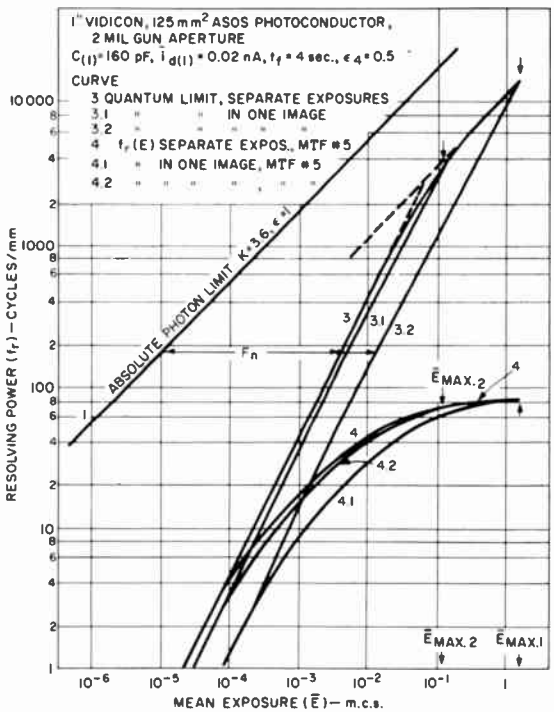

Fig. 22—Resolving power of 4.5-inch vidicon camera (without aperture correction).

creases as $\bar{E}_{\max}$ is reduced. At very low light levels, curve 4.2 for the exposure $\bar{E}_{\max 2}$ requires only 1.38 times the exposure of curve 4 because the beam modulation factor m_b becomes constant again at low signal potentials where $\bar{\imath}$ is made substantially constant by the black-level potential $\overline{V}_o$ (see Table VII).

Therefore, at moderate and low exposures, where the signal component $\overline{V}_s$ is normally a small fraction of the total potential, the reduction in exposure range caused by a constant beam current is insignificant. The comparatively high black-level potential V_o is instrumental in improving the conversion efficiency.

VI—Experimental Verification

Resolving-power tests were made on 4.5-inch multiplier vidicons and image orthicons in a precision camera containing the new high-resolution electron optic. The MTF of the camera lens (curve 1 in Figure 12) and the MTF's (curves 3 and 4) of reading beams were measured in this camera in the continuous-exposure mode by scanning a 10×10 mm area having a scanning line density of 100 to 200 lines/mm, 2:1 interlaced at 15 to 30 frames per second. The video system has a flat response over a 60 MHz pass band and can be reduced to 40, 30, 20, 15, 10, 6, or 4 MHz by phase-corrected filters.

The resolving power for vidicons observed visually on a high-definition monitor (6,000 lines resolution) ranged from 50 to 80 cycles/mm, depending on the electron gun.

The photographs in Figure 23 were taken with a double-frame exposure from a 4.5-inch vidicon having a 1.5-mil gun aperture. The resolving power in the photographs is $f_r \simeq 54$ cycles/mm. The computed resolving power without lens is 68 cycles/mm (see Figure 15), which is reduced by the camera lens to $f_r = 60$ cycles/mm.

The photograph in Figure 23b demonstrates the enhanced contrast through aperture correction that compensates for the decreasing response of the monitor kinescope and photographic system.

The photographs in Figures 24 and 25 were taken from an experimental 4.5-inch image orthicon operated with a 2.5-volt potential on a standard glass target, a standard electron gun, a field mesh of 29 cycles/mm, and a target mesh of 39 cycles/mm. The image section was operated at 2.4 kV. The resolution in the 10×10 mm test area is clearly limited by the 39 cycle/mm target mesh, which is shadow-imaged by the image section electrons without the MTF loss in the image section and camera lens. The test bar resolving power is $f_r \simeq 30$ cycles per mm. The resolving power computed for the MTF combination $1 \times 4 \times 5$ has practically the same value (see Figure 14). The product of the MTF's $1 \times 4 \times 5$ is 61% at 10 cycles/mm (the lens operated at 1.6 times the frequency because of the image magnification in this tube). The measured sine-wave response of the camera was 50% at 10 cycles/mm.

The photographs in Figures 26 and 27 were taken with a 4.5-inch vidicon having a one-mil gun aperture, a 39 cycle/mm field mesh and the MTF (curve 4) as shown in Figure 12. The signal current had the value $\hat{\imath}_s = 50$ nA. The resolving power in Figure 25 is $f_r \geqq 68$ cycles/mm and in Figure 27 (which is direct reading in television lines/mm) $f_r \simeq 75$ cycles/mm. The computed resolving power without lens is 78

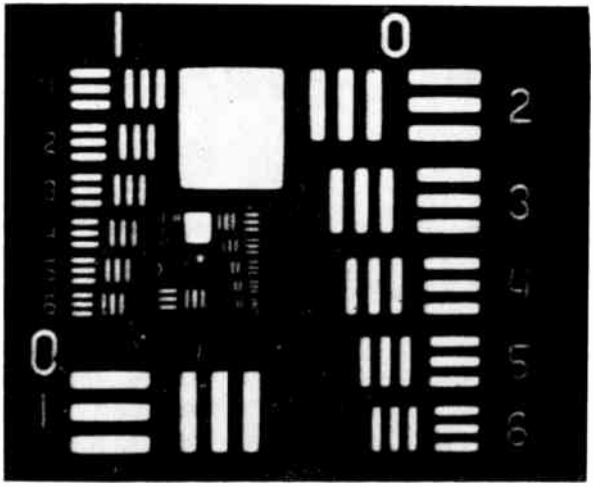

(a)

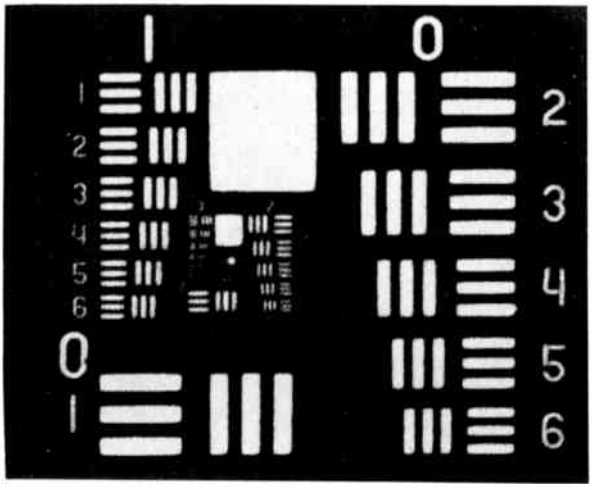

(b)

Fig. 23—Resolving power of 4.5-inch vidicon camera, *f*/5.6 lens, standard 1.5-mil aperture gun, double-frame exposure: (a) without aperture correction, (b) with 4 × aperture correction in scanning direction.

Test Chart Frequencies in Cycles/mm

No. 2.1 to 2.6, respectively:	24	26.9	30	33.7	37	42.6
No. 3.1 to 3.6, respectively:	48	54	60.5	68	76	85

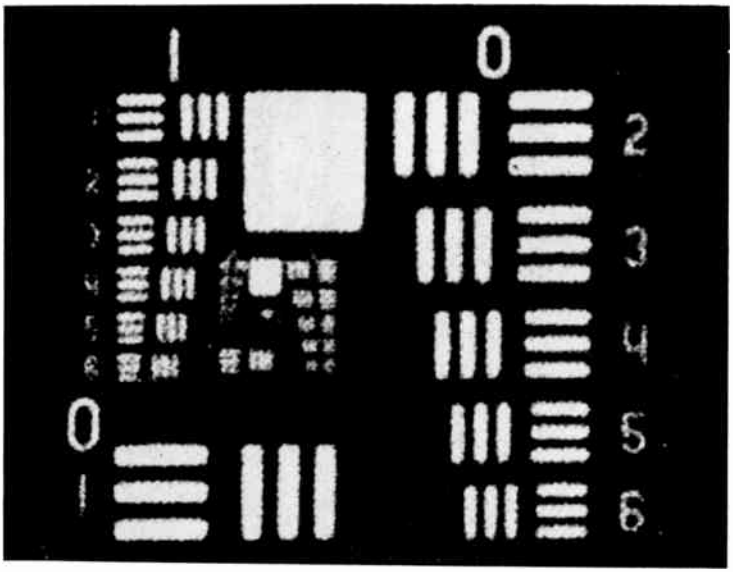

Fig. 24—Resolving power of 4.5-inch high-resolution image orthicon camera *f*/5.6 lens, experimental tube, double frame exposure. (Electron image magnification 1.6, scanning line density 100/mm.)

Test Chart Frequencies in Cycles/mm at Glass Target

No. 1.1 to 1.6, respectively:	12	13.4	15	17	18.5	21.3
No. 2.1 to 2.6, respectively:	24	26.9	30	33.7	37	42.6

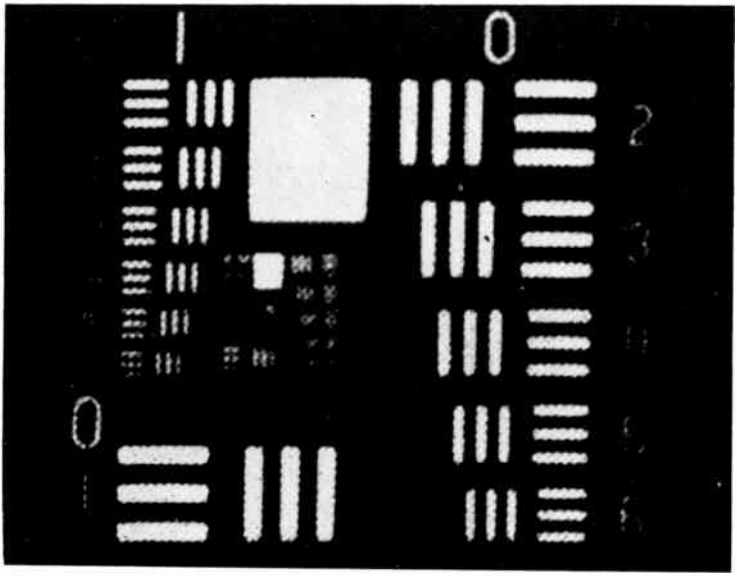

Fig. 25—Resolving power of 1.5-inch high-resolution image orthicon camera lens, 15-frame exposure. Test chart as in Figure 24, target mesh = 39 cycles/mm.

cycles/mm (see Figure 17), which is reduced by the lens to $f_r = 70$ cycles/mm. ($1/\bar{r}_L^2 = 4 = 0.6$ log units of $\bar{E}$ in Figure 17). Thus, the observed values agree well with the computed resolving power.

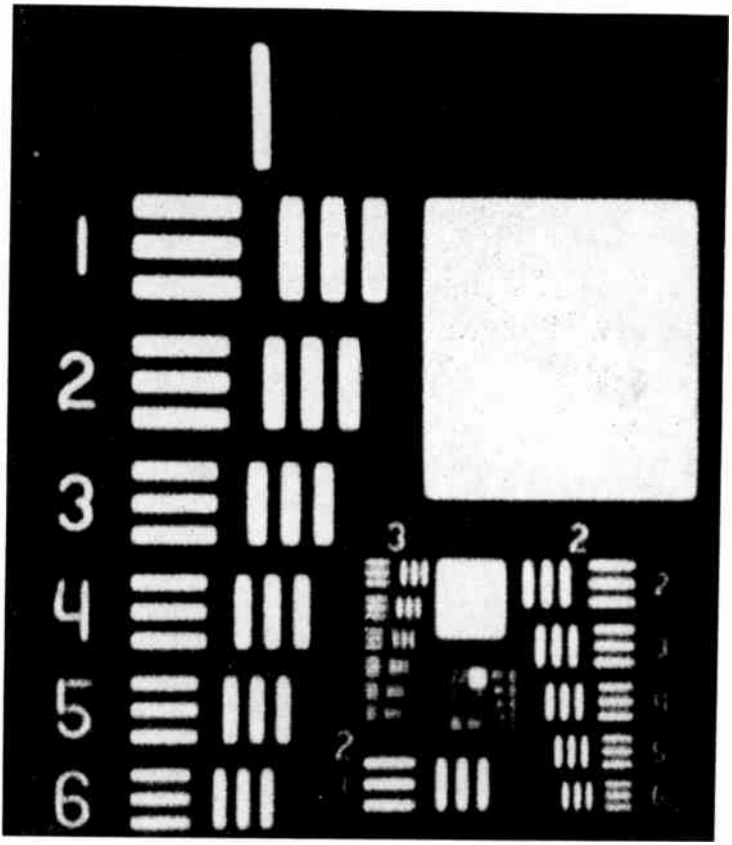

Fig. 26—Resolving power of 4.5-inch vidicon having the sine-wave response shown by curve 4 of Figure 12. Test chart frequencies in cycles/mm: No. 3.1 to 3.6, respectively, 48, 54, 60.6, 68, 76, 85.5.

VII—Conclusion

The resolving-power functions $f_r(\bar{E}, m_c)$ are a powerful tool in the analysis and appraisal of imaging systems. The numerical evaluation points out that high resolving powers require a high photon input and a high storage capacitance to increase the quantum limit. The realizable resolving power of television cameras is far smaller than the

quantum limit of the storage surface because of the large degradation of the image modulation (m_o) by the MTF's of the system. When compared with a photographic camera, the storage surface of a television camera has a considerably higher quantum efficiency. Photo-

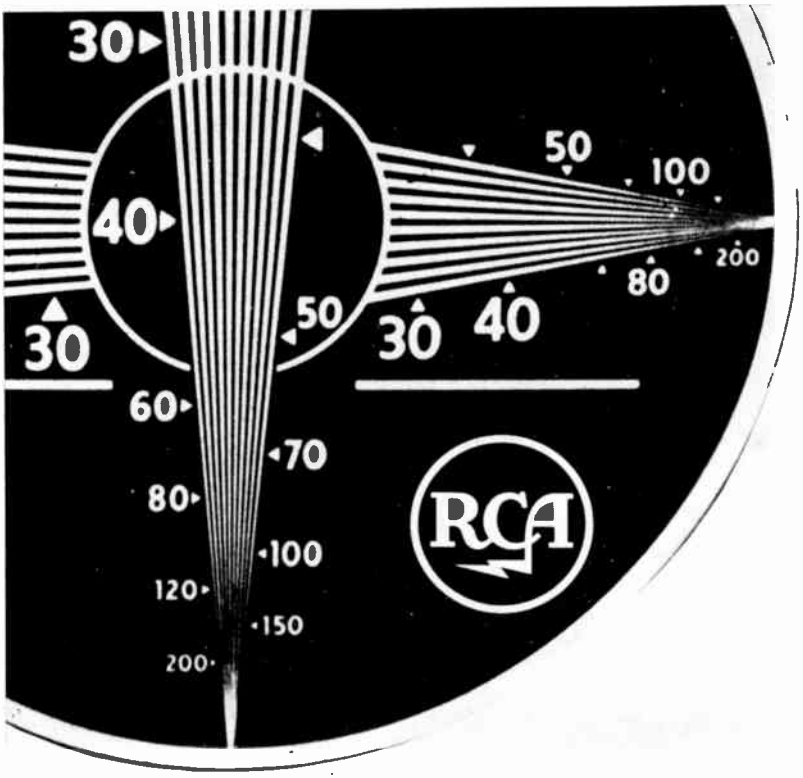

Fig. 27—Resolving power of 4.5-inch vidicon having the sinewave response shown by curve 4 of Figure 12.

conductors, in particular, can store higher particle densities and have higher resolving powers than the best photographic emulsions.

On the other hand, the signal in a photographic emulsion can be read out with less degradation by the MTF of a microscope objective than by the MTF of an electron beam in the sequential read out. The *maximum* realizable resolving power of the photographic camera may

be higher as shown by Figure 28, which compares the resolving power of a vidicon camera (standard electron gun) with various photographic cameras using identical f/5.6 camera lenses. When the influence of the MTF is decreased by reducing the modulation (m_o) of the input signal, the resolving power of the television camera exceeds the resolving power of the photographic camera because of the higher quantum efficiency and particle density in its storage surface. The vidicon exposure is roughly equal to that of Panatomic-X films.

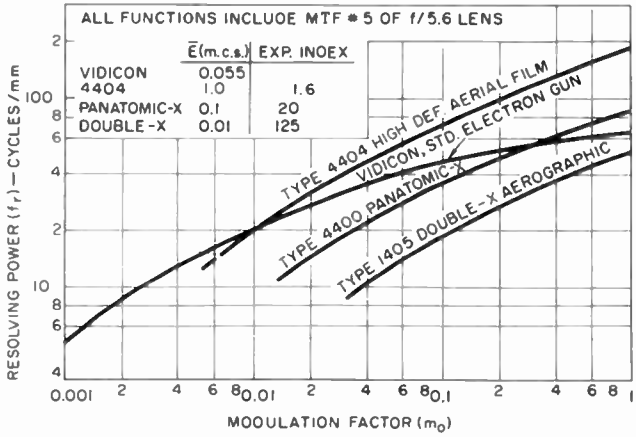

Fig. 28—The resolving power of photographic cameras and a vidicon camera using an identical $f/5.6$ camera lens.

Excess particle densities injected by dark currents or other sources ("fog" in photographic emulsions) reduce the low-light quantum limit. Dark-current charges in photoconductors decrease the low-light exposure limit considerably in the continuous-exposure mode, but have less effect in the single-exposure read-out mode. This mode is limited basically by the increasing beam resistance and decreasing conversion efficiency (η_c) of the reading beam in the exponential region of its V/i characteristic. The resolving power can be optimized at a given exposure level by selection of an appropriate beam diameter (not current density!). This is somewhat analogous to a change of grain size in photographic emulsions.

The low-light resolving power of the continuous-exposure mode is valid only for stationary objects, because the high conversion efficiency ($\eta_c = 1$) of this operating mode depends on the establishment of an equilibrium potential. This potential, however, requires a build-up or transient time, which increases to large values at low exposures because

of increased beam resistance. This capacitive time lag* is eliminated in the single-exposure erase mode; thus, sharp single-frame images are produced at the cost of a higher low-light exposure limit. The low-light limitation can be removed by preamplification in an image intensifier section preceding the storage surface. This method is very effective with photoconductors.

Finally, it is shown that for a return-beam read out the resolving power in the exposure range of a single image is reduced below that of independent exposures by the square root of the relative beam current modulation (m_b). The reduction is in the order of one half decade (out of four decades) for a vidicon at maximum exposure. It decreases to insignificant values at medium and low exposures because the constant black-level potential (V_o) becomes instrumental for optimum operation.

The electron beam read out of stored charges in this analysis is based on the condition that the storage capacitance is homogenous, without dielectric lag.

Acknowledgment

The development of high-definition electron optics and camera tubes used for experimental verification of computed resolving powers was sponsored by the Air Force Avionics Laboratories, Wright Patterson Air Force Base, Ohio (Contract AF 33 (615)-2109). In addition the writer has had helpful discussions on the subject of photosensitivity and noise in radiation converters with R. W. Engstrom (RCA Lancaster), A. D. Cope, G. A. Morton, D. D. North, and A. Rose of the David Sarnoff Research Center, Princeton.

Appendix—Units and Conversions

Photographic Units

The *optical net density* D of photographic emulsions is related to the light transmittance T of the film by $D = -\log(T/T_{base})$

The *rms granularity* $\sigma(D)$ of an emulsion is the rms deviation in density computed from the relation

$$\sigma(D) = 0.4343/|R|_T.$$

* The photoconductive lag is insignificant compared to the capacitive lag in all practical storage surfaces.

where $|R|_T = T/\sigma_T$ = absolute signal-to-noise ratio in transmittance

T is the gross light transmittance of film

σ_T is the measured rms "noise" = rms deviation in transmittance.

The rms granularity $\sigma(D)$ given by the Eastman Kodak Co. is measured by scanning a density $D = 1$ with an aperture 24 microns in diameter, which corresponds to a sampling area $\bar{a} = (.024/1.08)^2 = (0.0222 \text{ mm})^2$. The unit value $|R|_{(1)}$ used in resolving-power calculations is therefore, for $D = 1$,

$$|R|_{(1)} = 0.4343/\sigma_D \ (0.0222) = 19.5 \ \sigma_D$$

The maximum, resolving power is obtained when the product $(R)_{(1)}\gamma$ in Equation (8) is a maximum. This occurs generally at a density D' somewhat below the point, where the function D (log E) becomes a straight line, and D' may have a value less than unity. The value $|R|_{T(1)}$ for this density D' can be approximated for most cases by $(R)_{T(1)} = (R)_{T(1)}/(D')^{0.45}$. The film density $(D)_1$ and hence the values obtained for γ and $|R|_{(1)}$, are functions of the light absorption modulation of the photon carrier beam used in the image-transfer process, the beam diffusion by the grain structure, and the solid angle of radiation selected and transferred in the optical coupling (lens or contact) to the next stage or the eye. The transferred density measured with diffuse light may thus be considerably lower than the transferred density measured with "specular" light (Callier effect), particularly for thick grain layers. Resolving power tests of photographic emulsions are made with microscopes under the most favorable specular lighting conditions yielding maximum microdensity contrast, whereas sensitometric data are taken under entirely different conditions giving diffuse densities. As a result, the values $|R|_{(1)}\gamma$ and the resolving power computed from these data may be considerably lower than the rated resolving power of the film type, particularly when the emulsion has a high diffusion factor. The discrepancy is caused by improper data and does not indicate a failure of the principle.

Television Units

Signals and noise are observed as electron currents. A current of 1 nanoampere represents a flow of 6.25×10^9 electrons per second. The current density $i_{(1)}$ flowing to or from one square millimeter of a photomitting or conducting surface may thus be converted to a particle

or charge density $\bar{n}_{(1)}$ per unit area by means of the following:

$$\bar{n}_{(1)} = 6.25 \times 10^9 \, i_{(1)} \, T, \tag{56}$$

where $i_{(1)} = I/A$ = photocurrent density in nA/mm^2,

I is the total current, A = surface area in mm^2

T is the exposure or discharge time in seconds.

Sampling Area and Equivalent Pass Band

A noise-equivalent pass band is, by definition, a temporal or spatial frequency spectrum $\Delta f_{(e)}$ of constant amplitude passing the same mean-squared noise as the actual system spectrum.[2] It is computed from the sine-wave response function of the actual system;

$$\Delta f_{(e)} = \int_0^{f_c} (\bar{r}_1 \, \bar{r}_2 \ldots \bar{r}_n)^2_f \, df, \tag{57}$$

where $(\bar{r}_1 \, \bar{r}_2 \ldots \bar{r}_n)_f$ is the product of sine-wave response factors of the system elements as a function of frequency (f), and f_c is the cutoff frequency. The equivalent pass band may be expressed in half cycles by the television line number;

$$N_{(e)} = 2 \, \Delta f_{(e)}. \tag{58}$$

A two-dimensional aperture or sampling area can be described by its pass bands in the X and Y directions of scanning. The X and Y dimensions and the area $\bar{a}$ of a rectangular aperture are related to its equivalent pass bands as follows:

$$X = 1/N_{e(X)}, \; Y = 1/N_{e(Y)},$$

$$\text{and } \bar{a} = XY = 1/N_{e(X)} \, N_{e(Y)} = 1/\bar{N}_e^2, \tag{59}$$

where $\bar{N}_e = [N_{e(X)} \, N_{e(Y)}]^{1/2}$ is the equivalent pass band of a square aperture of equal area.

It follows that the equivalent sampling area $\bar{a}$ of a system stage or a system can be computed from its frequency spectrum with Equations (57) and (59). The diameter δ of a circular scanning aperture (used in film noise measurements) is given by $\delta = 1.08/N_e$.

Electrical Frequency Band Δf and Raster Line Density

The electrical pass band in cycles per second is given by

$$\Delta f = 2bAf_r^2/t_f, \tag{60}$$

where A is the image area in mm^2,

$b = t_f/t_{f\,(\text{unblanked})}$ is the blanking factor (generally $b = 1.23$),

t_f is the frame time in seconds,

f_r is the resolving power in cycles/mm.

The factor 2 appears because a minimum of two raster lines (samples) is required in the y direction to reproduce one cycle of resolving power f_r. The television line number for a square image ($X = Y$) is given by

$$N = 2f_r\sqrt{A}. \tag{61}$$

The raster line density $N_{r(1)}$ should be limited to the following values:

$$2f_r \leq N_{r(1)} \geq 0.4\,f_{r(\max)} \tag{62}$$

per mm of the vertical (Y) dimension of the camera tube image. The value $N_{r(1)} = 2f_r$ is generally satisfactory when the sine-wave response factor $\bar{r}_{\text{syst}}$ of the camera system has a small value at f_r. When f_r is limited by a low-light exposure or by the electrical frequency channel, the raster line density should not be reduced below the value $N_{r(1)} \simeq 0.4f_{r(\max)}$ to avoid undischarged interline area, unless the Y-dimension of the scanning beam is increased by vertical spot wobble.

Exposure and Photon Density

The radiant energy incident on a photosensitive surface during the exposure time is specified by the exposure E in meter-candle-seconds. The *mean exposure level* can be computed from the incident photon density $\bar{n}_{s(1)1}$;

$$\bar{E} = \bar{n}_{s(1)1}/[7.5 \times 10^9(\lambda/P_\lambda)] \tag{63}$$

The *peak white exposure* has the value $E_{\max} = 2\bar{E}$ for $m_o = 1$, where $\bar{E}$ or $E_{\max}$ is the exposure in meter-candle-seconds (lumens per square meter).

The factor (λ/P_λ) is a function of the spectral sensitivity of the surface and the relative energy distribution of the illuminant.[1] The following table gives some values for sunlight (5000°K, illuminant B):

Photosensitive Surface	λ	λ/P_λ
Panatomic-X film	0.400	0.56
Type 4404 film (high definition)	0.550	1.3
Uniform spectral sensitivity from $\lambda = 0.4$ to $\lambda = 0.7$	0.550	1.57
Spectral sensitivity-luminosity function	0.550	1.0

The test pattern brightness B_{max} in candles per square foot can be computed with $B_{max} \simeq 0.42\, E_{max}\, (F_{number})^2/T_e$.

Peak-to-Peak Signal to RMS Noise Ratio (SNR)

The SNR of a television camera is by definition the ratio of the maximum signal of a square-wave test object of zero frequency and modulation, $m_o = 1$, to the rms noise in a specified frequency channel Δf. Given the sine-wave response function $\bar{r}(f)$ of the camera and its resolving power f_r cycles/mm, the SNR can be computed from the relation

$$\mathrm{SNR}_{fr} = |R|/[0.81\, \bar{r}_{fr} m_o\, (5/S_{s(fr)})^{1/2}] \tag{64}$$

where the subscript fr specifies that these terms must be evaluated for the resolving-power frequency. The spread factor $S_{s(fr)}$ is computed with Equation (40).

Example: Given $f_r = 90$ cycles/mm for $m_o = 1$ for the threshold value $|R| = 3.6$. It will be assumed that the sine-wave response function furnishes the values $\bar{r}_{90} = 0.04$ and $S_{s(90)} = 1.38$. The SNR computed with Equation (64) has then the value $\mathrm{SNR}_{90} = 58.8$. Assuming further a storage surface of 25×25 mm^2, a frame time $t_f = 4$ seconds, and blanking factor $b = 1.2$, the video frequency channel computed with Equation (60) would have the pass band

$$\Delta f_{90} = 3.03 \text{ MHz}.$$

The resolving power of a camera can be determined from the measured SNR and MTF as follows. Compute the resolving power $f_{r(e)}$ of

the electrical system with Equation (60). The value SNR_f can then be plotted as a function of f from the relation $SNR_f = SNR_m f_{r(e)}/f$. The intersection of this function with that of Equation (64) computed for several frequencies yields the resolving power of the system.

References

1. Otto H. Schade, Sr., "An Evaluation of Photographic Image Quality and Resolving Power," *Jour. SMPTE*, Vol. 73, p. 81, Feb. 1964.
2. Otto H. Schade, Sr., "Image Graduation, Graininess and Sharpness in Television and Motion Picture Systems, Part III and IV," *Jour. SMPTE*, Vol. 61, p. 97, Aug. 1953, and Vol. 64, p. 593, Nov. 1955.
3. Otto H. Schade, Sr., "A 60-Megacycle Video Chain for High-definition Television Systems," *RCA Review*, Vol. XXVI, No. 2, June 1965.
4. A. Rose, "Television Pickup Tubes and the Problem of Vision," *Advances in Electronics*, Vol. I, 1948.

RCA Technical Papers

Second Quarter, 1967

Any request for copies of papers listed herein should be addressed to the publication to which credited.

"An AC/DC Line-Operated Transistorized TV Receiver," C. F. Wheatley, *Trans. IEEE PTGBTR* (April) 1967

"Acoustoelectric Current Saturation in CdS as a Fluctuation Process," A. R. Moore, *Jour. Appl. Phys.* (April) 1967

"Additional Considerations in Comb-Line Bandpass Filter Interstage Couplings," R. M. Kurzrok, *Trans. IEEE PTGMTT* (Correspondence) (April) 1967

"Analysis of Electron Current Extration from Synthesized Plasmas," H. Sobol and A. L. Eichenbaum, *Jour. Appl. Phys.* (April) 1967

"Characteristics of Microstrip Transmission Lines," H. R. Kaupp, *Trans. IEEE PTGEC* (April) 1967

"Characteristics of Waveguide Resonant-Iris Filters," T. S. Chen, *Trans. IEEE PTGMTT* (Correspondence) (April) 1967

"A Comparison of Solid-State and Electron-Tube Devices for TV-Receiver RF and IF Stages," L. S. Baar and S. Reich, *Trans. IEEE PTGBTR* (April) 1967

"Correction to 'Enumeration of Seven-Argument Threshold Functions'," R. O. Winder, *Trans. IEEE PTGEC* (Correspondence) (April) 1967

"An Ergodic Theorem and Its Generalization," A. A. Wolf, *Jour. Frank. Inst.* (April) 1967

"Four Tube, Separate Luminance Color Television Camera," C. J. Hirsch, *Broadcast News* (April) 1967

"High-Frequency Transistor Evaluation by Three-Port Scattering Parameters," A. P. Anderson, *Trans. IEEE PTGMTT* (Correspondence) (April) 1967

"High-Power, High-Efficiency Silicon Avalanche Diodes at Ultra High Frequencies," H. J. Prager, K. K. N. Chang, and S. Weisbrod, *Proc. IEEE* (Letters) (April) 1967

"Maintaining Modern TV Transmitter Performance," D. W. Sargent, *Broadcast News* (April) 1967

"Multiplexing Land-Mobile Base Station Signals on the Carrier of an FM Broadcast Station," W. L. Behrend, *Trans. IEEE PTGBC* (April) 1967

"A New Video and Noise-Immune-Sync Tube and Circuit," T. E. Deegan and E. F. Kashork, *Trans. IEEE PTGBTR* (April).. 1967

"Theory of Infrared Optical Properties of Fluorite Crystals," W. Zernik, *Revs. Mod. Phys.* (April) 1967

"Thermally Engraved Gratings Using a Giant-Pulse Laser," H. J. Gerritsen and M. E. Heller, *Jour. Appl. Phys.* (April) 1967

"A Unified Design Chart for Small VSWR Filters," N. K. M. Chitre and M. V. O'Donovan, *Microwave Jour.* (April) 1967

"The Use of Mobile Radio in On-the-Spot News Coverage," N. C. Colby, *Trans. IEEE PTGBC* (April) 1967

"Note on Transient Current Measurements in Liquid Crystals and Related Systems," G. H. Heilmeier and P. M. Heyman, *Phys. Rev. Letters* (10 April) 1967

"Taking Cryoelectric Memories Out of Cold Storage," R. A. Gange, *Electronics* (April 17) 1967
"All-Garnet-Substrate Microstrip Circulators," B. Hershenov, *Proc. IEEE* (Letters) (May) 1967
"Effects of Magnetic Field on Pulse and CW Operation of the Large Bore Ionized Gas Laser," S. A. Ahmed, T. J. Faith, and G. W. Hoffman, *Proc. IEEE* (Letters) (May) 1967
"GaAs Avalanche Microwave Oscillator with 1-Watt Power Output," S. G. Liu, *Proc. IEEE* (Letters) (May) 1967
"Linear Electro-Optic Effect in Ferroelectric KTN," J. A. van Raalte, *Jour. Opt. Soc. Amer.* (May) 1967
"Mechanically Variable Acoustic Surface-Wave Delay Line with a Noncontacting Transducer," C. P. Wen, R. F. Mayo, and P. Schnitzler, *Jour. Acous. Soc. Amer.* (Letters to the Editor) (May) 1967
"Modulation of Infrared Light by Holes in Pulse-Ionized GaAs," P. D. Southgate, H. J. Prager, and K. K. N. Chang, *Jour. Appl. Phys.* (Communications) (May) 1967
"MOS Transistors with Anodically Formed Metal Oxides as Gate Insulators," W. Witt, F. Huber, and P. Delivorias, *Proc. IEEE* (Letters) (May) 1966
"Two-Stream Instability in Semiconductor Plasmas," B. B. Robinson and G. A. Swartz, *Jour. Appl. Phys.* (May) 1967
"Energy Levels and Spectra of Ho^{2+} in CaF_2, SrF_2, BaF_2, and $SrCl_2$," H. A. Weakliem and Z. J. Kiss, *Phys. Rev.* (10 May) 1967
"Far-Infrared Optical Properties of CaF_2, SrF_2, BaF_2, and CdF_2," D. R. Bosomworth, *Phys. Rev.* (15 May) 1967
"Critical Magnetic Fields of Granular Superconductors," B. Abeles, R. W. Cohen, and W. R. Stowell, *Phys. Rev. Letters* (22 May) 1967
"Applied Lasers," J. Vollmer, *IEEE Spectrum* (June) 1967
"Boron Nitride as a Diffusion Source for Silicon," N. Goldsmith, J. Olmstead, and J. Scott, Jr., *RCA Review* (June) 1967
"A Collision-Induced Instability in Semiconductor Plasmas," B. B. Robinson, *RCA Review* (June) 1967
"Comment on 'A Double-Gap π-Mode Klystron Output Cavity'," C. Sun and Coauthor, *Proc. IEEE* (Letters) (June) 1967
"Dual Polarization FM Broadcasting with a Single Antenna," M. S. Siukola, *Broadcast News* (June) 1967
"Electrical Properties of Copper Phthalocyanine Thin Films as Influenced by the Ambient," A. Sussman, *Jour. Appl. Phys.* (June) 1967
"Flash Evaporation and Thin Films of Cuprous Sulfide, Selenide, and Telluride," S. G. Ellis, *Jour. Appl. Phys.* (June) 1967
"A Laminar Slow-Wave Coupler and Its Application to Indium Antimonide," R. D. Larrabee and W. A. Hicinbothem, Jr., *Trans. IEEE PTGMTT* (Correspondence) (June) 1967
"Landau Damping in Electron Beams," M. Caulton, *RCA Review* (June) 1967
"L-Band Epitaxial Gunn Oscillators," B. E. Berson and S. Y. Narayan, *Proc. IEEE* (Letters) (June) 1967
"Measurement of the Permittivity of Insulating Films at Microwave Frequencies," H. Sobol and J. J. Hughes, *Trans. IEEE PTGMTT* (Correspondence) (June) 1967
"The 'New Look' in Parallel Operation of 12.5 KW VHF TV Transmitters," D. L. Wright, *Broadcast News* (June) 1967
"New 'Vee-Zee' and 'Zee' Panel Type UHF Antennas," A. J. Galinus, *Broadcast News* (June) 1967
"Planning AM/FM Radio Stations, Pt. 2: The Transmitting Plant," *Broadcast News* (June) 1967
"Plasma Properties of a CO_2 Laser Discharge," A. I. Carswell and J. I. Wood, *Jour. Appl. Phys.* (Communications) (June) 1967
"Portable Electronic Keyboard for Computer Input by Telephone," M. H. Lewin, *Trans. IEEE PTGEC* (June) 1967

"A Practical Method of Heat Computations in Electronic Equipment," G. Rezek, *Trans. IEEE PTGPMP* (Correspondence) (June) 1967

"A Programming System for Electron Optical Simulation," H. E. Kulsrud, *RCA Review* (June) 1967

"A Review of the Effect of Imperfections on the Electrical Breakdown of P-N Junctions," H. Kressel, *RCA Review* (June) .. 1967

"Self-Pumped Parametric Amplification with Avalanche Diodes," P. Bura, *Proc. IEEE* (Letters) (June) 1967

"Sonic Film Memory," H. Weinstein, L. Onyshkevych, K. Karstad, and R. Shahbender, *RCA Review* (June) 1967

"Space-Charge Capacitance of Asymmetric, Abrupt P-N Junctions," H. P. Kleinknecht, *Jour. Appl. Phys.* (Communications) (June) 1967

"Space-Charge-Limited Currents in Copper Phthalocyanine Thin Films," A. Sussman, *Jour. Appl. Phys.* (June) 1967

"A Survey of Radiation Effects in Metal-Insulator-Semiconductor Devices," K. H. Zaininger and A. G. Holmes-Siedle, *RCA Review* (June) 1967

"Time-Domain Analysis of Multiple Parallel Transmission Lines," H. Amemiya, *RCA Review* (June) 1967

"Unlock Behavior of the Second Order Phase Locked Loop With and Without Interfering Carriers," F. S. Keblawi, *RCA Review* (June) 1967

"Using Linear IC's for Consumer Products," R. L. Sanquini, *Electronic Engineer* (June) 1967

"Collective Behavior of Polar Impurities in Ionic Crystals. II," W. Zernik, *Phys. Rev.* (10 June) 1967

"Gallium Arsenide FET's Outperform Conventional Silicon MOS Devices," H. W. Becke and J. P. White, *Electronics* (June 12) .. 1967

"A Maser That Works in Radar by Avoiding Saturation," S. B. Adler, *Electronics* (June 12) 1967

"R-F Breakdown Phenomenon Improves the Voltage Capability of a Transistor," P. Schiff, *Electronics* (June 12) 1967

"Advancements in the Facsimile Art During 1966," W. H. Bliss, *IEEE International Convention Record, Part 1, Wire and Data Communication* 1967

"The Future Role of Field-Effect Devices in Electronics," F. P. Heiman, *IEEE International Convention Record, Part 6, Solid-State Circuit and Devices* 1967

"IEEE's Relations with the Professional Societies," G. A. Kiessling, *IEEE International Convention Record, Part 12, Engineering Management; Professional Relations; New Horizons in Science and Engineering* 1967

"New Horizons in Television and Broadcasting," G. H. Brown, *IEEE International Convention Record, Part 12, Engineering Management; Professional Relations; New Horizons in Science and Engineering* 1967

"Solid State Microwave Power Sources," F. Sterzer, *IEEE International Convention Record, Part 7, Electron Devices; Materials; Microwave Components* 1967

"Speech Processing Techniques and Applications," H. F. Olson, H. Belar, and E. S. Rogers, *IEEE International Convention Record*, Part 11, Speech 1967

"Techniques for Altering the Properties of Re-Entry Plasmas," M. P. Bachynski, A. I. Carswell, and B. W. Gibbs, *IEEE International Convention Record, Part 2, Radio Communication; Broadcasting; Propagation; Plasma* 1967

"Visual Sensor Systems in Space," J. J. Dishler, *IEEE International Convention Record, Part 1, Wire and Data Communication* ... 1967

AUTHORS

JOSEPH R. BURNS received his B.S.E.E. from Princeton University in 1959, and his M.S.E.E. from the same institution in 1962. He joined RCA Laboratories in 1959 where he has engaged in research on micro-magnetic memory elements and systems, high-speed transistor–tunnel-diode combinational and sequential logic circuits, and integrated semiconductor memory systems using large arrays of insulated-gate field-effect transistors. He is presently completing graduate work for the Ph.D. degree in electrical engineering at Rutgers University, New Brunswick, N. J. Mr. Burns is a member of the Institute of Electrical and Electronics Engineers.

MICHAEL COOPERMAN received the B.E.E. degree from the City College of New York in 1955, and the M.S.E. degree from the University of Pennsylvania in 1967. In 1955 he joined RCA Home Instruments Division where his work centered on the application of ferromagnetic and ferroelectric devices to television circuits. He later worked on the development of parametric amplifiers and tunnel-diode amplifiers, up converters, and down converters in the UHF range. In 1961 he joined the applied research activity where he worked on development of high speed tunnel-diode and transistor logic circuits. Mr. Cooperman is presently with RCA Defense Micro-Electronics where he is working on establishing design and layout criteria for MOS integrated logic arrays. Mr. Cooperman is a member of the Institute of Electrical and Electronics Engineers, Tau Beta Pi, and Eta Kappa Nu.

R. W. ENGSTROM received the degree of Ph.D. in Physics from Northwestern University in 1939; the dissertation for this degree was in the field of photoelectricity. He joined RCA Electronic Components and Devices, Lancaster, Pennsylvania, as an engineer in 1941. He advanced through several technical and managerial assignments and in 1962 was appointed Manager, Conversion Tube Advanced Development Engineering. During those years, Dr. Engstrom has made numerous contributions to the development and application of photoelectric devices, particularly in the area of low-light-level applications. Dr. Engstrom is a Fellow of the American Physical Society and a Member of Sigma Xi.

A. L. MOREHEAD received the B.S. Degree in Electrical Engineering from the University of Minnesota, where he graduated with distinction in 1958. From 1958 to 1960 he investigated noise in electron tubes under a research assistantship granted by the EE Department. He received the M.S. Degree in Electrical Engineering from the University of Minnesota in 1960. In September 1960 he joined RCA Electronic Components and Devices, Lancaster, Pennsylvania, and was assigned to the advanced development group of the black and white kinescope section. While in this group, he developed a new electron gun for low-power kinescopes. Mr. Morehead was assigned to the image tube design group in February 1961, and in January 1963 he became Manager, Image Tube Product Engineering. Since 1965, he has been Engineeering Leader, low-light-level camera tube development. Mr. Morehead is a member of Tau Beta Pi, Eta Kappa Nu, and the Institute of Electrical and Electronics Engineers.

OTTO H. SCHADE was born and educated in Germany; he came to the United States in 1926. He joined RCA Electronic Components and Devices, Harrison, New Jersey, in 1931. Since 1938, he has specialized in television circuits, camera tubes, and picture tubes. From 1944 to 1957 he worked on a unified general method of image analysis and specification, including practical methods for measuring the "aperature" effect (square-wave and sine-wave response function) and fluctuation levels (noise) of optical, photographic, and electronic image-system components and the eye. He has had the responsibility for the thermal and electrical design of nuvistor tubes. More recently, he has developed an accurate method for calculating the resolving power of television and photographic imaging systems to assist in the evaluation of high-definition television systems, and a new electron optic providing minimum aberrations and uniform focus in television camera tubes with larger (50 × 50 mm) image surfaces. Dr. Schade has received numerous honors, including the Modern Pioneers Award of the National Association of Manufacturers (1940), the Morris Liebmann Memorial Prize of the Institute of Radio Engineers (1950) and a Fellowship (1951) from the Institute of Radio Engineers. In 1951 he was made a Fellow, and also was the first recipient of the David Sarnoff Gold Medal Award, of the Society of Motion Picture and Television Engineers. In June 1953, he was invested with the honorary degree of Doctor of Engineering by Rensselaer Polytechnic Institute. In 1960, he received the Progress Medal Award of the Society of Motion Picture and Television Engineers for his outstanding technical contribution in the engineering phases of the motion picture and television industries.